The Dissertation Committee for Sedef Kocakaplan Certifies that this is the approved version of the following dissertation:

COMPUTATIONAL MODELING OF LOCAL BUCKLING BEHAVIOR IN POST-TENSIONED STEEL BEAM-TO-COLUMN CONNECTIONS

Committee:

Patricia M. Clayton, Supervisor

Michael D. Engelhardt

Yigit Ozcelik

Eric B. Williamson

COMPUTATIONAL MODELING OF LOCAL BUCKLING BEHAVIOR IN POST-TENSIONED STEEL BEAM-TO-COLUMN CONNECTIONS

by

Sedef Kocakaplan

Dissertation

Presented to the Faculty of the Graduate School of

The University of Texas at Austin

in Partial Fulfillment

of the Requirements

for the Degree of

Doctor of Philosophy

The University of Texas at Austin

May 2021

Dedication

To my family

Acknowledgements

First and foremost, I would like to express my deepest appreciation to my supervisor Dr. Patricia M. Clayton for her guidance and inspiring instructions in the development and completion of this study. I would like to express my sincere gratitude for her technical and personal mentorship, patience, support and encouragement for my future career. I would like to thank her for giving me chance to work with her and to get experience in teaching. The experience I gained with her during my PhD studies inspired me to be a professor that is eager to conduct research and teach.

I would like to thank Dr. Michael D. Engelhardt, Dr. Yigit Ozcelik and Dr. Eric B. Williamson for serving on my dissertation committee.

I would also like to express my gratitude to Dr. John L. Tassoulas for his kind support and giving chance to work under his supervision during the first two years of my PhD studies.

I am also grateful to faculty members in Mechanics, Uncertainty and Simulation in Engineering (MUSE) group, Dr. Lance Manuel, Dr. Loukas Kallivokas and Dr. Berkin Dortdivanlioglu, for their support and guidance during my PhD time.

I am thankful to being a part of Dr. Patricia M. Clayton research group. Bushra Islam, Dr. Farid Khosravikia, Joseph J. Gilroy, Yasaman Zeinali and Sangwook Park's discussions of the technical topics and inspiring comments in improving presentation skills during the group meetings helped me a lot in my academic career. I would also like to thank my colleagues in MUSE group, especially Dr. Phong T. T. Nguyen, Dr. Arash Fathi, Dr. Babak Poursartip, Dr. Ying-Chuan Chen, Dr. Heedong Goh, Jinsong Liu, Dr. HyeongUK Lim, Teamin Heo, Dr. Hamidreza Mashayekh and Dr. Coung T. Nguyen for

sharing the same office and their friendship for making each office day better. I would also want to thank my friends in Austin, particularly to Dr. Hande Gerkus Harris, Yucel Alp, Korkut Kaynardag, Dr. Ahmet Celik, Dr. Mehmet Bakir Bozkurt, Ebru Cayir Cengiz, Adem Cengiz and Seda Mursel for all their friendship and support during my time in Austin. I am also thankful to Dr. Farid Khosravikia and Yasaman Zeinali additionally for opening their house for me during the historic winter storm in Austin.

I would like to thank Republic of Turkey Ministry of National Education for the fellowship that I awarded to support my PhD study.

Last but not least, I would like to thank my family and friends back in Turkey for their support. Particularly, my dear twin brother, many thanks to you and your wife, for never wavered in your support. I would like to extend my deepest gratitude to my parents for their endless support, love and encouragement.

COMPUTATIONAL MODELING OF LOCAL BUCKLING BEHAVIOR IN POST-TENSIONED STEEL BEAM-TO-COLUMN CONNECTIONS

Sedef Kocakaplan, Ph.D.

The University of Texas at Austin, 2021

Supervisor: Patricia M. Clayton

Self-centering moment-resisting frames with post-tensioned (PT) beam-to-column connections have been proposed as a damage mitigating alternative to conventional steel moment-resisting frames used in seismic force resisting structural systems. The self-centering capability of properly designed PT connections proves to be an effective tool for improving resilience of a building following an earthquake; however, the rocking behavior of PT beam-to-column connections could result in excessive compressive forces at the contact surfaces between beams and column. These concentrated compressive forces can cause local buckling in the beams, which causes plastic shortening of the beam, resulting in loss of PT force and subsequently reduces connection capacity and self-centering capability of the structure. For this reason, local buckling is a critical limit state that should be considered in design of self-centering moment-resisting frames with PT connections. Additionally, even in well-designed PT connections that can withstand local buckling under design earthquake levels, it is necessary to understand the strength degrading behaviors associated with beam local buckling for assessing collapse risk of these systems.

In this PhD dissertation, a computational study is performed using finite element methods to investigate strength degrading behavior due to beam local buckling. First, detailed finite element simulations are conducted and these simulations are validated using experimental data from quasi-static tests of steel PT moment-resisting connections conducted at the University of Texas at Austin. According to results, modeling recommendations are presented. Secondly, based on these simulation recommendations, a parametric study is performed to investigate parameters affecting strength degradation behavior due to beam local buckling. Finally, simplified fiber cross-section models are proposed using the effective stress-strain behavior extracted from the parametric study results to model the strength degrading behavior in a computationally efficient line element.

Table of Contents

List of Tables xiii

List of Figures xiv

Chapter 1: Introduction 1

1.1 General 1

1.2 Research objectives 5

1.3 Organization of dissertation 6

Chapter 2: Literature Review 8

2.1 Introduction 8

2.1 Overview of self-centering moment resisting frames 8

2.2.1 Yielding elements within the connection 8

Ricles, Sause, and Garlock- [2001] 8

Christopoulos, Filiatrault, Uand, and Folz - [2002] 10

Kim and Christopoulos- [2008] 12

Lin, Sause, and Ricles - [2013] 13

2.2.2 Yielding elements outside the connection 14

Clayton - [2013] 14

2.3 Strength degradation of PT connections due to beam local buckling 15

Garlock - [2002] 15

Chou, Chen, Chen and Tsai- [2006] 17

Chou, Wang, and Chen- [2008] 19

Kim and Christopoulos- [2008] 20

Hulsey- [2015] 21

2.4 Finite element modeling of posttesioned connections 25
Esposto - [2008] 25
Moradi and Alam - [2015] 27
Kim - [2008] 30
Clayton, Tsai, Berman and Lowes - [2015] 32
2.5 Fiber-based and deterioration modeling of moment resisting frames 33
Suzuki - [2018] 34
Kolwankar, Kanvinde, Kenawy, Lignos and Kunnath - [2018, 2019] 39
2.6 Modeling of strength degrading behavior in PT connections 42
Kamperidis - [2016] 42
Ahmadi, Ricles and Sause - [2018] 44
Chapter 3: Finite Element Models of Self-Centering Moment Resisting Frame Connections 48
3.1 Introduction 48
3.2 Reference experiments 50
3.2.1 Tensile coupon tests 54
3.3 Overview of finite element models for post-tensioned beam-to-column connections 57
3.3.1 Element Types 57
3.3.2 Solution Algorithms 58
3.3.3 Boundary conditions and material models 61
3.4 Shell element models 65
3.4.1 Model description 65
3.4.2 Analysis and application of imperfections 66

3.4.3 Meshing 67
3.5 Solid element models.....70
3.5.1 Model description 70
3.5.2 Analysis 71
3.5.3 Meshing 71
3.6 Analysis results and model validation 72
3.6.1 Numerical results for Test Specimen 1 73
3.6.2 Numerical results for Test Specimen 2 77
3.6.3 Numerical results for Test Specimen 3 82
3.6.4 LED data and buckled shape 88
3.7 Summary and modeling recommendations.....92
Chapter 4: Parametric Study to Investigate Local Buckling Behavior of PT Beam-to-Column Connections.....94
4.1 Introduction 94
4.2 Finite element parametric models.....96
4.2.1 Finite element modeling 96
4.2.2 Investigated beam cross-sections and design parameters 98
4.2.3 Modeling techniques.....103
4.2.4 Displacement load history 104
4.3 Results of parametric studies 106
4.3.1 Observed buckling length 106
4.3.2 Characterization of post-buckling behavior under cyclic load 110
4.3.3 Variation in initial PT force and reinforcing plate length.....114
4.4 Summary and conclusions 116

Chapter 5: Fiber-Based Modeling of Strength Degradation in PT Beam-to-Column Connections....118
5.1 Introduction....118
5.2 Fiber-based modeling....120
5.3 OpenSees modeling of PT beam-to-column connections....121
5.4 Hysteretic material model....124
5.5 Application of effective stress-strian relationship....125
5.5.1 Selected numerical hinge integration method....128
5.6 Trends of key parameters....130
5.7 Regression analyis of key constitutive parameters....137
5.8 Fiber discretization....142
5.9 Verification of proposed constitutive model....143
5.9.1 Parametric study....144
5.9.2 Hulsey (2015)....149
5.10 Limitations of the proposed consitutive model....152
5.11 Summary and conclusions....153
Chapter 6: Summary, Conclucions and Recommendations for Future Research....154
6.1 Summary....154
6.2 Conclucions....155
6.3 Recommended future research....156
Appendix A....158
Appendix B....159
References....162

List of Tables

Table 3.1: Summary of test specimen properties 51
Table 3.2: Material properties of beam specimens 56
Table 3.3: Comparison between the shell element FE results and experimental.....74
Table 3.4: Comparison between the shell element FE results and experimental.....79
Table 3.5: Comparison between the shell element FE results and experimental.....85
Table 4.1: Beam and connection detail data used for parametric studies 101
Table 5.1: ABAQUS and OpenSees results comparisons.....146
Table A.1: Material Properties for Beam Webs.....158
Table A.2: Material Properties for Beam Flanges 158

List of Figures

Figure 1.1: SC-MRFs with PT beam-to-column connections with including only PT strands, (a) connection behavior, (b) frame model 2

Figure 1.2: SC-MRFs with PT beam-to-column connections with yielding angles, (a) connectin behvior, (b) exterior joint area 3

Figure 1.3: Limit states and desired limit state progression.....4

Figure 1.4: General progression of the research presented in this study.....6

Figure 2.1: (a) Post-tensioned connection with angles, (b) moment-rotation behavior of post-tensioned connection [Ricles et al.,2001].....9

Figure 2.2: (a) Post-tensioned connection with ED bars; (b) moment-rotation behavior of posttensioned connection [Christopoulos et al.,2002].....11

Figure 2.3: Experimental setup of post-tensioned connection with ED bars [Christopoulos et al.,2002] 11

Figure 2.4: Experimental setup of friction damped post-tensioned connection [Kim and Christopoulos, 2008] 12

Figure 2.5: (a) Experimental details and (b) behavior of friction damped post-tensioned connection [Kim and Christopoulos, 2008] 13

Figure 2.6: (a) Details of posttensioned connection with a beam web friction device; (b) details of web friction device; (c) slotted holes in the beam web; (d) moment rotation response of the proposed connection [Lin et al., 2013] 14

Figure 2.7: (a) Photo of experimental setup of SC-SPSW; (b) force-drift response of the tested specimen [Clayton, 2013] 15

Figure 2.8: Schematic of experimental setup [Garlock, 2002] 16

Figure 2.9: (a) Buckled shape of test Specimen 36s-30 at east peak of second 1.5% drift cycle; (b) reduction of PT force *(T)* due to beam local buckling [Garlock, 2002] 17
Figure 2.10: Test setup [Chou et al., 2006] 18
Figure 2.11: Moment versus drift plots for (a) Specimen 1, (b) Specimen 2, (c) Specimen 3 [Chou et al., 2006] 18
Figure 2.12: Specimen 3 (a) buckling of FRP at 4% drift, (a) flange local buckling at 5% drift [Chou et al., 2006] 19
Figure 2.13: (a) Specimen 3, buckled shape at 5% drift, (b) Specimen 4, effect of web stiffeners [Chou et al., 2008] 20
Figure 2.14: (a) Load drift response of post-tensioned connection with FEDs showing initiation of local buckling; (b) PT force-drift response and reduction in PT force; (c) photo of the beam local buckling at the end of reinforcing plates [Kim et al., 2008] 21
Figure 2.15: Test configuration of post-tensioned connections (a) Specimen W65-PT1 3/4 (b) Specimen W76-PT2 1/4 [Hulsey, 2015] 22
Figure 2.16: Buckled shape at the end of the tests (a) Specimen W55-PT1 3/4; (b) Specimen W76-PT2 1/4 [Hulsey, 2015] 23
Figure 2.17: (a) PT force vs drift (b) moment vs drift response for Specimen W55-PT1 3/4 [Hulsey, 2015] 24
Figure 2.18: (a) PT force vs. drift and (b) moment vs. drift responses for Specimen W76-PT2 1/4 [Hulsey, 2015] 25
Figure 2.19: (a) Mesh of connection region; (b) applied loading protocol [Esposto, 2008] 26

Figure 2.20: (a) Experimental and numerical results; (b) response of ED bars [Esposto, 2008] 27
Figure 2.21: (a) ANSYS model of the connection; (b) mesing details of the nodal area [Moradi et al., 2015] 28
Figure 2.22: (a) Numerical vs. experimental results; (b) yielding and deformation of the angles in FE simulation; (c) experimental photo of yielding [Moradi et al., 2015] 29
Figure 2.23: ANSYS model of the connection and details of friction and bearing elements, and contact elements [Kim et al., 2008] 30
Figure 2.24: Experimental results vs numerical results for: (a) load vs drift response; (b) PT force vs drift response; (c) load vs drift respinse, photo and ANSYS model results of further applied drifts in beam local buckling [Kim et al., 2008] 31
Figure 2.25: (a) Line element models, (b) shell element models [Clayton et al., 2015] 32
Figure 2.26: Obtained buckling length of (a) virtual stub column and (b) physical column tests [Suzuki, 2018] 35
Figure 2.27: Extracted equivalent stress-strain relationship for different axial loading protocols [Suzuki, 2018] 36
Figure 2.28: Extracted equivalent stress-strain relationship: (a) monotonic loading, (b) cyclic loading compressive behavior, (c) cyclic loading tensile behavior [Suzuki, 2018] 37
Figure 2.29: Application of equivalent stress-strain relationship with hinge midpoint integration method [Suzuki, 2018] 38

Figure 2.30: Verification results of applied equivalent stress-strain relationship to cantilever HSS columns [Suzuki, 2018] 39
Figure 2.31: Process for development of nonlocal formulation [Kolwankar et al., 2018] 40
Figure 2.32: (a) Localized buckling length; (b) FE extracted effective stress-strain behavior [Kolwankar et al., 2018] 40
Figure 2.33: (a) Experimental tests, (b) FE simulations, (c) fiber elements (c) effective stress-strain relationship extracted from FE analyses [Kolwankar et al., 2019] 42
Figure 2.34: Details of Opensees model of post-tensioned connections [Kapmeridis, 2016] 43
Figure 2.35: The prototype building of SC-MRFs with WDFs [Ahmadi et al., 2018] 45
Figure 2.36: (a) Details of ABAQUS model for complete shell elements, (b) simplified ABAQUS model, (c) buckling of the beam at the end of reinforcing plates [Ahmadi et al., 2018] 46
Figure 2.37: (a) Details of simplified ABAQUS model of prototype building, (b) at collapse [Ahmadi et al., 2018] 47
Figure 3.1: (a) Isometric view of test setup, and (b) detailed drawing of Specimen 2 [Hulsey., 2015] 53
Figure 3.2: Displacement loading history of experimental work 54
Figure 3.3: Engineering stress-strain relation for beam flanges.....55
Figure 3.4: Engineering stress-strain relation for beam webs 56
Figure 3.5: Schematic of computational finite element post-tensioned connection model with (a) shell elements [adapted from Clayton et al., (2015)], (b) solid elements.....58

Figure 3.6: Displacement loading history of experimental work 59
Figure 3.7: Typical ABAQUS model boundary conditions and restraints.....62
Figure 3.8: Constitutive laws for: (a) beams; (b) structural steel (SS) (e.g., reinforcing plates, column, stiffener, anchorage assembly, and top plates) and post-tensioned bars (PT).....64
Figure 3.9: Idealized tri-linear material model for W18x76 flange coupon test 64
Figure 3.10: Force-displacement relationship for compression-only springs modeled in shell finite element models 66
Figure 3.11: Typical buckling mode considered in the analysis for local geometric imperfections.....67
Figure 3.12: Mesh sensitivity study of Specimen 3 showing maximum moment obtained in simulation normalized with experimental data 69
Figure 3.13: Mesh sensitivity study of Specimen 3 showing minimum moment obtained in simulation normalized with experimental data 69
Figure 3.14: View of connection region showing selected mesh 70
Figure 3.15: Typical ABAQUS model of solid elements showing meshing.....72
Figure 3.16: Moment-drift response validation results for test Specimen 1 using impicit analysis algorithm.....75
Figure 3.17: PT force -drift response validation results for test Specimen 1 using impicit analysis algorithm.....75
Figure 3.18: Moment-drift response validation results for test Specimen 1 using explicit analysis algorithm 76
Figure 3.19: PT force-drift response validation results for test Specimen 1 using explicit analysis algorithm 76

Figure 3.20: Moment-drift response validation results for test Specimen 2 using impicit analysis algorithm 77
Figure 3.21: PT force-drift response validation results for test Specimen 2 using impicit analysis algorithm 78
Figure 3.22: Moment-drift response validation results for test Specimen 2 using explicit analysis algorithm 78
Figure 3.23: PT force-drift response validation results for test Specimen 2 using explicit analysis algorithm 79
Figure 3.24: Comparison between (a,c) experimental and (b,d) simulated shell models flange and web buckled shapes at the end of the first N 4% drift cycle 81
Figure 3.25: Comparison between (a) experimental and (b) simulated shell models flange and web buckled shapes at the end of 5% drift cycle 81
Figure 3.26: Moment-drift response validation results for test Specimen 3 implicit analysis algorithm 83
Figure 3.27: PT force-drift response validation results for test Specimen 3 implicit analysis algorithm 83
Figure 3.28: Moment-drift response validation results for test Specimen 3 explicit analysis algorithm 84
Figure 3.29: PT force-drift response validation results for test Specimen 3 explicit analysis algorithm 84
Figure 3.30: Bearing plate deformations at north bearing plate (a) at the end of the test, Hulsey (2015) and (b) at the end of the 8% drift cycles in the solid element FE model 85

Figure 3.31: Comparison of simulated shell models and experimental buckled shapes (a,b) at peak of first 8% N cycle-northwest edge (c,d) at the end of second 8% S drift cycle.....87
Figure 3.32: Comparison between simulated and experimental buckling shapes at the end of 9% drift (a) experimental buckling shape (b) simulated buckling shape 88
Figure 3.33: LED marker locations on the beam web and flanges [Hulsey, 2015].....89
Figure 3.34: Experimental vs. simulation results for specimen with W18x55 beam at the end of the first north 4% drift cycle 90
Figure 3.35: Experimental vs. simulation results for specimen with W18x55 beam at the end of the first north 5% drift cycle 91
Figure 3.36: Experimental vs. simulation results for specimen with W18x55 beam at the end of the test 92
Figure 4.1: Local slenderness ratios of selected beam sections for parametric simulations, shown with respect to AISC Seismic Provisions (2016b) limits 99
Figure 4.2: Distribution of analysis method with respect to beam local slenderness ratios.....104
Figure 4.3: Displacement loading history for parametric analyis in ABAQUS/Standard 105
Figure 4.4: Displacement loading history for parametric analyis in ABAQUS/Explicit 106
Figure 4.5: Projected strains [Kolwankar et al., 2019] 108
Figure 4.6: Buckling length of Model Number 3 109
Figure 4.7: Buckling length of Model Number 12 109

Figure 4.8: Extracted stress-strain relationship and idealized multi-linear backbone curve for Model Number 22 111
Figure 4.9: Extracted stress-strain relationship and idealized multi-linear backbone curve for Model Number 11 112
Figure 4.10: Key parameters for idealized multi-linear backbone curve.....113
Figure 4.11: Effect of reinforcing plate (R-Plate) length on the effective stress-strain response for Model Number 22 114
Figure 4.12: Effect of initial PT force (as a proportion of beam yield force, P_y) on the effective stress-strain response for Model Number 12 115
Figure 4.13: Effect of initial PT force (as a proportion of beam yield force, P_y) on the effective stress-strain response for Model Number 11 116
Figure 5.1: Fiber line element geometry and describtion in OpenSees [Garlock,2002] 121
Figure 5.2: Beam with hinges model employing a midpoint hinge integration.....121
Figure 5.3: Schematic of PT beam-to-column connection modeling in OpenSees 122
Figure 5.4: Definition of Hysteretic material in OpenSees.....124
Figure 5.5: Schematic and organization of the research in extraction and application of the effective stress-strain relationship 125
Figure 5.6: Generalized strength degrading slope and residual stress extracted from effective stress-strian responses.....127
Figure 5.7: Comparison of OpenSees and ABAQUS modeling results for Model Number 5 127
Figure 5.8: Modified two-point Gauss-Radau integration [Scott et al., 2006] 129
Figure 5.9: The effective stress-strain beahvior applied to fiber sections in the predefined hinges of a forced-based beam column element.....130

Figure 5.10: Trends for the key parameters with respect to bf/2tf (a) critical (maximum) stress; (b) corresponding critical strain 132
Figure 5.11: Trends for the key parameters with respect to bf/2tf (a) residual stress at which slope changes from degradation to stabilization; (b) corresponding residual strain 133
Figure 5.12: Trends for the key parameters with respect to h/tw (a) critical (maximum) stress; (b) corresponding critical strain 135
Figure 5.13: Trends for the key parameters with respect to h/tw (a) residual stress at which slope changes from degradation to stabilization; (b) corresponding residual strain 136
Figure 5.14: Comparisons between FE-extracted and predicted key parameters (a) critical (maximum) stress; (b) corresponding critical strain; (c) residual stress; (d) corresponding residual strain 140
Figure 5.15: Fiber discretization of wide-flange sections [Kostic and Filippou, 2012], (a) 4x1-4x1-4x1 (b) 8x1-4x2-8x1 (c) 8x2-8x1-8x2 (d) 12x3-12x3-12x3...143
Figure 5.16: Fiber discretization comparisons for moment vs. drift response.....143
Figure 5.17: Comparisons of ABAQUS results and OpenSees results for predictive equations for Model Number 21 145
Figure 5.18: Comparisons of ABAQUS results and OpenSees results for predictive equations for Model Number 21 145
Figure 5.19: Comparisons of maximum moment observed from ABAQUS FE models vs. OpenSees models 148
Figure 5.20: Comparisons of moment response at 10% drift from ABAQUS models vs. OpenSees models 148

Figure 5.21: Comparisons of experimental and OpenSees results for connection moment vs. drift response of Test Specimen 2 150
Figure 5.22: Comparisons of experimental and OpenSees responses for PT force vs. drift response of Test Specimen 2 150
Figure 5.23: Comparisons of experimental and OpenSees responses for connection moment vs. drift response of Test Specimen 3 151
Figure 5.24: Comparisons of experimental and OpenSees responses for PT force vs. drift response of Test Specimen 3 152
Figure B.1: Comparisons between ABAQUS results with multi-linear backbone and Regressed Equation results for Model Number 8 159
Figure B.2: Comparisons of ABAQUS results and OpenSees results for Model Number 8 160
Figure B.3: Comparisons between ABAQUS results with multi-linear backbone and Regressed Equation results for Model Number 12 160
Figure B.4: Comparisons of ABAQUS results and OpenSees results for Model Number 12 161

Chapter 1: Introduction

1.1 General

In current seismic design codes, to prevent loss of lives, structures are designed based on "life safety" performance under the design basis earthquake (DBE). Structures are expected to undergo large deformations with significant damage to structural elements under severe seismic loads. Therefore, structural members can experience yielding, buckling, and fracture, resulting in a structure with permanent horizontal displacements or residual drifts after an earthquake. Damage of main structural members can lead to high repair costs and significant loss of functionality and can even necessitate demolition of the entire structure.

Following the 1994 Northridge Earthquake, brittle failures observed in welded beam-column connections prompted the search for new connection types to improve the seismic performance of steel moment-resisting frames. Most of the proposed connections focus on concentrating yielding in structural elements away from the brittle welded regions; however, such design approaches, while exhibiting enhanced ductility, result in significant plastic deformations and damage following an earthquake. To achieve more resilient and sustainable cities, structures that experience no or minimal damage to the main structural components have been proposed in recent decades. The self-centering moment-resisting frame (SC-MRF) with post-tensioned (PT) beam-to-column connections is one such structural system that can withstand earthquake loads with minimal damage and residual drifts. Instead of yielding the main structural elements, gap opening occurs in the connections, which keeps the main structural components, including beams and columns, elastic. In SC-MRFs with PT beam-to-column connections, PT strands or bars run along the beam length and are anchored behind the column flanges as shown in Figure 1.1 (b).

The PT elements provide recentering capabilities in SC-MRFs, allowing them to come back to their plumb position after an earthquake and preventing residual drifts as shown by the bilinear elastic behavior of in Figure 1.1 (a).

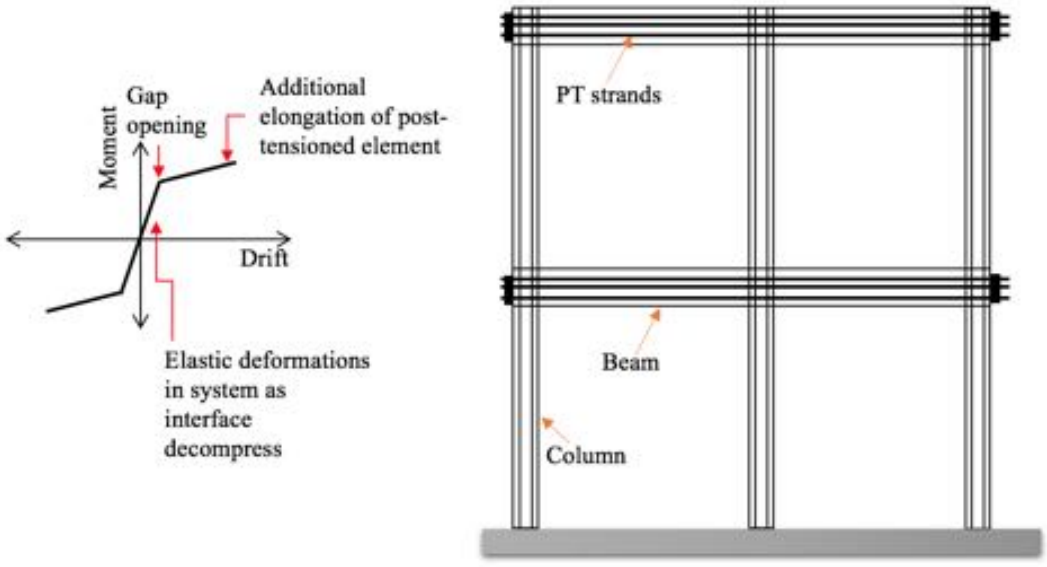

Figure 1.1: SC-MRFs with PT beam-to-column connections with including only PT strands, (a) connection behavior, (b) frame model

Since the PT connections themselves are designed to remain elastic, energy dissipation must be provided by special energy dissipation devices. These energy dissipation elements can be yielding elements within the connection (e.g., top and seat angles in Garlock (2002), buckling restrained bars in Christopoulos et al., (2002)), friction devices in the beam flange or web (e.g., Iyama et al., (2008) and Lin et al., (2013), respectively), or yielding elements outside of the connections (e.g., steel plate shear walls per Clayton et al., (2015)). An example of a PT beam-to-column connection with angles is shown in Figure 1.2 with the resulting flag-shape hysteretic behavior, which notably still results in no residual drifts.

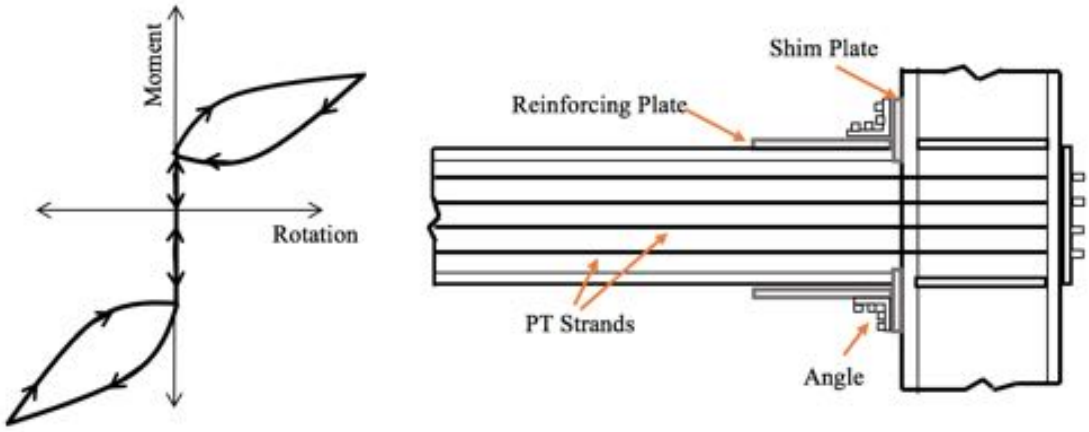

Figure 1.2: SC-MRFs with PT beam-to-column connections with yielding angles, (a) connection behavior, (b) exterior joint area

While PT beam-to-column connections are generally designed to remain elastic during design-level seismic loading, with the exception of yielding in specific replaceable energy dissipation devices, it is important to understand potential connection limit states for assessing system-level performance and collapse resistance under extreme earthquake loading. Previous researchers (e.g., Garlock (2002)) have investigated limit state behaviors of SC-MRFs with PT beam-to-column connections, which are summarized by Chancellor et al., (2014). Figure 1.3 shows the target limit state progression for SC-MRFs with PT beam-to-column connections. The first limit state that is expected to occur is decompression or gap opening within the PT connections, with yielding or friction activation in the energy dissipating devices. The second limit state is limited damage to the structure, which could include limited panel zone yielding in the columns or horizontal shear yield in the beam web. The last limit state is severe damage to structural elements, which can include beam local buckling and PT strand yielding, both of which can lead to loss of moment-resisting capabilities in the PT connections and even collapse.

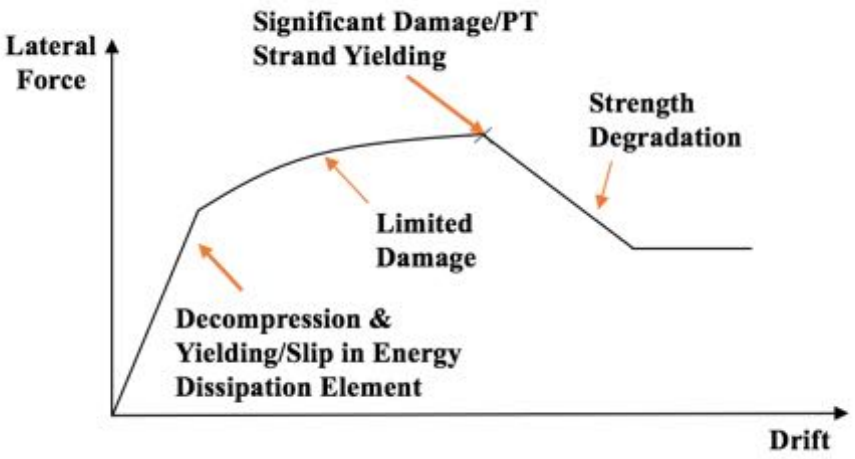

Figure 1.3: Limit states and desired limit state progression

In this research, PT connection strength degradation due to beam local buckling is the target limit state that is investigated. Beam local buckling can occur as a result of excessive compressive forces at the contact surfaces between the beam and column. These contact forces increase compressive stresses in the beam flanges after gap opening in the connection, which leads to beam local buckling. Local buckling causes plastic shortening of the beams, resulting in loss of post-tension force and subsequently reducing the connection capacity and self-centering capability of the structure (Garlock, 2002). Therefore, beam local buckling is a critical limit state that should be considered in design of self-centering steel moment-resisting frames. Additionally, even in well-designed PT connections that can withstand beam local buckling under design earthquake levels, it is necessary to understand the strength degrading behaviors associated with beam local buckling for assessing collapse risk of these systems.

1.2 RESEARCH OBJECTIVES

Based on the discussion in Section 1.1, collapse performance of SC-MRFs with PT beam-to-column connections experiencing beam local buckling should be investigated in detail. This collapse performance assessment requires capturing strength degradation behaviors due to beam local buckling in computationally efficient ways that facilitate a large number of nonlinear response-history analyses of system-level models subjected to a wide range of earthquake ground motions. Previous research on the collapse performance of these structures due to beam local buckling is limited. Ahmadi (2016) investigated collapse performance of SC-MRFs with web friction devices due to beam local buckling with computationally expensive shell-based finite element models, while Kamperidis (2016) used more computationally efficient concentrated plasticity models to simulate the general strength degrading behaviors of PT connections but did not explicitly consider the local buckling limit state and axial-flexural interaction in the connection behavior. To investigate the strength degrading behavior of PT beam-to-column connections due to beam local buckling, the main objectives of this research, as represented schematically in Figure 1.4, are:

- Develop experimentally validated finite element models to explicitly capture beam local buckling in PT beam-to-column connections
- Perform a parametric study to investigate design parameters affecting strength degradation behavior
- Characterize strength degradation behavior from results of the parametric study
- Develop empirical equations to model strength degradation behavior for various beam cross-sections

Employ the developed empirical equations in a simplified fiber-based line element model to capture the strength degrading effects of local buckling in PT beam-to-column connections

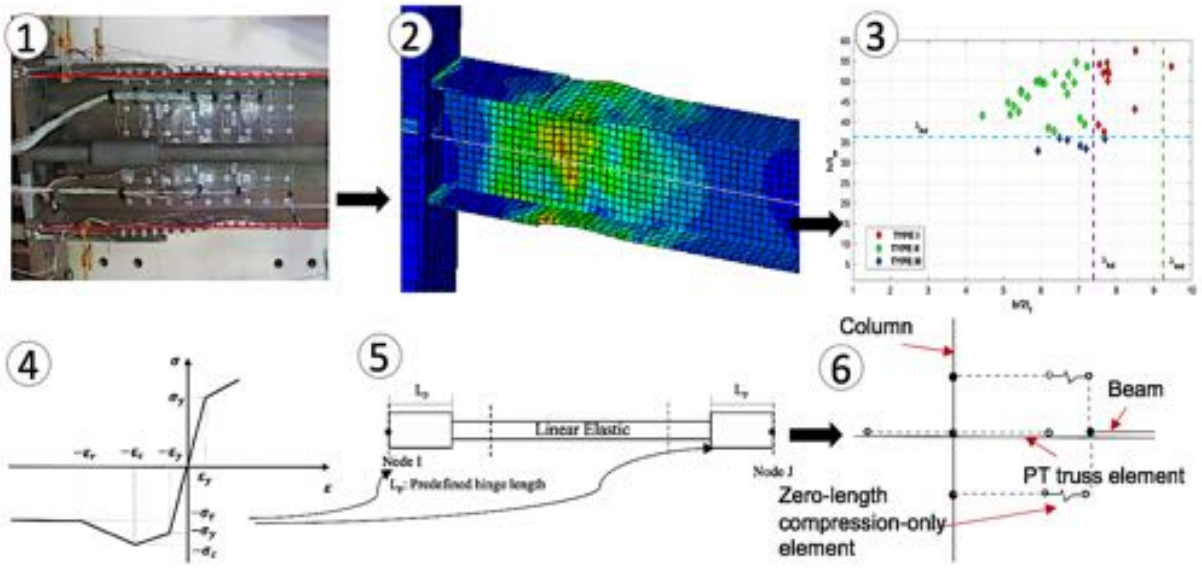

Figure 1.4: General progression of the research presented in this study

1.3 Organization of Dissertation

This dissertation includes six main chapters as explained here briefly:

- *Chapter 1*: Provides an introduction to the main concepts of SC-MRFs with PT beam-to-column connections and presents the objectives of this study.
- *Chapter 2*: Provides a literature review on behavior and modeling of PT beam-to-column connections.
- *Chapter 3*: Presents detailed finite element models of experimentally tested PT beam-to-column connections both with solid and shell elements and

with implicit and explicit solution techniques. Modeling recommendations are provided based on results.

- *Chapter 4*: Presents a parametric study to investigate local buckling behavior of PT beam-to-column connections using the recommending finite element modeling approaches. Discusses properties and investigated parameters and their effect on local buckling strength-degradation behavior.
- *Chapter 5*: Proposes a fiber-based line element approach to model local buckling-induced strength degradation of PT beam-to-column connections. Provides empirical equations for proposed strength degradation model due to beam local buckling and presents modeling results.
- *Chapter 6*: Presents a summary and conclusions for the research and gives directions for future work.

Chapter 2: Literature Review

2.1 INTRODUCTION

In this chapter, past research on self-centering moment-resisting frames with PT beam-to-column connections is discussed. The focus is on the key points that are outlined during the research. First, overviews of self-centering moment-resisting frames (Section 2.1) and strength degrading behavior of PT connections due to beam local buckling (Section 2.2) are presented. Previous finite element (FE) modeling techniques are summarized in Section 2.3. Finally, fiber-based modeling techniques (Section 2.4) and collapse performance analysis of self-centering moment frames (Section 2.5) are discussed.

2.2 OVERVIEW OF SELF-CENTERING MOMENT-RESISTING FRAMES

Self-centering moment-resisting frames have been proposed in the last couple of decades, which utilize PT beam-to-column connections to mitigate damage in structures compared to traditional moment-resisting frames with conventional yielding connections. Self-centering moment-resisting frames typically include energy dissipation elements that can be categorized into two types, (i) yielding elements or friction devices within the connection and (ii) yielding elements outside the connection, as summarized in Sections 2.1.1 and 2.1.2, respectively.

2.2.1 Yielding Elements Within the Connection

Ricles, Sause, and Garlock – [2001]

The new type of self-centering moment-resisting frame with PT beam-to-column connection was proposed in the authors' research. The post-tensioned tendons run along

the beam length and are anchored to the column flanges as shown in Figure 2.1 (a). Energy dissipation is provided by yielding of the top and seat angles in the connection as also shown in Figure 2.1 (a). Keeping the plastic deformations located in the angles allows the beams and columns to stay essentially elastic, and the angles can be replaced after an earthquake. As shown in Figure 2.1 (b), the post-tensioned tendons provide recentering capabilities for the structure, allowing it to self-center after earthquake loads are removed (i.e., the connection returns to zero rotation as it is unloaded).

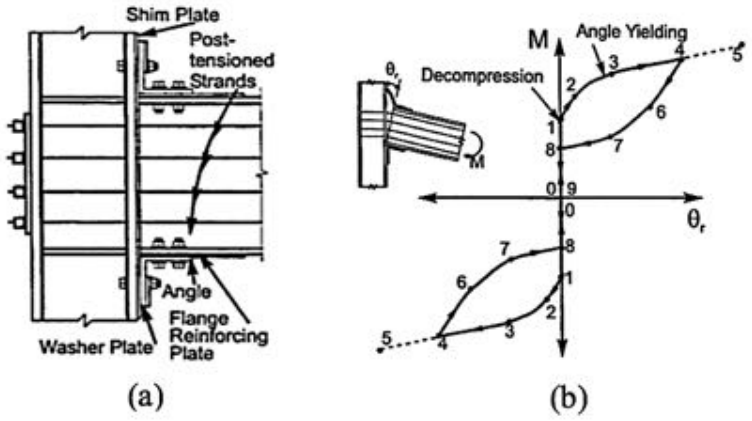

Figure 2.1: (a) Post-tensioned connection with angles; (b) moment-rotation behavior of post-tensioned connection [Ricles at al.,2001]

The authors propose an analytical model consisting of fiber-based elements to simulate the compression-only rocking behavior at the beam ends, as well as yielding along the beam length. The analytical model results are compared with the experiments conducted by the authors. This analytical model is then used to perform parametric studies to investigate the effects of connection details on the moment-rotation behavior of the connection and yielding in the beam. The parameters varied are: presence of reinforcing plates, the size and gauge length of the angles, and initial PT force. The results of the

analytical studies showed that reinforcing plates on the beam flanges prevent excessive yielding in the connection, which is necessary to maintain self-centering capabilities. Another finding from the study is that an increase in initial PT force could result in yielding of the beam flanges even in the presence of reinforcing plates. Finally, the authors concluded that connections with stiffer and stronger angles provide higher post-decompression stiffness and energy dissipation.

Christopoulos, Filiatrault, Uang, and Folz - [2002]

The authors presented a post-tensioned connection with energy dissipating bars (PTED) in which self-centering is provided by high-strength PT bars and energy dissipation is provided by buckling restrained energy dissipating (ED) bars enabling yielding in tension and compression. The PTED connection details are given in Figure 2.2 (a). ED bars are welded into couplers starting from the inside if the beam flanges and welded to the column continuity plates. Moment rotation behavior of the connection is presented in Figure 2.2 (b). According to the figure, the connection can self-center, and it dissipates energy through yielding of the ED bars.

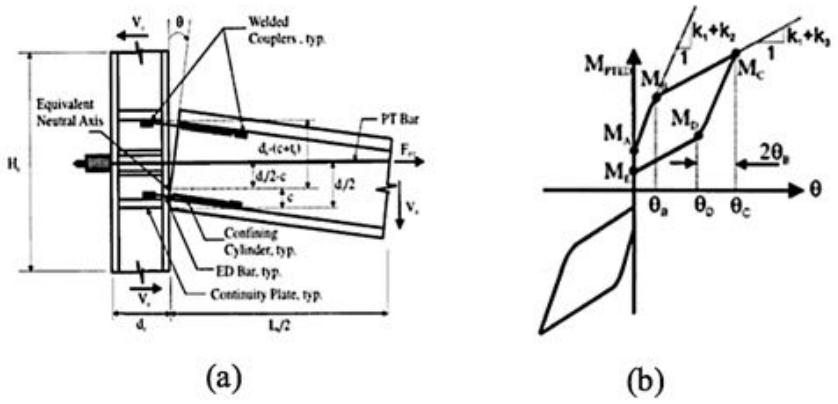

Figure 2.2: (a) Post-tensioned connection with ED bars; (b) moment-rotation behavior of post-tensioned connection [Christopoulos at al., 2002]

Performance of the connection is tested by conducting experimental studies. The experimental setup is shown in Figure 2.3 (a) and results are presented in Figure 2.3 (b). Experimental results showed that the PTED connection can provide self-centering with energy dissipation and keep the columns and beams damage-free under large deformations.

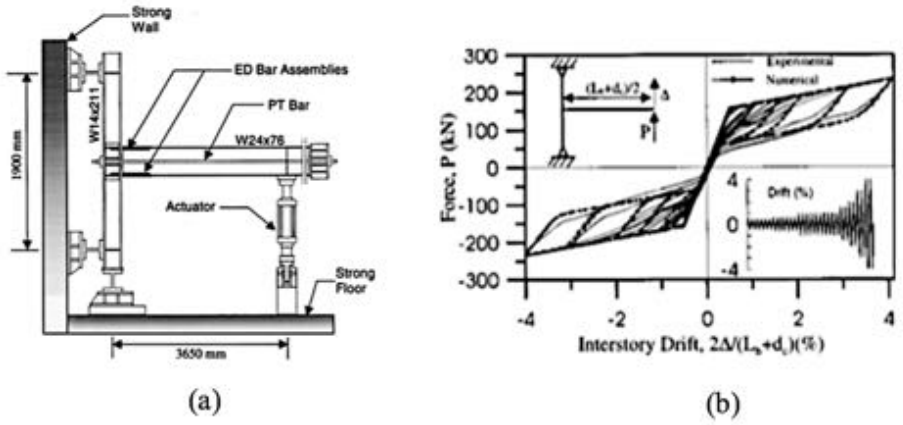

Figure 2.3: Experimental setup of post-tensioned connection with ED bars [Christopoulos at al., 2002]

Kim and Christopoulos - [2008]

Energy dissipation in post-tensioned connections can also be provided by friction mechanisms. Kim and Christopoulos (2008) proposed a new type of self-centering moment-resisting frame with PT connections with frictional energy dissipating devices (FEDs). The FEDs are located on the top and bottom of the beams to provide shear slip mechanisms as the connection rotates open, as shown in Figure 2.4. FEDs consist of three plates: one outer plate is welded to the column, the inside plate is welded to the beam flange, and the other outer plate is bolted to the inner plate without welding to the column. The friction energy dissipation mechanism gets activated with the gap opening behavior of the connection.

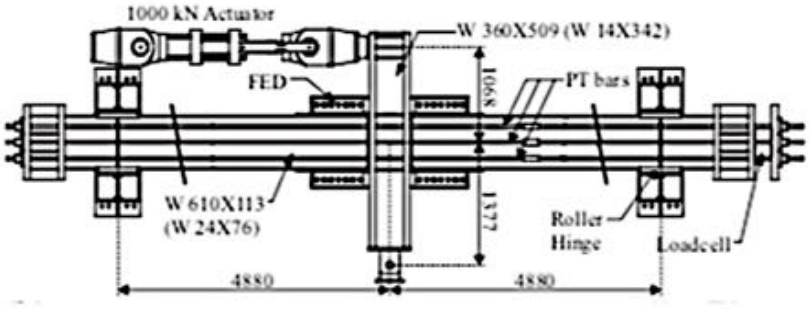

Figure 2.4: Experimental setup of friction damped post-tensioned connection [Kim and Christopoulos, 2008]

The authors conducted experimental tests for an interior beam-column assembly (as shown in Figure 2.4) and exterior beam-column assembly to evaluate the performance of the connection with FEDs. Figure 2.4 shows the experimental setup, and Figure 2.5 (a) presents the photos of the connection during the test, both before and after connection gap opening. According to experimental results, the proposed connection can provide self-

centering capability and FEDs provide seismic energy dissipation under applied cyclic lateral loads as shown in Figure 2.5 (b).

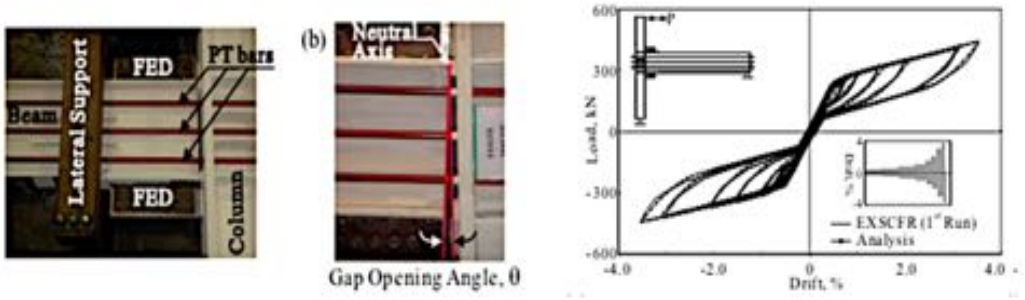

(a) (b)

Figure 2.5: (a) Experimental details and (b) behavior of friction damped post-tensioned connection [Kim and Christopoulos, 2008]

Lin, Sause, and Ricles - [2013]

The final example of yielding elements within the connection that will be discussed in this section is the post-tensioned connection with a beam web friction device. Self-centering is provided by the post-tensioned elements, while energy dissipation is provided by web friction devices. Details of the connection are given in Figure 2.6. Reinforcing plates are provided to prevent beam yielding while shim plates that are welded to the column flange provide an even contact surface during the gap opening and closing phenomena. To assemble the connection, first, the friction channels are clamped to the beam web by prestressed friction bolts. Following this process, the channels are welded to the columns. The web friction device activates during connection gap opening by sliding inside the slotted holes in the web shown in Figure 2.6 (c).

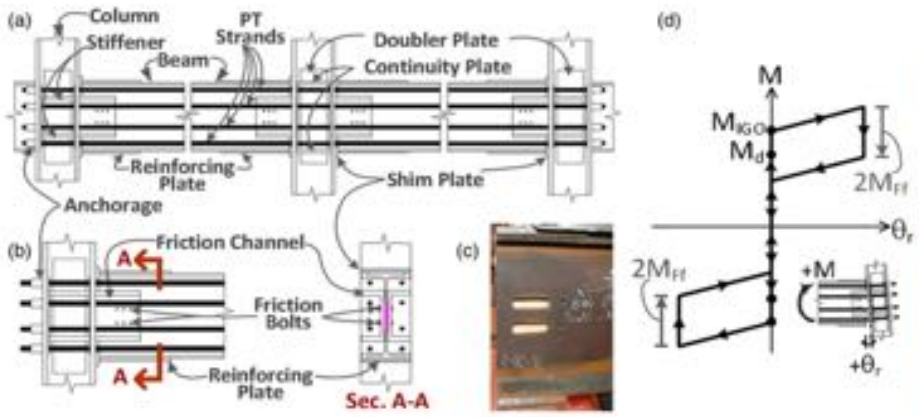

Figure 2.6: (a) Details of post-tensioned connection with a beam web friction device; (b) details of web friction device; (c) slotted holes in the beam web; (d) moment-rotation response of the proposed connection [Lin et al., 2013]

2.2.2 Yielding Elements Outside of the Connection

Clayton – [2013]

In addition to having yielding elements within the connection, the self-centering steel plate shear wall (SC-SPSW) is proposed to provide energy dissipation away from the connection. The SC-SPSW employs post-tensioned beam-to-column connections with reinforcing plates, and a thin steel infill plate that is attached to the beams and columns away from the connection regions. The seismic performance of the SC-SPSW system is investigated through experimental and numerical studies. Fifteen large-scale specimens consisting of two half-stories were tested during the quasi-static experimental program. Under applied lateral loads, the lateral strength of the SC-SPSW is provided by the thin steel infill plates connected to the beams and columns or to the beams only (as shown in Figure 2.7 (a)). Self-centering is provided by the post-tensioned beam-to-column connections, and energy dissipation is provided by ductile yielding of the infill plate via

tension field action. The flag-shaped hysteretic behavior of the system is shown in Figure 2.7 (b).

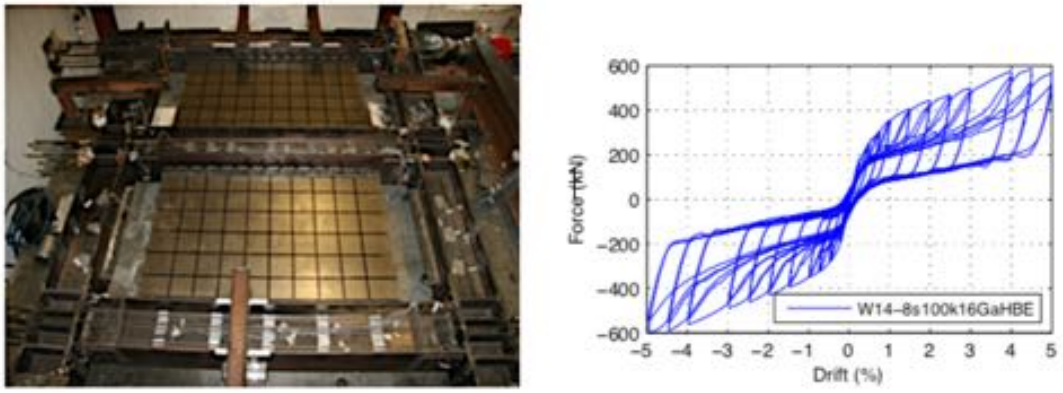

Figure 2.7: (a) Photo of experimental setup of SC-SPSW; (b) force-drift response of the tested specimen [Clayton, 2013]

2.3 STRENGTH DEGRADATION OF PT CONNECTIONS DUE TO BEAM LOCAL BUCKLING

Garlock – [2002]

Garlock's research extended the work performed by Ricles et al. (2001) by introducing design procedures for the connections, based on simplified models and additional experiments. To investigate different limit states and seismic performance of post-tensioned connections with bolted top and seat angels, six full-scale interior connections are tested. The specimens are subjected to cyclic loading up to 4% drift following the loading protocol of the *AISC Seismic Provisions* (1997). Each test specimen includes the same beam size, W36x150, with 14-inch wide, 1-inch-thick reinforcing plates as shown in the experimental setup in Figure 2.8. The test variables included reinforcing plate length, number of PT tendons, and initial PT force to investigate different limit states such as angle fracture, beam local buckling, and strand yielding.

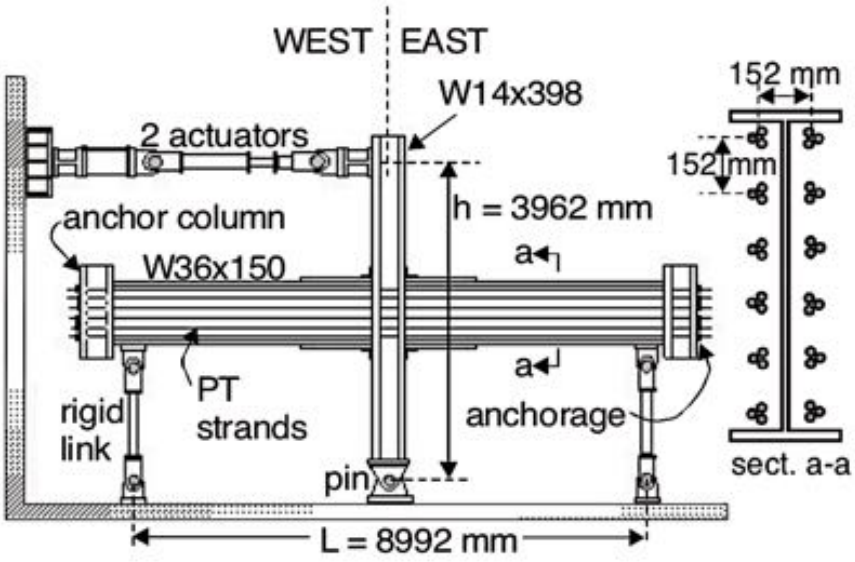

Figure 2.8: Schematic of experimental setup [Garlock, 2002]

The test specimen of most interest to the current research is Specimen 36s-30 in which beam local buckling is observed. The referenced test specimen is initially post-tensioned to a force of 1063 kips and the reinforcing plate length is equal to the nominal beam depth, which is 36 inches. The buckling of the specimen first occurred in the east beam at the first 1.5% peak drift cycle to the east. The buckling continued to increase until the test ended after the second 1.5% drift cycle as shown in Figure 2.9 (a). The buckling of the beam caused the beam to shorten, leading to a reduction in PT forces as shown in Figure 2.9 (b).

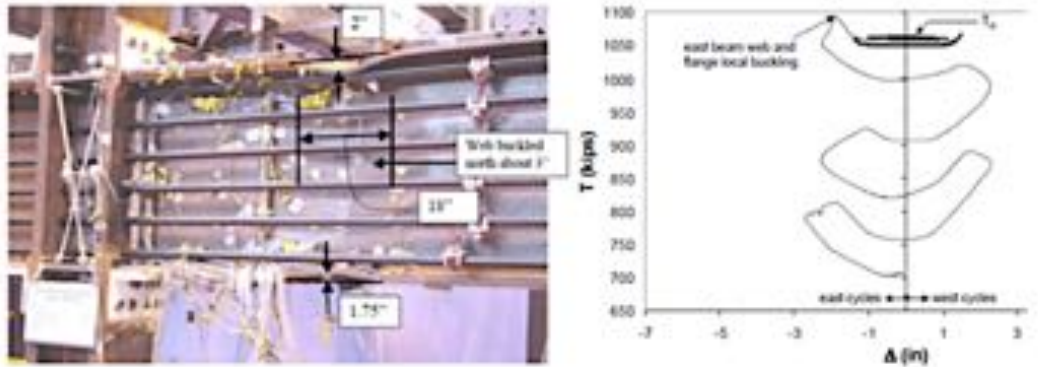

(a) (b)

Figure 2.9: (a) Buckled shape of test Specimen 36s-30 at east peak of second 1.5% drift cycle; (b) reduction of PT force (*T*) due to beam local buckling [Garlock, 2002]

Chou, Chen, Chen and Tsai – [2006]

The authors investigated seismic performance of post-tensioned connections through experimental and finite element studies. The model includes two steel beams connected to the concrete filled tube (CFT) column with post-tensioned strands that provide rocking behavior in the connection. Energy dissipation is provided using buckling restrained reduced flange plates (RFPs) welded to the column and bolted to the top of the beam flanges. RFPs provide energy dissipation through yielding in axial tension and compression. The test setup is shown in Figure 2.10. The applied drifts are three cycles at inter story drifts of 0.25, 0.375, 0.5, 0.75, and 1% then two cycles at 1.5, 2, 3, 4 and 5% drifts. For each specimen, the reinforcing plate lengths are kept constant. Specimen 1 has connections with PT strands only and no RFPs, while Specimens 2 and 3 includes RFPs. Specimen 3 includes cover plates to prevent buckling of RFPs. Figure 2.11 shows the response of the three specimens. Specimens 2 and 3 experienced buckling of the RFPs and beam flanges at 4% drift, while the degradation in moment capacity started after 5% drift

leading to loss of PT force and recentering capabilities as shown in Figure 2.11 (b) and (c), and Figure 2.12 (a) and (b).

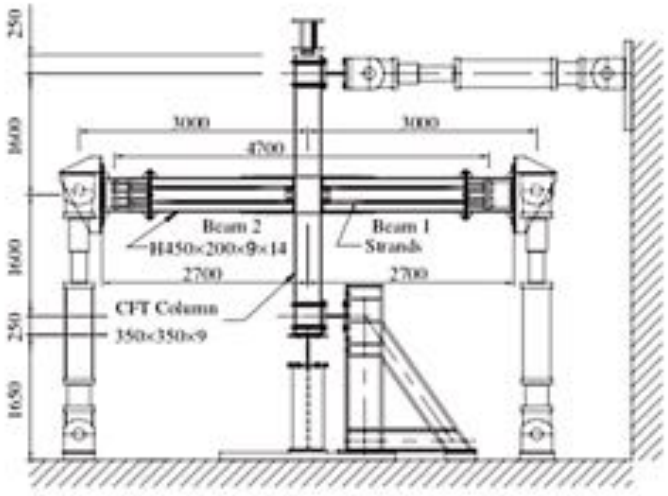

Figure 2.10: Test setup [Chou et al., 2006]

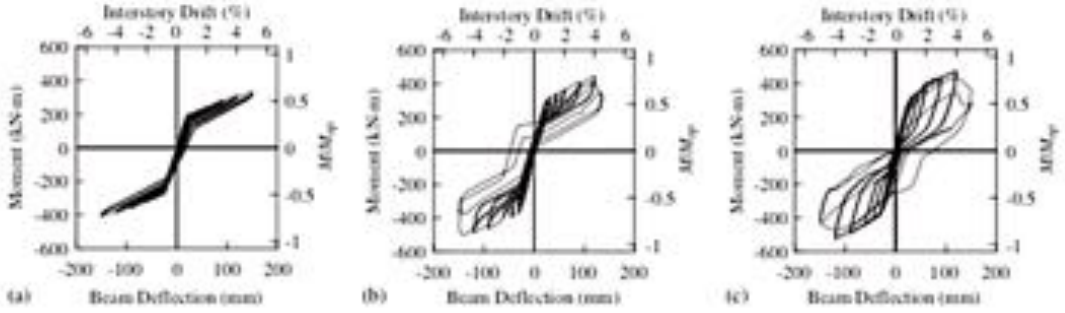

Figure 2.11: Moment versus drift plots for (a) Specimen 1, (b) Specimen 2, (c) Specimen 3 [Chou et al., 2006]

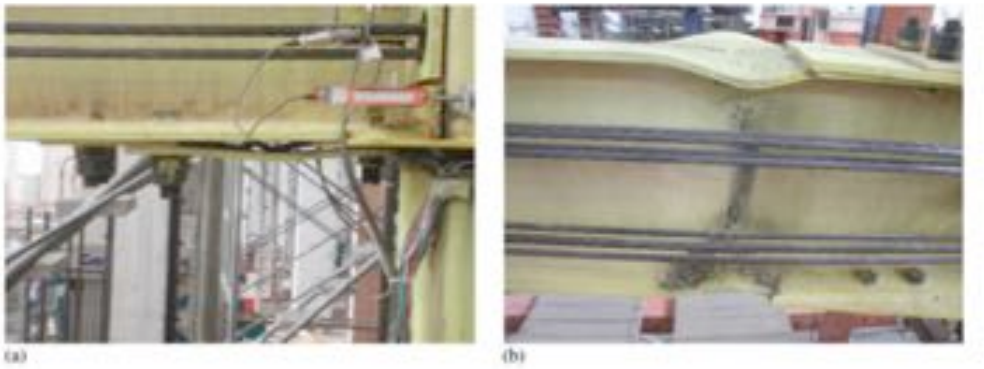

Figure 2.12: Specimen 3 (a) buckling in RFP at 4% drift, and (b) flange local buckling at 5% drift [Chou et al., 2006]

Chou, Wang, and Chen – [2008]

Chou extended the research on post-tensioned connections by conducting three series of six full-scale cyclic tests of interior connections. The effect of beam web stiffeners on beam local buckling and the interaction of the rocking connection and the composite slab is investigated in this research. Applied loading is the same as in the Chou et al. (2006). In the second test series, the authors varied the beam reinforcing plate lengths (based on a different gap opening angle chosen for each specimen and the expected strains in the beam at that gap opening angle) and included a test specimen with a web stiffener (Test Specimen 4). Test Specimen 4 has a lower initial PT force based and fewer PT strands than Specimen 3. Figure 2.13 shows test results for Specimen 3 in the second series where local buckling is observed. Specimen 4 includes web stiffeners at a location of $d_b/4$ away from the end of the reinforcing plate (d_b is the beam depth). The authors concluded that, rather than changing the reinforcing plate length to prevent beam local buckling, additional stiffeners can successfully prevent beam local buckling.

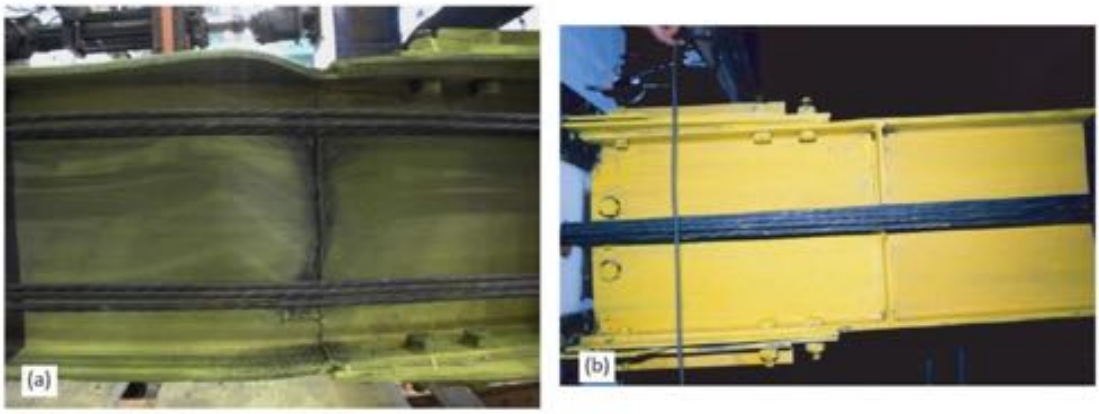

Figure 2.13: (a) Specimen 3, buckled shape at 5% drift, (b) Specimen 4, effect of web stiffeners [Chou et al., 2008]

Kim and Christopoulos – [2008]

In this research, in addition to proposing post-tensioned connections with FEDs, the experimental study also investigated the limit state response of the connection. The test specimens include W24x76 beams with a reinforcing plate length equal to the beam depth. As expected, beam local buckling occurred just beyond the ends of the reinforcing plates. The test specimen shown in Figure 2.14 experiences local buckling at a drift of 6.2%. As shown in Figure 2.14 (a), reduction of the connection stiffness at 4% drift is observed due to yielding in the beams at the end of the reinforcing plates, yet the PT force is not notably affected by this reduction of stiffness. With increasing drift, bearing of the bolts in the inner friction plates of the FEDs occurred at 4.5% drift, which led to a slight increase in connection stiffness. The maximum PT force is reached at 5.9% drift as shown in Figure 2.14 (b). Local buckling of the beam (shown in Figure 2.14 (c)) happened at the maximum drift of 6.2% drift, causing a significant reduction in the PT force.

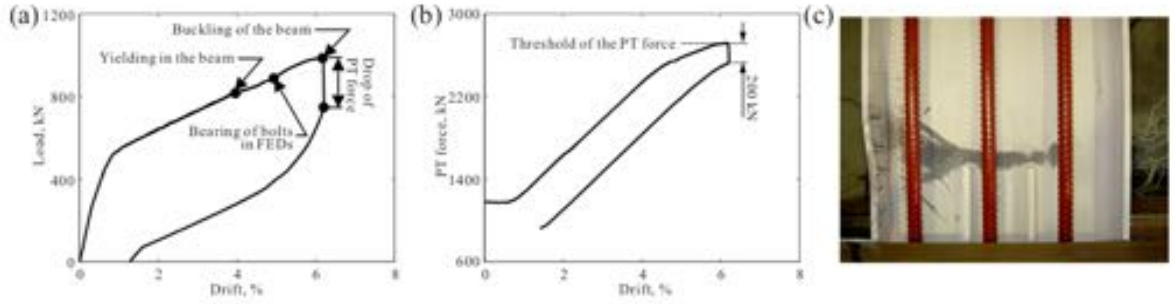

Figure 2.14: (a) Load-drift response of post-tensioned connection with FEDs showing initiation of local buckling; (b) PT force-drift response and reduction in PT force; (c) photo of the beam local buckling at the end of reinforcing plates [Kim et al., 2008]

Hulsey - [2015]

Hulsey conducted three experiments with varied beam sections to investigate beam local buckling of post-tensioned beam-to-column connections. The first test, W65- PT1¾, includes a W18x65 beam with two 1 ¾ inch diameter PT bars and ½ inch thick reinforcing plates with a length equal to the beam depth. The second test, W55-PT1¾, includes a W18x55 beam with two 1¾ inch diameter PT bars and ¾ thick reinforcing plates with a length equal to the beam depth. The last test, W76-PT2¼, includes a W18x76 beam with two 2¼ inch diameter PT bars and ½ thick reinforcing plates with a length equal to the beam depth. The initial post-tension force for all specimens is kept around 350 kips. The cyclic loading for first two test specimens is up to 5% drift, which was limited by actuator stroke capacity, while loading is applied up to 10% drift for the last specimen by moving the actuator closer to the connection and reducing the beam length as shown in Figure 2.15 (b). More details about these tests are also provided in Section 3.2 of this dissertation.

According to the test results, clear local buckling is observed in test Specimens W55-PT1¾ and W76-PT2¼ as shown in Figure 2.16 (a) and (b). Due to beam local buckling, the beam length shortened plastically and resulted in reduction of the PT forces

as shown in Figure 2.17 (a) and (b) for test Specimen W55-PT1¾. As observed in the moment and PT force vs. drift responses, Specimen W55-PT1¾ started buckling at 4% drift, resulting in a loss of PT force and connection capacity. The buckling was first observed in the southwest flange. Upon later cycles of increasing drift demands, buckling of the beam was clearly visible and strength degradation of the connection and subsequent loss in PT forces occurs. The moment vs. drift response and PT force vs. drift response for Specimen W76- PT2¼ is presented in Figure 2.18. Buckling is observed clearly in the 6% drift cycles for this specimen. As can be seen in Figure 2.18 (a), the buckling and subsequent plastic shortening of the beam resulted in a near-zero PT force at the end of the test and a near-zero stiffness in the connection as it unloads and reloads around zero moment.

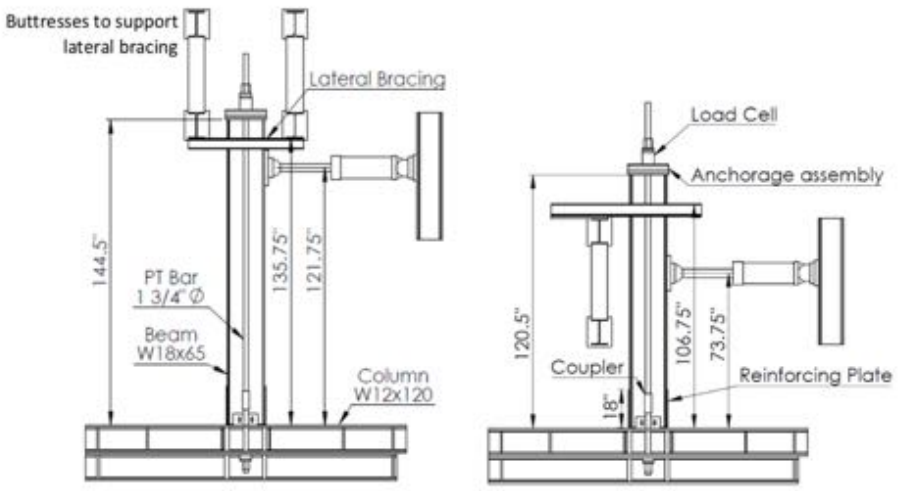

Figure 2.15: Test configuration of post-tensioned connections: (a) Specimen W65-PT1¾; (b) Specimen W76- PT2¼ [Hulsey., 2015]

(a) (b)

Figure 2.16: Buckling shape at the end of the tests: (a) Specimen W55-PT1¾; (b) Specimen W76- PT2¼ [Hulsey., 2015]

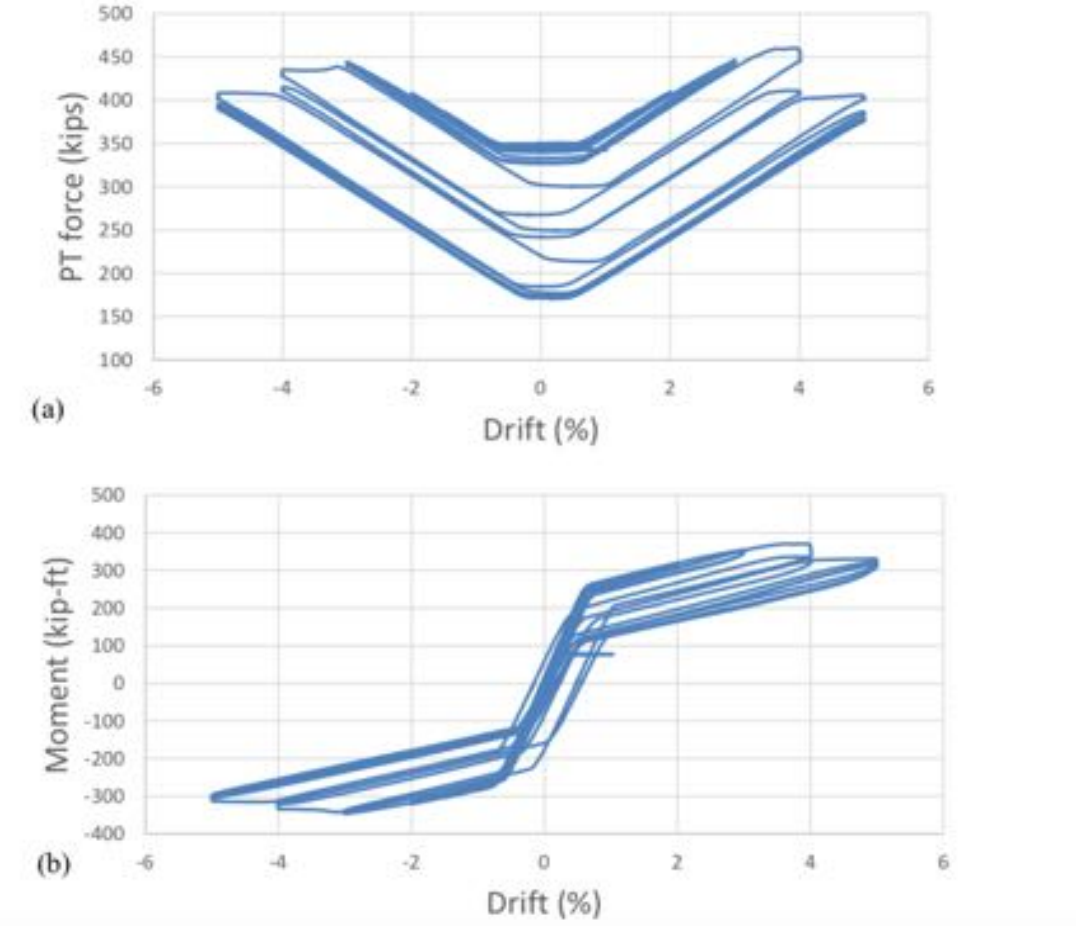

Figure 2.17: (a) PT force vs. drift and (b) moment vs. drift responses for Specimen W55-PT1¾ [Hulsey., 2015]

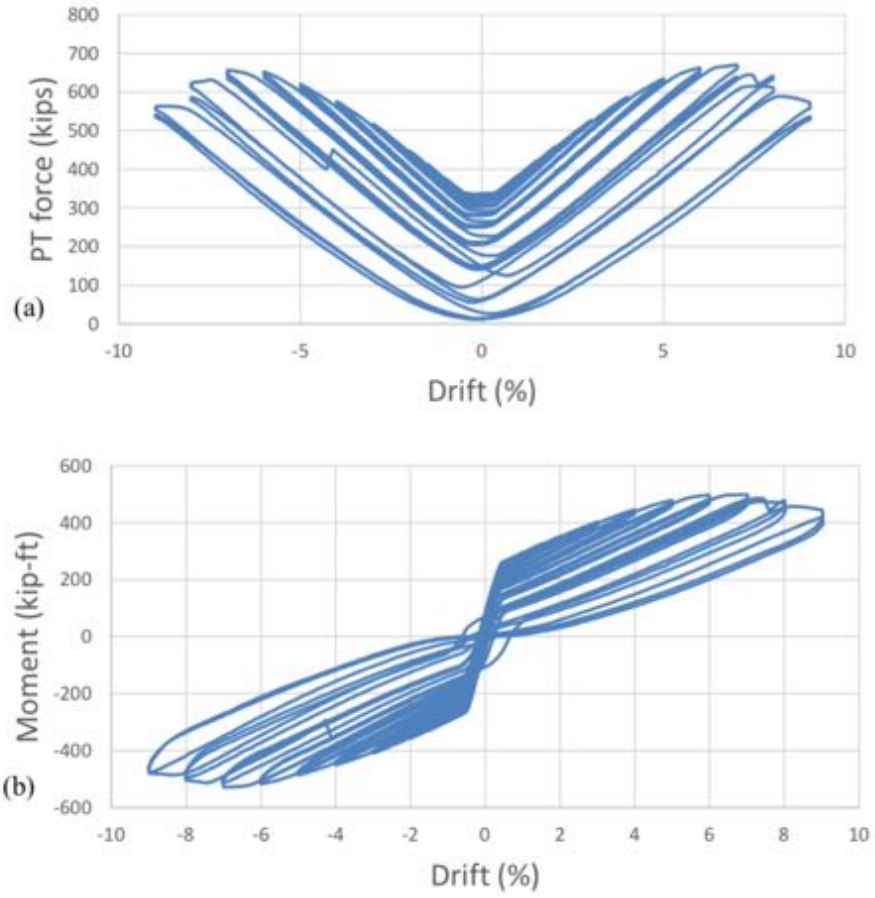

Figure 2.18: (a) PT force vs. drift and (b) moment vs. drift responses for Specimen W76-PT2¼ [Hulsey., 2015]

2.4 FINITE ELEMENT MODELING OF POST-TENSIONED CONNECTIONS

Esposto – [2008]

Esposto used the ABAQUS (2006) finite element software to investigate the seismic performance of post-tensioned connections. The reference experiment chosen for the research is Christopoulos et al. (2002), in which post-tensioned connections with buckling restrained ED bars are investigated. Each structural component is modeled with C3D8R continuum solid elements with reduced integration. Material models are defined

using true stress and strain values obtained from the engineering stress-strain results. The rigid interfaces between reinforcing plates and beam, anchorage assembly and PT bars, contact plate and beams, and the continuity plates and column are defined using tie constraints in ABAQUS. ED bars are attached to confining cylinders on both ends, and these cylinders are attached to the beam flange in one end and to the column continuity plates on the other end. The rocking behavior between the contact plates and the column are assigned as a contact interaction in ABAQUS. The contact behavior in ABAQUS includes *hard* contact normal to the interaction surface and *frictional* behavior tangential to the surface.

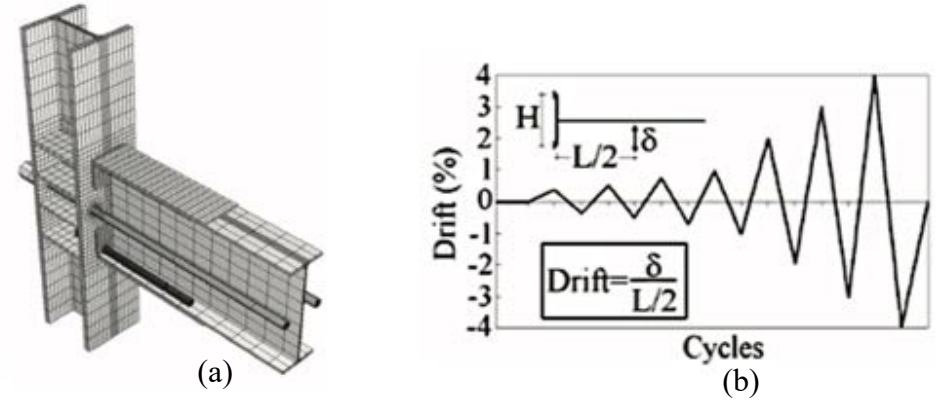

Figure 2.19: (a) Mesh of connection region; (b) applied loading protocol [Esposto., 2008]

Figure 2.19 (a) shows the mesh of the connection region. The authors used a meshing technique based on the tie constraint and contact interaction assignment where retained surfaces have a denser mesh compared to the corresponding constrained surface. For example, contact plates are assigned as retained surfaces and have a denser mesh compared to the column flange, which are defined as the constrained surface. Loading is applied in two steps. First, initial PT forces are applied to the structure using the *bolt load*

function in ABAQUS. Secondly, cyclic displacement-controlled loads are applied as performed in the experiments as shown in Figure 2.19 (b).

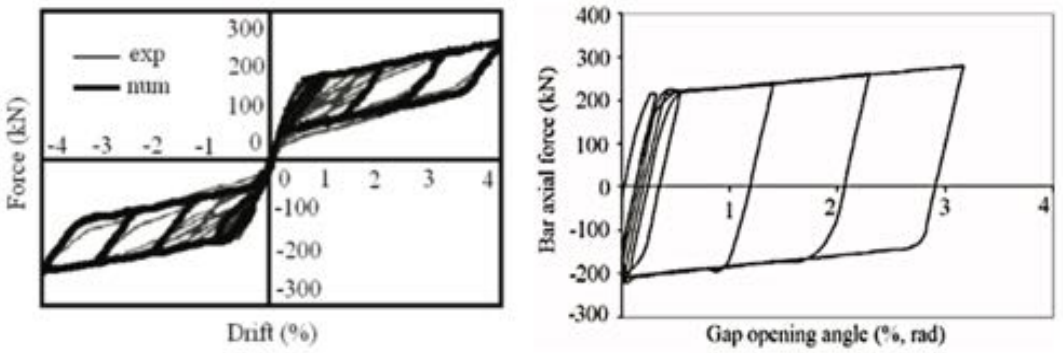

(a) (b)

Figure 2.20: (a) Experimental and numerical results; (b) response of ED bars [Esposto., 2008]

The comparison of experimental vs. numerical results is given in 2.20 (a) for the global response of the connection. According to the figure, the authors' numerical model compares well with the experimental test results. The authors also investigated the behavior of each member in the connection, particularly those members whose behavior was not explicitly measured during the experimental tests. For example, Figure 2.20 (b) shows the response of the ED bars.

Moradi and Alam – [2015]

Another example of detailed finite element modeling of post-tensioned connections is conducted by Moradi et al. (2015). The authors used the ANSYS (ANSYS 15) finite element software to develop three-dimensional models of the tests conducted by Ricles et al. (2002). Each connection element, including the bolts, are modeled using solid elements

as shown in Figure 2.21 (a). To reduce the computational time, symmetry conditions are assigned in the vertical plane. In addition, the authors presented techniques to prevent convergence problems in modeling of the contact interaction between the beams and columns.

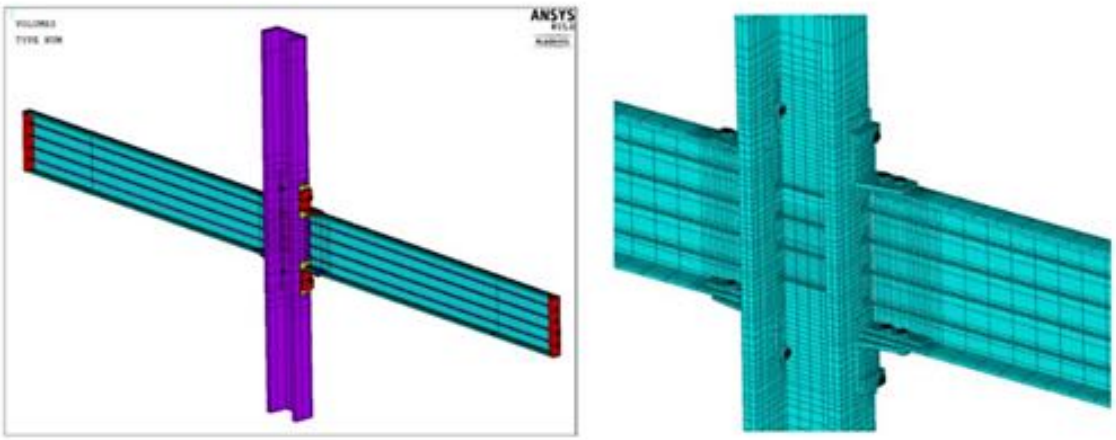

(a) (b)

Figure 2.21: (a) ANSYS model of the connection; (b) mesh of the connection region [Moradi et al., 2015]

In the finite element model, finer meshes are applied in places closer to the beam-column contact interface as shown in Figure 2.21 (b). All contact surfaces have a friction coefficient of 0.4, such as surfaces between the vertical angle leg and the shim plate, the horizontal angle leg and beam flange, and the PT bars and holes in the column flanges. The loads are applied in two steps, first preloads of bolts and PT strands are applied, then displacement-controlled cyclic loading with drift amplitudes of 0.1, 0.2, 0.3, 0.4, 0.5, 0.7, 1, 1.5 2, 2.5 and 3% are applied. Geometric nonlinearity is considered in the analysis, and no initial imperfection is assigned to the connection.

Figure 2.22 (a) shows the accuracy of the numerical model in capturing the global behavior of the connection. Figures 2.22 (b) and (c) show the FE model and experimental, respectively, local deformations of the yielding angle at the end of the test. According to the results, the authors showed that the proposed solid element FE modeling approach can capture the response of the post-tensioned connections with top and seat angles.

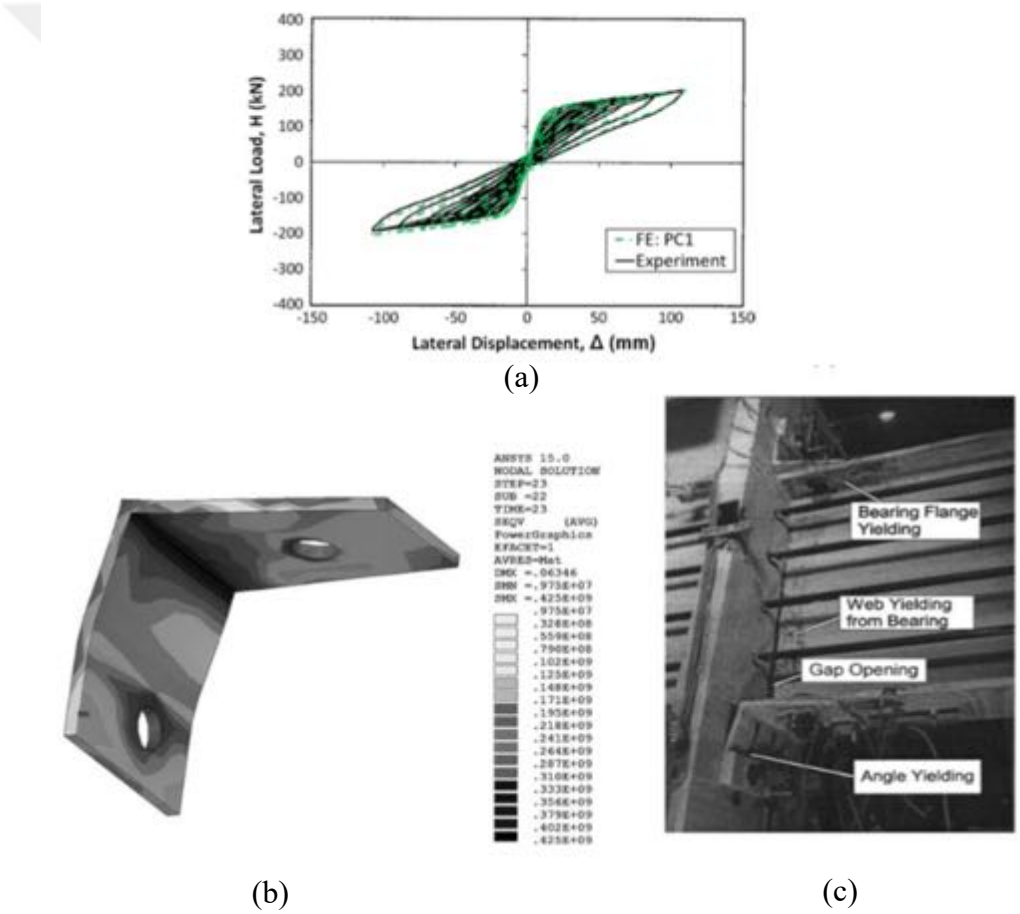

(a)

(b) (c)

Figure 2.22: (a) Numerical and experimental results; (b) yielding and deformation of the angles in the FE simulation; (c) experimental photo of angle yielding [Moradi et al., 2015]

Kim – [2008]

In this research, Kim performed numerical studies of experiments conducted by Kim and Christopoulos (2008). The researcher included two different numerical modeling approaches: One is a more simplified discrete spring model using frame elements, and the second one is a detailed FE model performed in ANSYS. A summary is provided here for the detailed FE models as they are most applicable to the current research.

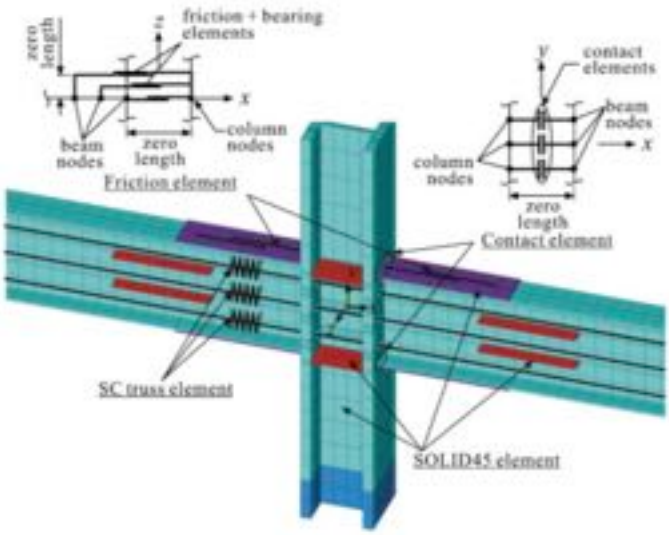

Figure 2.23: ANSYS model of the connection and details of friction and contact elements [Kim et al., 2008]

FE analysis is performed in ANSYS by modeling reinforcing plates, beams, columns, web stiffeners and continuity plates as solid elements as shown in Figure 2.23. Post-tensioning elements are assigned as truss elements using LINK1 in ANSYS. Initial force is applied as initial strain in the truss elements. Contact interaction is defined using CONTAC12 elements in ANSYS. The normal stiffness of the contact element is obtained by a trial-and-error process to provide computational efficiency and accuracy and is

defined as 15-20 times the axial stiffness of the beam as suggested by the authors. The tangential behavior of the contact element is defined by the friction coefficient, taken as 0.3. Finally, the frictional energy dissipating devices are modeled as LINK1 elements, and bolt-bearing effects are modeled with LINK10 compression-only elements with an initial gap of 25 mm.

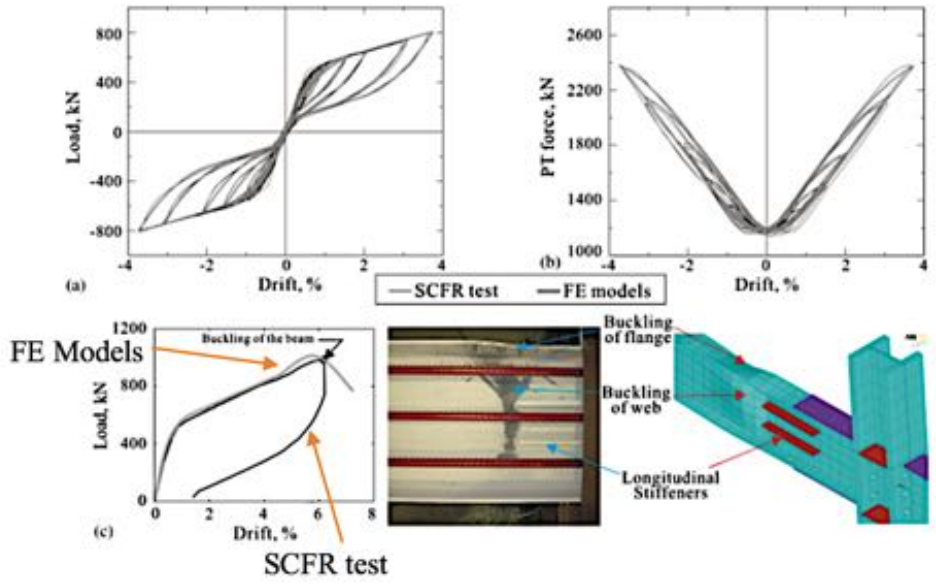

Figure 2.24: Experimental and numerical results for: (a) load vs. drift response; (b) PT force vs. drift response; (c) load vs. drift response, photo, and ANSYS model results of further applied drifts resulting in beam local buckling [Kim et al., 2008]

Figure 2.24 (a) and (b) show global response comparisons of numerical and experimental results. These figures show that the proposed modeling details can simulate self-centering and energy dissipation properties of post-tensioned connections. Finally, similar to the experiments, the authors applied drifts up to 6.2% and beyond to investigate the FE model's ability to capture the beam local buckling limit state observed in the test.

The results in Figure 2.24 (c) show that the proposed numerical model can simulate beam local buckling as shown by the gradual loss of strength of the FE model around 6.2% drift.

Clayton, Tsai, Berman and Lowes – [2015]

Clayton et al. performed numerical modeling comparisons for self-centering plate shear walls. In addition to looking at different methods of modeling the web plates of the SC-SPSW system, the authors proposed different modeling techniques for the PT boundary frame elements. Two different modeling approaches are introduced; the first one is more simplified line element models in the OpenSees simulation platform (McKenna 1997), and the second one is shell element modeling of the elements in ABAQUS.

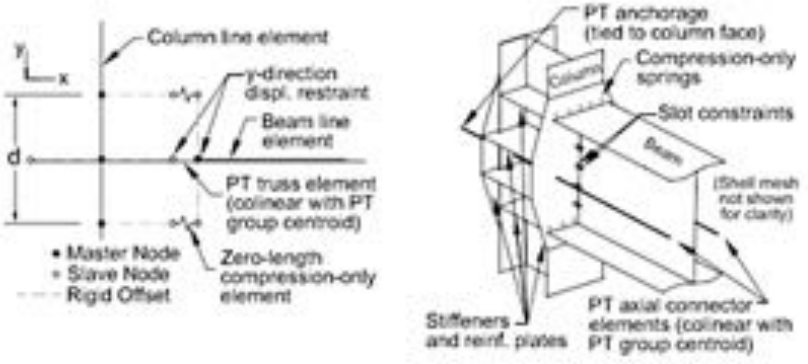

(a) (b)

Figure 2.25: (a) Line element models; (b) shell element models [Clayton et al., 2015]

The proposed line element model consists of modeling the beams and columns as nonlinear forced-based, distributed plasticity beam-column elements in OpenSees, and post-tensioning elements are modeled as truss elements with initial stress as shown in Figure 2.25 (a). Contact interaction between the column flange and beam flange is provided by zero length compression-only spring elements. Vertical direction translational restraints are assigned to provide shear transfer at the beam ends.

The details of the shell element ABAQUS model are shown in Figure 2.25 (b). S4R elements are used to model the stiffeners, reinforcing plates, beams, and columns. Compression-only springs, or connector elements, along the ends of the beam flanges are used to simulate the rocking behavior of the connection. PT elements are defined using axial connecter element with an initial stress. Slot constraints are assigned at the same location of the horizontally slotted shear tab in the test specimen, and out-of-plane restraints are located at the same locations as the test specimen.

2.5 Fiber-Based and Deterioration Modeling of Moment-resisting Frames

For frame element models of moment frames, which are commonly used in large system-level simulations, deterioration behaviors are often modeled using nonlinear concentrated plastic hinge models and distributed plasticity models. Concentrated plasticity models are typically defined using nonlinear zero-length rotational springs in moment frame beams at the location of expected plastic hinging. Different concentrated plasticity deterioration material models have been proposed for moment frames elements. Ibarra and Krawinkler (2005) proposed a hysteretic model to capture cyclic strength and stiffness deterioration as well as loading and reloading stiffness reduction in beams and columns. Following this research, Lignos and Krawinkler (2010, 2011, and 2012) extended the deterioration model proposed by Ibarra and Krawinkler (2005) and developed empirical equations to obtain the key degradation parameters for wide-flange steel beams and hollow structural section columns. However, the nonlinear concentrated plastic hinge models defined as a predefined moment vs. rotation behavior cannot capture the effects of variation in axial load, which is an important parameter for post-tensioned connections. An extensive literature review on deterioration modeling in concentrated plasticity models can be found in Lignos (2008) and Suzuki (2018).

Distributed plasticity models are also proposed to model yielding and strength deterioration in moment frames. Distributed plasticity models can be displacement-based or force-based elements, where nonlinearity can be captured using fiber cross-sections at element integration points. Displacement-based method follows standard finite element procedures, in which section forces are interpolated from an approximate displacement field (constant axial deformation and linear curvature distribution are enforced); while force-based method is based on exact force interpolation functions (constant axial force and linear moment distribution for elements without in-span loading). Advantages of using force-based elements over displacement-based elements to evaluate nonlinear response of moment frames elements is extensively explained in Neuenhofer and Filippou (1997). To overcome localization problems in distributed plasticity models, Scott and Fenves (2006) proposed force-based beam-columns with predefined plastic hinges that contains two finite-length plastic hinges at the ends of the beam and a linear elastic mid-section. Fiber cross-sections can capture axial-flexural interaction that concentrated moment-rotation springs cannot. In this section, two different studies on the deterioration modeling of beams and columns using fiber-based elements will be presented.

Suzuki – [2018]

Suzuki proposed a uniaxial equivalent stress-strain behavior to capture strength and stiffness degradation in hollow structural section (HSS) columns. In this study, experimental tests were conducted for different sizes of HSS columns with various axial loading protocols. To obtain uniaxial stress-strain material behavior to implement in fiber sections, stub column FE models are simulated first with monotonic axial load and then cyclic axial loading, including symmetrical incremental strain amplitudes up to $\pm$5%, constant amplitude of $\pm$5%, decrementing amplitude from $\pm$5%, and an asymmetric strain

protocol. Figure 2.26 shows the buckling length obtained from the simulation and experimental results. Authors concluded that the buckling length could be generalized as equal to the *0.8 D*, where *D* is the depth of HSS column.

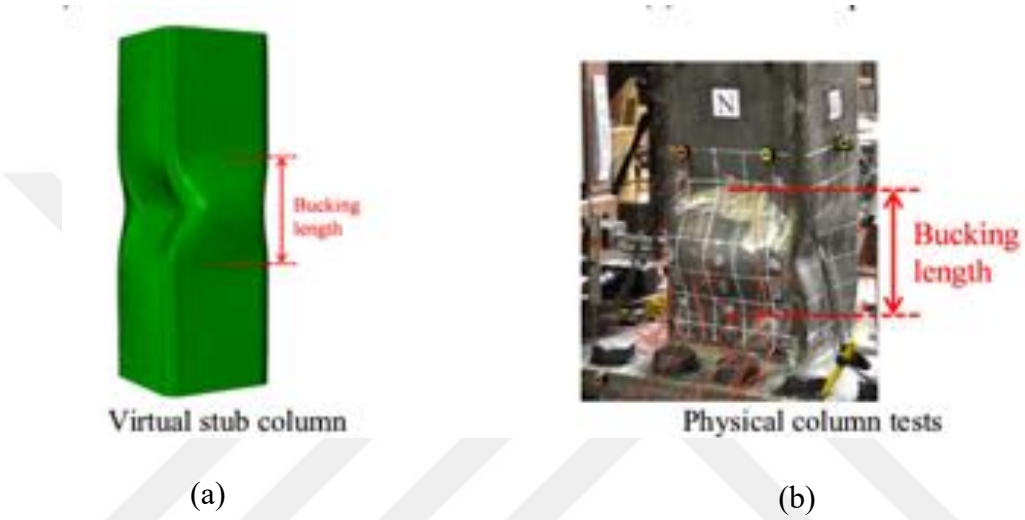

Figure 2.26: Obtained buckling length of (a) virtual stub column and (b) physical column tests [Suzuki, 2018]

The uniaxial equivalent stress-strain relationship to use in more simplified fiber-based element models is extracted over the defined buckling length from the stub column parametric studies. The equivalent stress-strain relationship obtained from the FE element models (shown as the black line in the figure) under different types of cyclic axial loading protocols as given in Figure 2.26, along with the proposed simplified stress-strain model (shown as the red line in the figure).

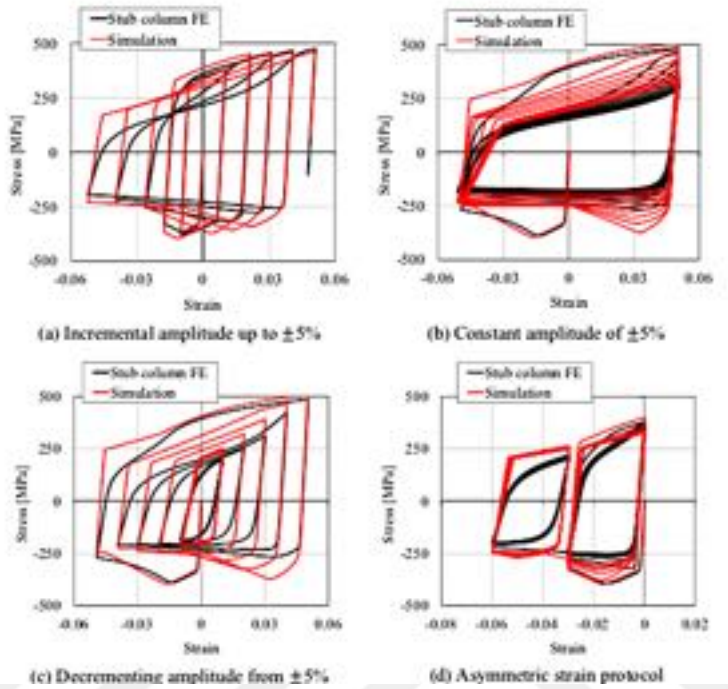

Figure 2.27: Extracted equivalent stress-strain relationship for different axial loading protocols [Suzuki, 2018]

The key backbone, or monotonic, parameters for the proposed equivalent stress-strain model are given in Figure 2.28 (a). The authors obtained empirical equations to define the key points. The key parameters for cyclic behavior are shown in Figure 2.28 (b) for compressive behavior and in Figure 2.28 (c) for the tensile behavior. The constitutive relationship for the compressive behavior includes four distinct regions: elastic behavior, post-yield behavior defined by combined isotropic and kinematic hardening, a strength degradation slope, and a continued degradation region with a lower slope. To obtain the cyclic deterioration model, the energy-based deterioration rule developed by Rahmana and Krawinkler (1993) is applied by the authors.

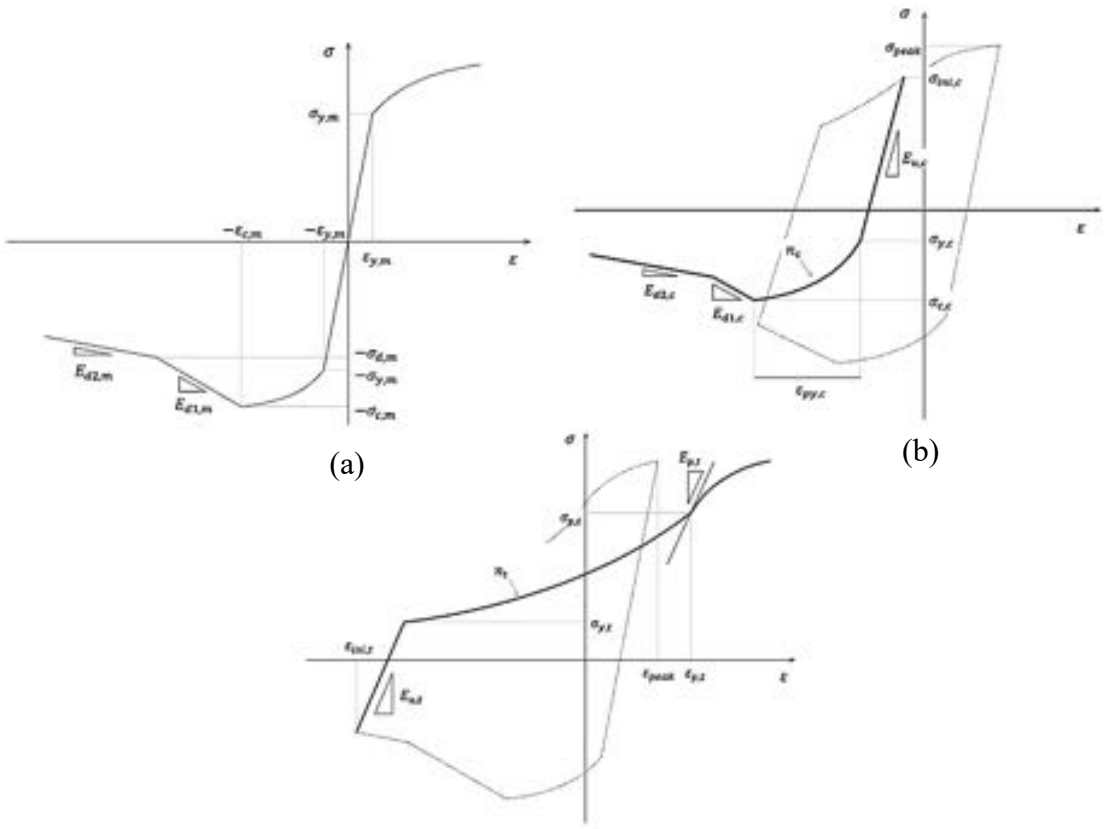

Figure 2.28: Extracted equivalent stress-strain relationship: (a) monotonic loading, (b) cyclic loading compressive behavior, (c) cyclic loading tensile behavior [Suzuki, 2018]

The proposed constitutive relationship is implemented in force-based beam-column elements with predefined hinges, where the midpoint hinge integration method is used, as shown in Figure 2.29. The authors pointed out that the reason for using the midpoint hinge integration method is that due to the effect of axial loads, the location of the highest moment demands will be away from the column base, as compared to the beams where the highest flexural demands are observed at the beam ends.

Finally, Figure 2.30 shows the validation of the proposed deterioration models with an experimental test of a HSS column subjected to constant axial load and cyclic moment

demands. According to the figures, the authors concluded that the proposed constitutive relationship for fiber-based elements could simulate strength degradation under different loading protocols, as well as axial shortening of the columns. The authors noted that the proposed model is not suitable for simulating the hysteretic behavior of wide-flange steel columns due to coupled local and lateral torsional buckling, particularly in the case of deep and slender wide-flange steel columns.

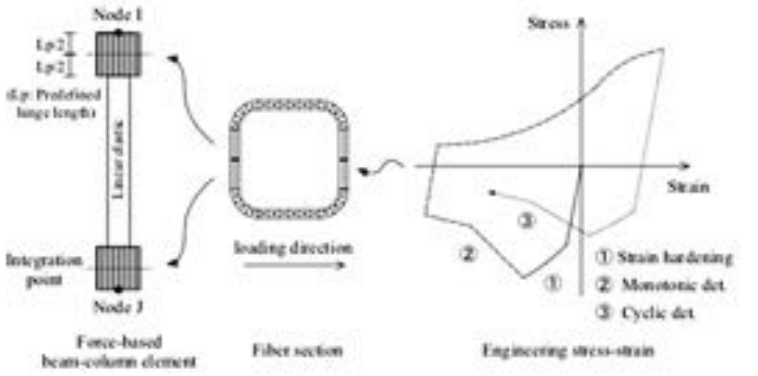

Figure 2.29: Application of equivalent stress-strain relationship with midpoint hinge integration [Suzuki, 2018]

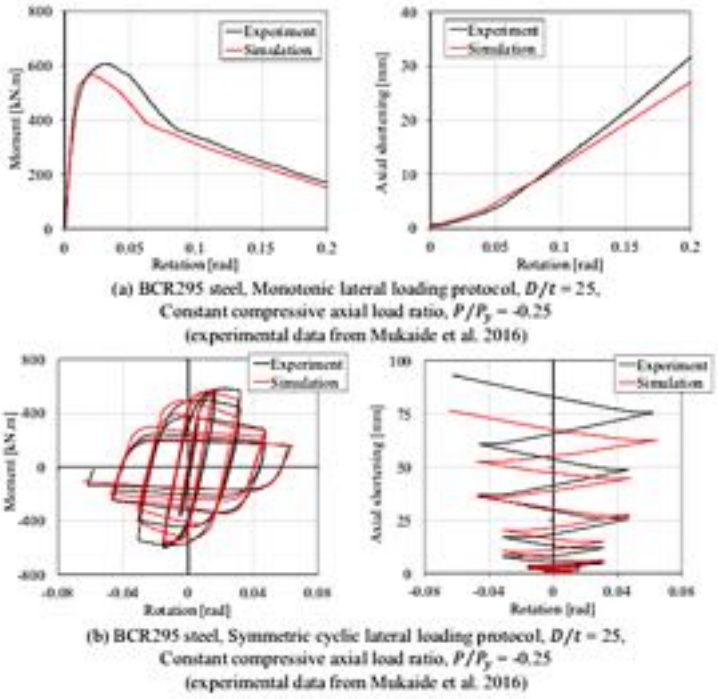

Figure 2.30: Verification results of equivalent stress-strain relationship applied to cantilever HSS columns [Suzuki, 2018]

Kolwankar, Kanvinde, Kenawy, Lignos and Kunnath – [2018, 2019]

The authors proposed an equivalent nonlocal material model for displacement-based fiber elements to simulate local buckling-induced softening. For the nonlocal formulation, strain at any location is computed from strains at neighboring locations as a weighted average by introducing a length scale (Kolwankar et al., 2018). This method is proposed to overcome mesh dependency in modeling of the softening behavior of frame members. Figure 2.31 shows the process used to develop the proposed nonlocal fiber element formulation. First, the localization or buckling length, which is the characteristic length for the nonlocal formulation, is obtained from continuum FE models and is found to be 1.5 times the beam flange width for monotonic loading as shown in Figure 2.32 (a).

Following this step, effective stress-strain data is extracted from the FE simulations under monotonic loading, shown in Figure 2.32 (b). For the effective stress-strain constitutive relationship, longitudinal stresses are obtained at a location just outside of the buckling length, and strains are determined from the shortening of the beam in the buckled region (net displacement divided by the buckling length). Both stresses and strains are obtained by averaging through the flange width. The key parameters defined in Figure 2.32 (b) are obtained through empirical equations developed based on the results of FE simulations.

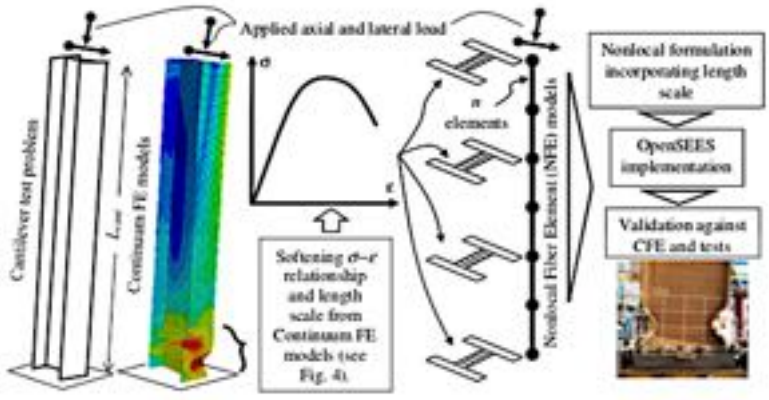

Figure 2.31: Process for development of nonlocal formulation [Kolwankar et al., 2018]

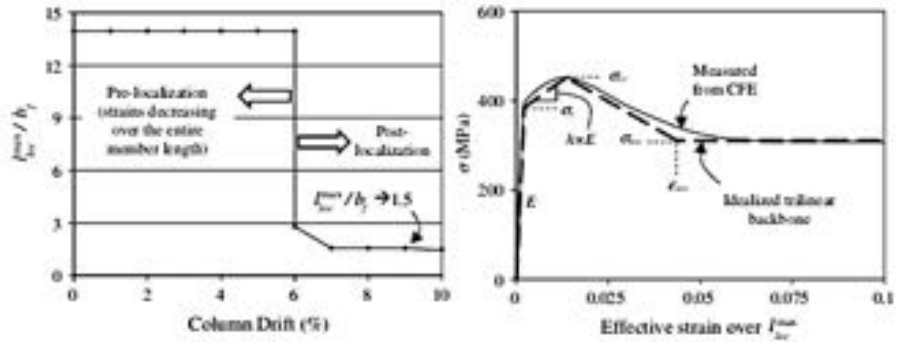

(a) (b)

Figure 2.32: (a) Localized buckling length; (b) FE extracted effective stress-strain behavior [Kolwankar et al., 2018]

In Kolwankar et al. (2019), the authors implemented the nonlocal formulation in displacement-based fiber element models of wide-flange steel columns subjected to cyclic lateral loading. The results are compared with the experiments conducted by Elkady and Lignos (2018a). Similar to the authors' previous research, the effective stress-strain behavior is obtained from the FE simulations. Stresses are obtained at a location adjacent to the buckling length, and strains are obtained as the net shortening of the buckling length divided by the gauge length. The gauge length, or the buckling length, is obtained as 2.25 times of the beam flange width for cyclic loading, which is different than the 1.5 times the beam flange width previously proposed for monotonic loading. The research is focused on laterally braced beam-columns such that the observed softening behavior is due to local buckling, not lateral torsional buckling. Figure 2.33 shows the approach the authors used to develop the nonlocal fiber element formulation. First, FE simulations are validated against experimental results and then effective stress-strain behavior is extracted over the buckling length in the FE simulations. Empirical equations are obtained based on flange slenderness ratio using statistical regression analysis, similar to the previously developed monotonic relationship. The proposed stress-strain models are applied to both the beam flanges and web to simulate local buckling-induced softening. The authors pointed out that the empirical equations that are defined based on the flange slenderness ratio can be also obtained using web slenderness, yet it is concluded that equations obtained based on flange slenderness ratio can more accurately simulate the strength degradation behavior.

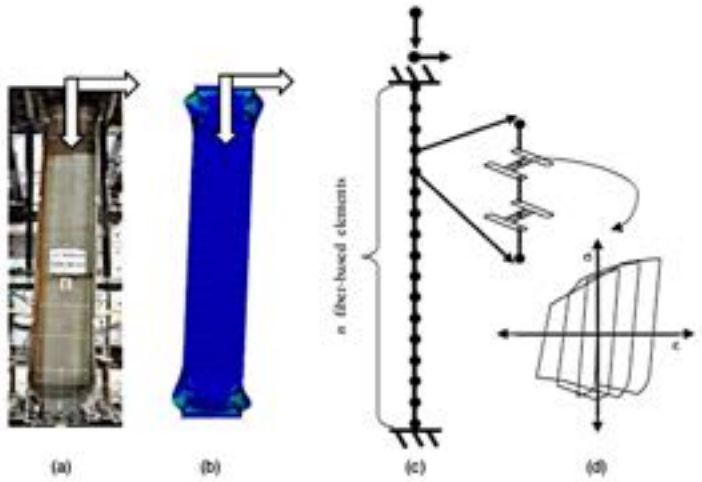

Figure 2.33: (a) Experimental tests, (b) FE simulations, (c) fiber elements, (c) effective stress-strain relationship extracted from the FE analyses [Kolwankar et al., 2019]

2.6 Modelling of Strength Degrading Behavior in PT Connections

Kamperidis – [2016]

Kamperidis developed a novel damage-free self-centering column base connection for earthquake-resilient buildings. Web-hourglass shape steel pins (WHPs) are used in post-tensioned column bases to dissipate seismic energy, while self-centering is provided by PT forces. To test the performance of the proposed post-tensioned column base connections under earthquake loads, the author conducted OpenSees simulations using a model that is calibrated against experimental results from Vasdravellis et at. (2013b). Details of the PT beam-to-column connections in the OpenSees model are shown in Figure 2.34.

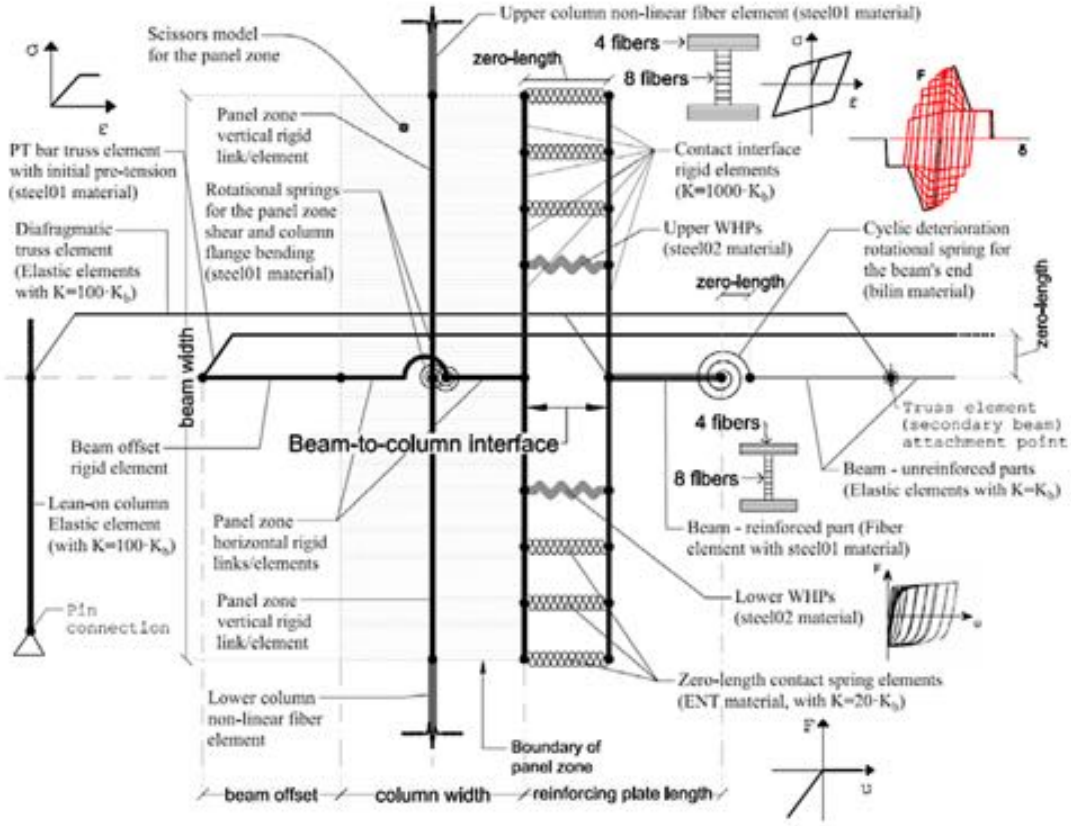

Figure 2.34: Details of OpenSees model of post-tensioned connection [Kapmeridis, 2016]

Based on the focus of the current research, the details for modeling the beam elements in the PT connections are explained here, and the details of the complete OpenSees model are explained in Kamperidis (2016). The portions of the beams with reinforcing plates are modeled with nonlinear force-based beam-column fiber elements. According to previous research, beam local buckling is expected to occur at the end of the reinforcing plates; therefore, the unreinforced parts of the beams are modeled as elastic elements with zero-length rotational springs at their ends to simulate the stiffness and strength degradation induced by beam local buckling. The *bilin* material (Ibarra-Medina-

Krawinkler model) in OpenSees is assigned to the zero-length rotational springs. The authors performed pushover analysis of the designed frame and showed that local buckling of the beams occurred when the moment in the frame lateral strength reaches its peak value.

Ahmadi, Ricles and Sause – [2018]

The authors conducted incremental dynamic analyses using the methodology presented in FEMA P695 (2009) for a four-story perimeter steel self-centering moment-resisting frame (SC-MRF) with web friction devices (WFDs) to investigate the seismic collapse resistance of self-centering moment-resisting frames. The details of the prototype building are given in Figure 2.35, which is designed by Lin (2012). Authors developed an alternate design by reducing the limit for the PT strand stress under the maximum considered earthquake (MCE) to investigate the influence of the PT strand force limit on the seismic collapse resistance of an SC-MRF. The reinforcing plate length is increased in the alternate design to accommodate increased PT forces as a result of increased number of PT strands.

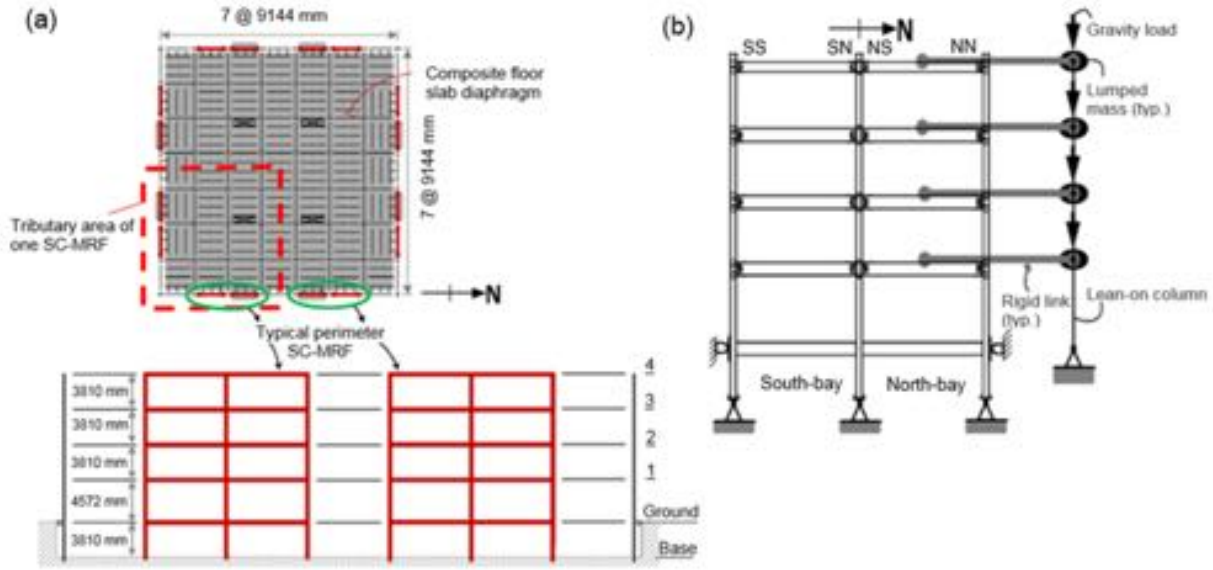

Figure 2.35: The prototype building of SC-MRFs with WDFs [Ahmadi et al., 2018]

The incremental dynamic analyses are performed in the ABAQUS finite element program (2013). Details of the ABAQUS model are shown in Figures 2.36 (a) and 2.36 (b). Finite element models are simplified to improve computational efficiency by using the eight-node shell (S8R) element only in the portion of the beam just beyond the end of the reinforcing plate, since this is the region where local buckling is expected to occur, whereas the rest of the beam is modeled as elastic line elements. Gap elements are used to simulate rocking behavior, and the stiffness of the gap element is chosen through calibration with the experimental results of Lin (2012). The accuracy of the proposed model is tested through comparison with a completely shell element model of an interior connection tested by Garlock (2002) as shown in Figure 2.36 (a). In addition to being used to evaluate the accuracy of the proposed model, Garlock (2002) test results are also used to calibrate initial imperfections assigned to the beam shell model. According to ABAQUS results, the

authors concluded that the simplified FE models can adequately capture the beam local buckling response and subsequent loss in PT forces.

After validation of the simplified ABAQUS models, the authors conducted static pushover analyses to investigate lateral load-roof drift behaviors of the different frame designs, and finally seismic collapse fragility analyses are conducted. The authors concluded that seismic collapse of an SC-MRF under extreme ground motions is mainly governed by the initiation of inelastic local buckling and subsequent axial shortening in the beams that lead to loss in PT strand force. Therefore, accurate modeling of beam local buckling is essential in investigation of seismic performance of SC-MRFs.

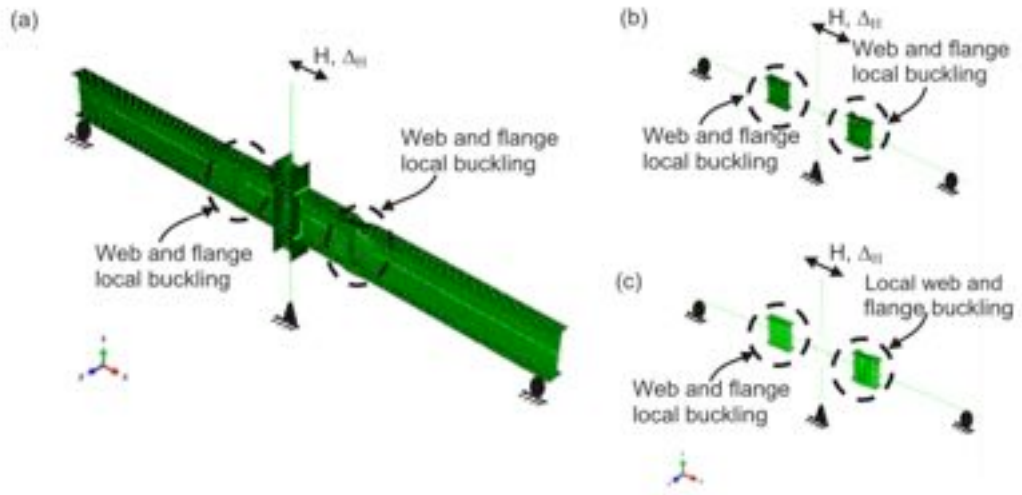

Figure 2.36: (a) Details of ABAQUS model with complete shell elements, (b) simplified ABAQUS model, (c) buckling of the beam at the end of reinforcing plates [Ahmadi et al., 2018]

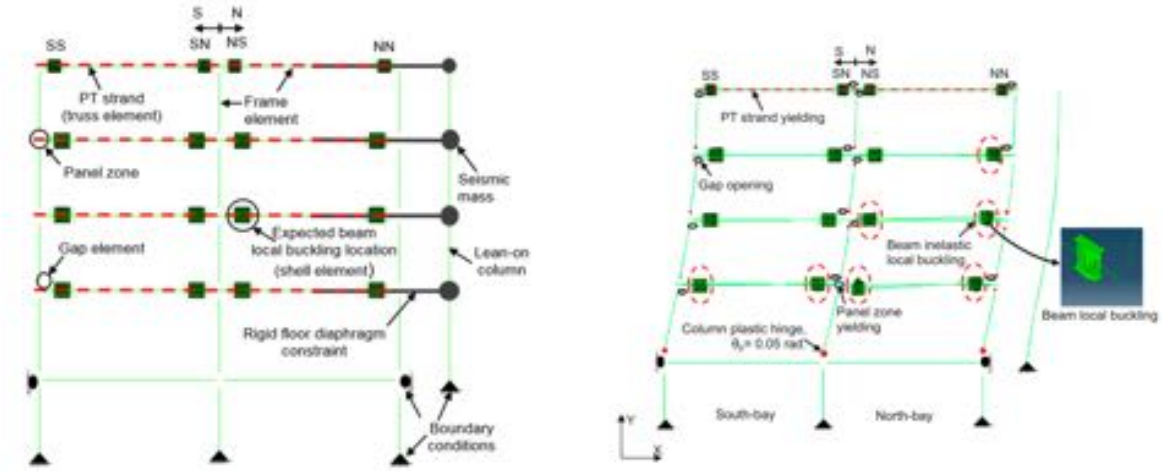

(a) (b)

Figure 2.37: (a) Details of simplified ABAQUS model of prototype building, (b) at collapse [Ahmadi et al., 2018]

Although this modeling technique can be used to evaluate the collapse resistance of SC-MRFs, it requires large computational time due to frame modeling with shell elements and the large number of dynamic analyses required for a collapse fragility study, which is very time consuming in ABAQUS. Therefore, simpler and more computationally efficient models capable of capturing local buckling-induced strength degrading behaviors should be developed for more widespread study of seismic collapse performance of self-centering systems that employ post-tensioned connections.

Chapter 3: Finite Element Models of Self-Centering Moment-Resisting Frame Connections

3.1 INTRODUCTION

Self-centering moment-resisting frames are designed for beams and columns to stay essentially elastic and provide energy dissipation through specific yielding or friction elements during an earthquake. However, due to the rocking behavior within post-tensioned connections, high compressive forces could occur in the beam flanges and can subsequently lead to local buckling and plastic shortening of the beams and subsequent loss in post tensioned (PT) force. This phenomenon results in reduced moment capacity and self-centering capability of the PT connection. Modeling the strength degrading behavior of these connections caused by the buckling limit state is necessary to investigate collapse performance of moment frames employing PT connections. While other limit states like PT bar or strand yielding, can occur and result in loss of connection capacity, previous research (Garlock, 2002; Ahmadi et al., 2018) has shown that beam local buckling is the most common limit state governing strength degradation behavior. The degradation in connection stiffness and moment capacity caused by beam local buckling could result in a reduction in lateral stiffness of the self-centering moment-resisting frames with PT connections and could lead to collapse. Experiments investigating beam local buckling limit state behaviors of PT beam-to-column connections are limited; therefore, experimentally validated finite element (FE) models can be used to further examine buckling-induced strength degradation behavior of these connections.

FE modeling of self-centering moment-resisting frames could provide insights into nonlinear behavior, earthquake performance, and detailing of these post-tensioned connections. Past research has been performed to develop FE models of self-centering connections; Kim and Christopoulos (2009) conducted FE analyses using solid

(continuum) elements. The FE results compared well with the experimental tests performed by Kim and Christopoulos (2009) for capturing the cyclic behavior of self-centering moment-resisting frames with beam local buckling. Another group of researchers, Moradi et al. (2015), used solid finite elements to simulate the behavior of PT steel connections with bolted yielding angles tested by Ricles et al. (2001). The authors used the experimentally validated FE models to conduct parametric studies on the effect of the reinforcing plates on connection performance, showing that the existence of reinforcing plates and their length can delay the onset of beam local buckling. Furthermore, Ahmadi et al. (2018) used FE models of PT connections with bolted yielding angles to study seismic collapse resistance of self-centering moment-resisting frames. The FE models were employed in incremental dynamic analyses to assess system collapse performance. Their models consist of shell elements in regions near the beam ends where local buckling may occur, and the local buckling behavior was validated against experiments conducted by Garlock (2002). They demonstrated that shell element-based FE models can predict the local buckling of beams accurately, and they stated that accurate modeling of beam local buckling is crucial to obtain proper assessment of the self-centering moment-resisting frame's collapse resistance.

This section describes the development of FE models to capture the behavior of self-centering PT connections at design and at ultimate drift levels, where elastic and strength degrading behaviors, respectively, are expected. The purpose of this chapter is to develop and to make modeling recommendations for FE models that capture strength degradation behavior due to beam local buckling. The FE models are validated against large-scale experimental test results from Hulsey (2015). The ABAQUS (2017) finite element program is used to model the PT beam-to-column connections and detailed descriptions of the modeling process are discussed. These models are implemented in

ABAQUS using both implicit static and explicit dynamic solution algorithms and associated element formulations, via ABAQUS/Standard and ABAQUS/Explicit, respectively. Experimental validation results and modeling recommendations for each of these analysis methods are discussed in this section.

Furthermore, this section explores the element types used to model post-buckling behavior of PT connections. Both shell elements and solid elements are used for modeling of the connections using ABAQUS/Standard, while only shell element models are used for ABQUS/Explicit analyses. Results from these analyses are compared with experimental results, and ultimately, shell element models are recommended for their relative computational efficiency and accuracy. Solid element results are only included for moment vs. drift response, while shell modeling results are included for connection moment vs. drift, PT element force vs. drift, and buckled shape.

The organization of this section is as follows: Section 3.2 presents a brief summary of the reference experimental work. Following this part, an overview of the PT connection model is provided in Section 3.3, whereas detailed explanations of the shell and solid element models are described in Sections 3.4 and 3.5, respectively. Section 3.6 compares results between experimental tests and ABAQUS/Standard FE models using both shell and solid elements, as well as ABAQUS/Explicit analysis shell element models. Finally, Section 3.7 provides a summary and recommendations for modelling of PT beam-to-column connections.

3.2 Reference Experiments

In this study, the experiments performed by Hulsey (2015) were selected to validate the finite element models. To isolate beam local buckling behavior, the experiments were conducted with a single beam-to-column connection. Additionally, energy dissipating

devices were not included in these experiments. A total of three specimens were tested with varying beam dimensions, PT bar diameters, initial post-tension forces in the PT bars, and reinforcing plate thicknesses. Each specimen consisted of a beam with two PT bars located on each side of the beam web, which are anchored in the column and at the end of the beam, as shown in Figure 3.1 (a). A summary of the test specimens' beam size, PT bar diameters, initial PT force, and reinforcing plate thicknesses is provided in Table 3.1. The specimens were loaded cyclically via an actuator as shown in Figure 3.1 (a). The length of the beams in the first two experiments (Specimens 1 and 2) were 144.5 inches with the actuator loading and lateral bracing located at 121.75 inches and 135.75 inches, respectively, from the column face, while the beam that was used in last experiment (Specimen 3) was 120.5 inches long with the actuator loading and lateral bracing located at 73.75 inches and 106.75 inches, respectively, from the column face. The purpose of changing the beam length and actuator location in the last specimen was to increase the drift capacity of the test set-up from 5% to 10% drift.

Table 3.1 Summary of Test Specimen Properties

Specimen Number	Beam Size	Beam Length (in)	Reinforcing Plate Thickness (in)	PT Diameter (in)	Initial PT Force (kips)		Total Initial PT Force (kips)
					Bar #1	Bar #2	
1	W18x65	144.5	0.50	1 ¾	187	185	372
2	W18x55	144.5	0.75	1 ¾	175.5	174.5	350
3	W18x76	120.5	0.50	2 ¼	166	170.5	336.5

A W12x120 column with a length of 13 ft was attached to the strong floor via an anchor column (shown as blue in Figure 3.1 (a)) with tie-down locations 12 ft apart. The

PT bars are anchored at the lower anchor column and at an anchorage assembly at the top of the specimen as shown in Figure 3.1 (a) and (b). The anchorage assembly consists of two 15x20 inch size plates with a thickness of 2 inch each, which were separated by four 2-inch-tall and 1 inch wide "webs" welded between the plates. The columns had 2-inch stiffeners or continuity plates located in line with the beam flanges so that the compression forces from the beam had a direct load path to the strong floor (Hulsey, 2015). The lengths of the reinforcing plates for all specimens were equal to the nominal beam depth, 18 inches, and their thicknesses varied with beam geometry as given in Table 3.1. As suggested by Ricles et al. (2002), a 2-inch-wide bearing plate was welded to the end of each beam flange and reinforcing plate to provide an even contact surface with the column face, as shown in Figure 3.1 (a) and (b). Although the beam-column contact surfaces are expected to provide adequate shear resistance through friction, due to the large normal forces produced, a shear tab (as seen in Figure 3.1) welded to the column and connected to the beam web with three 1-inch diameter A325 bolts and slotted holes allows for rotation of the beam relative to the column.

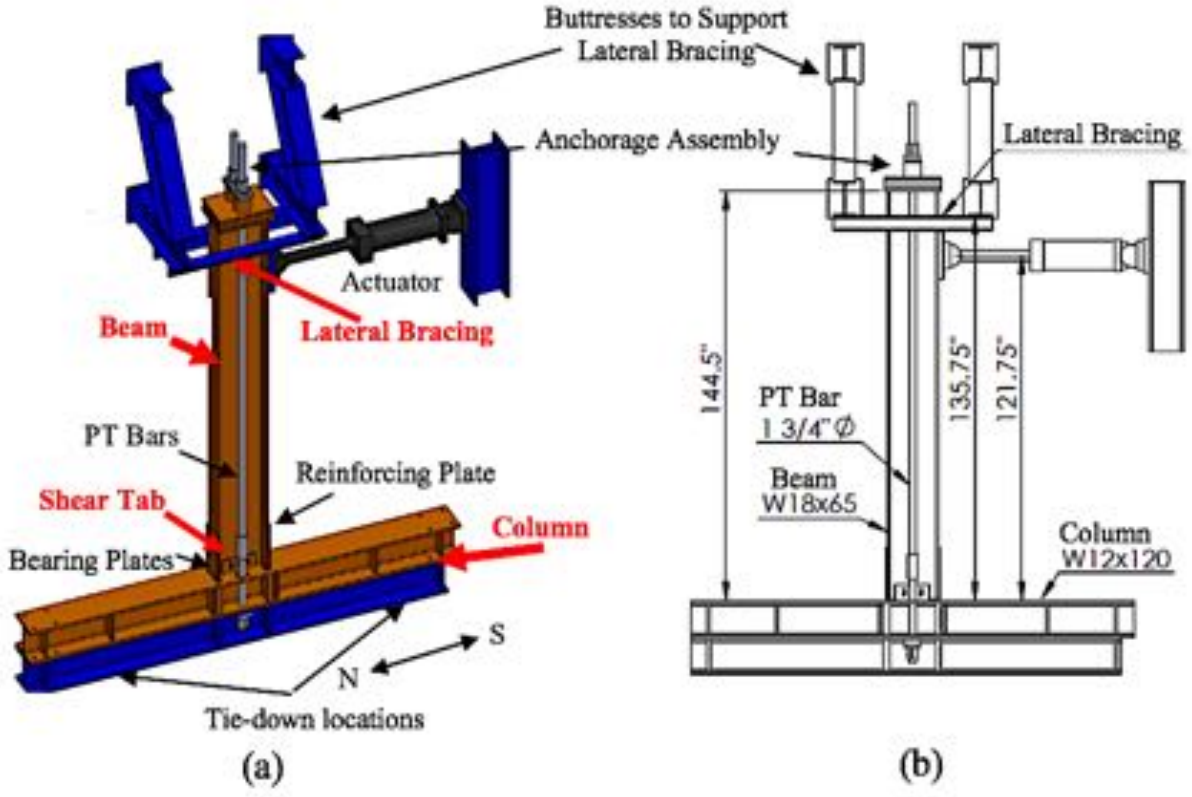

Figure 3.1: (a) Isometric view of test setup, and (b) detailed drawing of Specimen 2 [Hulsey, 2015]

Reinforcing plates, stiffeners, and bearing plates were made of 50 ksi steel, while the PT bars were made of high strength steel with an ultimate strength of 150 ksi in compliance with ASTM A722 specifications. Columns and beams were made of A992 steel material. To define material properties for beams, coupon tests were conducted at the Ferguson Structural Engineering Laboratory, results of which are presented in Section 3.2.1.

The loading sequence was based on the AISC *Seismic Provisions* (2010) requirements for beam-to-column connection testing. However, during the experiments to

reduce the number of cycles in the elastic range and shorten the test duration, the sequence was shortened as follows: 1 cycle at 0.375% drift, 4 cycles at 0.5% drift and 2 cycles at 0.75%,1%,1.5%,2%,3%,4%,5% (increasing at 1% drift increments up to 9% drift for the final specimen) as shown in Figure 3.2.

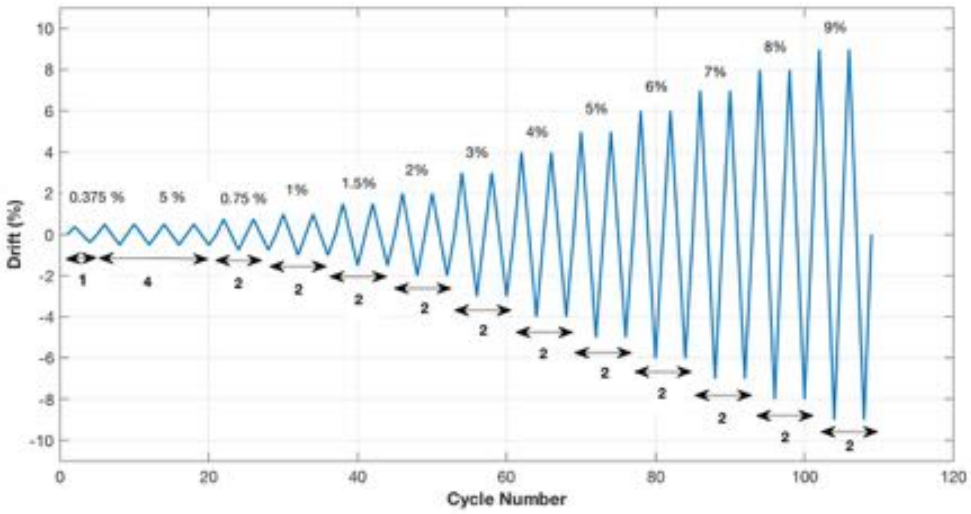

Figure 3.2: Displacement loading history of experimental work

Finally, LED markers used as part of the NDI Optotrak vision system were used to capture the three-dimensional displacements and buckled shape of the beam specimens. The detailed configuration of the LED markers will be presented in Section 3.6.4.

3.2.1 Tensile Coupon Tests

The column and beam sections are fabricated with ASTM A992 steel with a nominal yield strength of 50 ksi. The material properties of the beam sections are obtained from tensile coupon tests conducted at the Ferguson Structural Engineering Laboratory. Coupon specimens are extracted from the beam flanges and webs for each beam section. The engineering stress-strain results for the beam flanges and webs are given in Figures

3.3 and 3.4, respectively. Key material strength values are given in Table 3.2, where the yield strength was determined using the 0.02% offset rule and the ultimate strength is taken as the maximum measured stress. For structural steel members, the modulus of elasticity, *E*, is defined as 29,000 ksi.

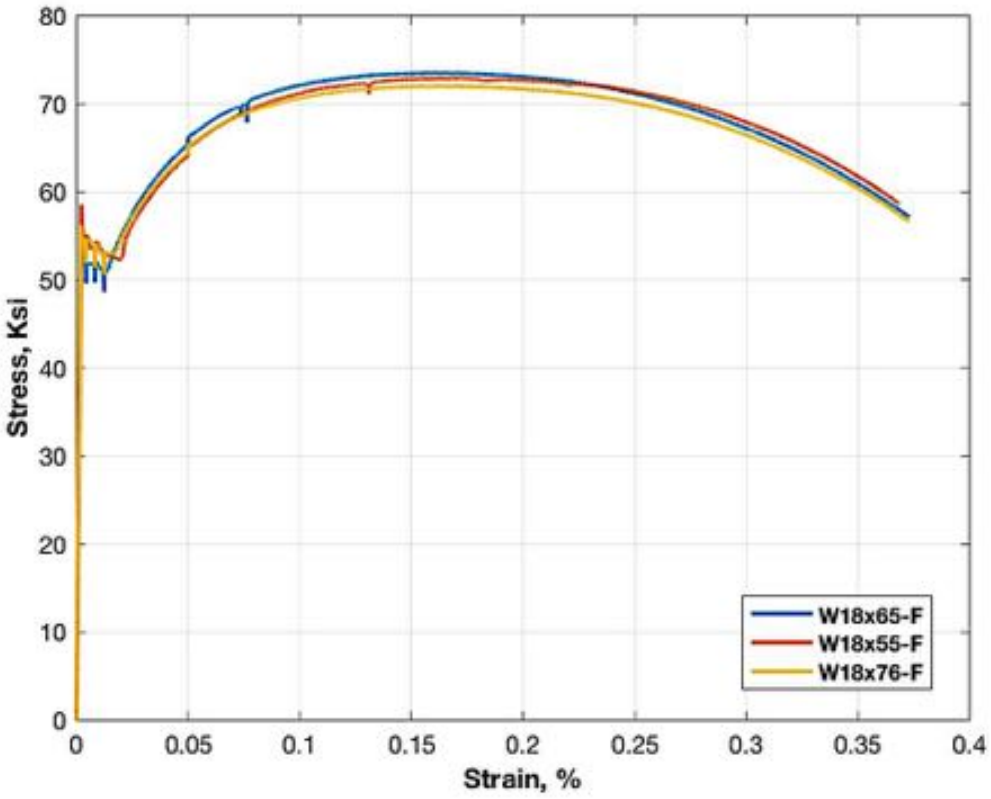

Figure 3.3: Engineering stress-strain response for beam flanges

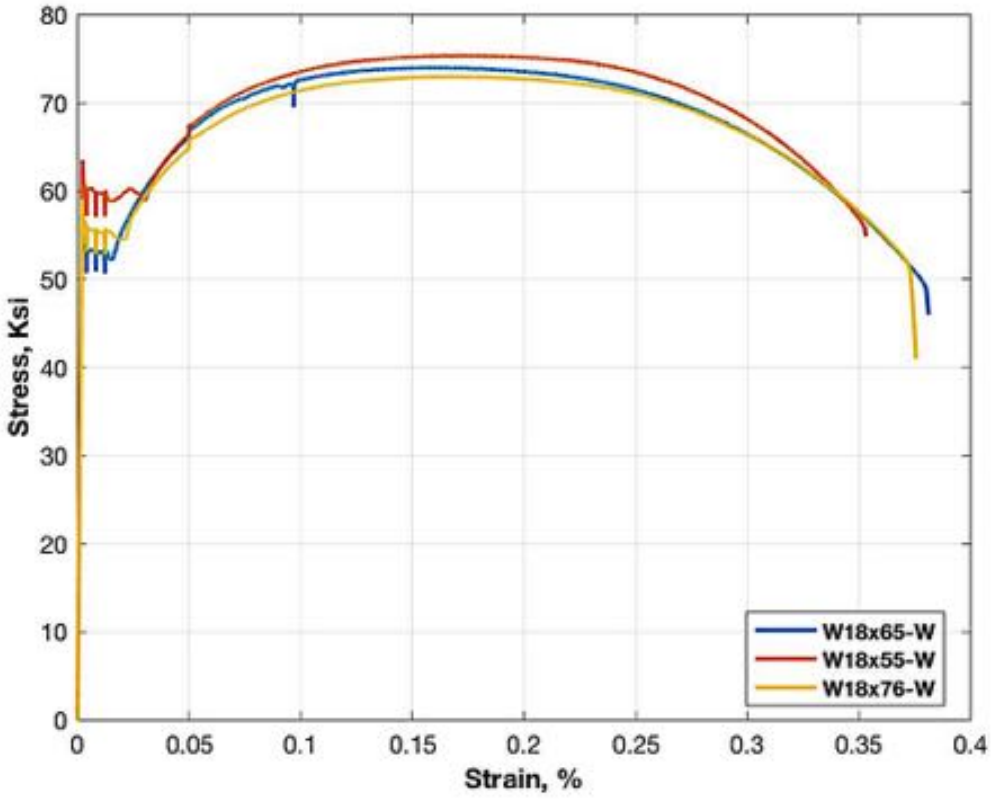

Figure 3.4: Engineering stress-strain response for beam webs

Table 3.2 Material Properties of Beam Specimens

Specimen Number	Beam Size	Web Yield Strength (ksi)	Web Ultimate Strength (ksi)	Flange Yield Strength (ksi)	Flange Ultimate Strength (ksi)
1	W18x65	53	74	51	74
2	W18x55	58	75	55	73
3	W18x76	56	73	54	72

3.3 Overview of Finite Element Models for Post-Tensioned Beam-to-Column Connections

This section provides an overview of the numerical models, including the different element types, solid and shell, considered, as well as the different solution algorithms, implicit and explicit, considered in this study. More specific details of the shell and solid element models will be described in Sections 3.4 and 3.5, respectively. Additionally, this section describes aspects of the models that are common to all the considered element and solution algorithm types, such as assigned material properties.

3.3.1 Element Types

Finite element models of post-tensioned beam-to-column connections are developed using two primary element types: one using shell elements for the main structural members, and another using solid elements. The shell-based finite element models, shown schematically in Figure 3.5 (a), consist of shell elements for the beams and column, slot constraints to simulate the slotted shear connection, and connector elements to characterize the gap opening and closing behavior within the connection. Solid-based finite element models, as shown in Figure 3.5 (b), are conducted using solid elements for each member, including the PT bars, and a contact interaction model is used to simulate contact behavior, where a friction tangential behavior is also added in the contact interaction to provide shear resistance within the connection. In terms of analysis time, on average, the FE analysis time for one solid model is 12 hours long, while for a shell element model, the running time is 6 hours long using the Ferguson Structural Engineering Laboratory's high-speed computing platform where each node contains a Dell PowerEdge R820 server, 256 GV Ram, with 32 cores.

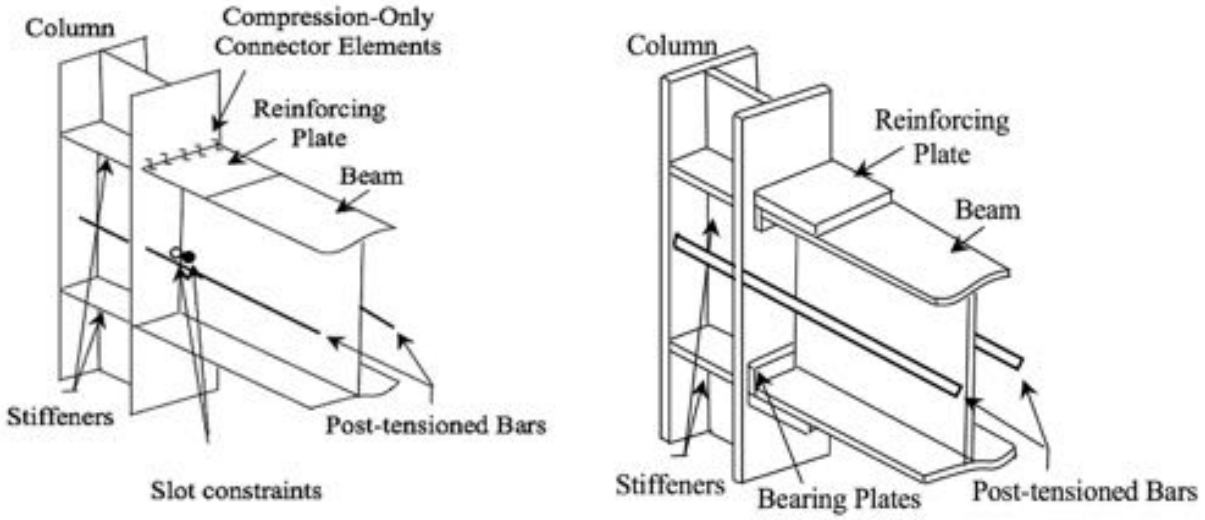

Figure 3.5: Schematic of computational finite element post-tensioned connection model with (a) shell elements [adapted from Clayton et al. (2015)] and (b) solid elements

3.3.2 Solution Algorithms

ABAQUS/Standard is used for the majority of this study, as its unconditionally stable implicit solution algorithms produce reliable results for a broad range of nonlinear behaviors; however, for some cases where severe local buckling results in highly nonlinear response, the implicit static algorithms used in ABAQUS/Standard are not able to successfully find a converged state. While these convergence challenges were not observed in the validation comparisons with the experimental specimens, it was observed during the later parametric study (discussed in Chapter 4), particularly for very slender beam sections with more severe local buckling. For cases where the ABAQUS/Standard static analysis is unable to complete an analysis due to convergence issues, an ABAQUS/Explicit quasi-static dynamic analysis is used due to its ability to capture highly discontinuous post-buckling behaviors that are difficult to capture with implicit methods in

ABAQUS/Standard. Since equilibrium is not strictly enforced in explicit methods, small analysis time steps must be used to capture changes in stiffness throughout the entire response, which requires significant computation time—much more than required by static implicit methods. For instance, the stable time increment of explicit analysis performed for Specimen 3 is 1.37e-05 sec, out of a total loading duration of 236 sec, and the analysis runtime was 27 hours, while the implicit static analysis runtime for the same simulation was around 6 hours. Hence, ABAQUS/Explicit dynamic analyses are only used in cases where ABAQUS/Standard static analyses are unable to produce the desired results. The comparisons in this chapter demonstrate that using the recommended modeling approaches, ABAQUS/Explicit is able to produce results nearly identical to ABAQUS/Standard results from converged models.

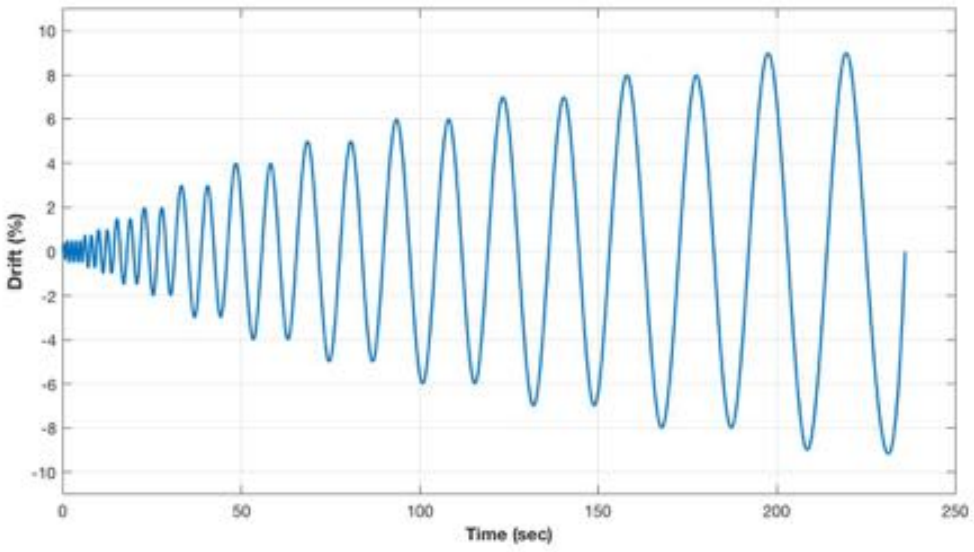

Figure 3.6: Displacement loading history of experimental work

The experimental displacement history shown in Figure 3.2 is applied to the numerical models in ABAQUS/Standard at the same location as the actuator that is used

to apply load during the experiments. To simulate quasi-static loading in the dynamic ABAQUS/Explicit analyses, the time scale of the displacement history was defined long enough to guarantee inertial effects were negligible in the model. In addition, the *Smooth Step* loading amplitude is used to define the displacement history given in Section 3.2 as shown in Figure 3.6.

In detail, the central difference method used in ABAQUS/Explicit is a conditionally stable algorithm (ABAQUS 6.14 documentation, 2014); therefore, the maximum analysis time increment should be less than the critical time step, Δt_{cr}, to ensure numerical stability. The critical time step can be defined as the time that it would take a dilatational wave to propagate through an element:

$$\Delta t_{cr} = L_{min} \sqrt{\frac{\rho}{E}} \qquad \text{(Eq. 3.1)}$$

where, E is the modulus of elasticity of the material, ρ is the density of the material, and L_{min} is the minimum characteristic element length (shortest length of an element mesh). As shown in the Equation 3.1, element mesh size, elastic stiffness, and density are key parameters that can affect the critical time increment, consequently affecting the computational runtimes. Defining very large material stiffness or very small elements can result in very small-time steps and long computational run times. Thus, artificially high stiffnesses to simulate nearly rigid behaviors and excessively fine meshes should be avoided when possible. The critical time step can also be increased through mass scaling, which amplifies the density term. Therefore, to reduce the computational runtime, the number of steps required in a given load history must be reduced, which, according to Equation 3.1, can be achieved by increasing the mass (or density ρ) of the material by a

factor of f^2, which results in an increase in the critical time step by a factor f. During ABAQUS/Explicit analyses, a mass scale of twenty-five is used for all of the members (e.g., beam, reinforcing plate, PT elements) of the model. When using mass scaling, care must be taken to ensure that inertial dynamic effects remain negligible for simulation of quasi-static loading.

3.3.3 Boundary Conditions and Material Models

Boundary conditions and applied displacements for the FE models of the test specimens are shown in Figure 3.7. These boundary conditions apply to both solid and shell element models to simulate experimental conditions. The column has pinned supports at the tie-down locations, represented as displacement restraints in the global x, y, and z direction (u_x, u_y and u_z, respectively). The beams are laterally supported at the same locations as the experiments, where the out-of-plane displacements and twist of the beam cross-section are restrained at that location, shown as u_x=uR_y=0, where uR_y is the rotation about the global y axis. The cyclic lateral displacement history is applied through a reference point on the beam section at the same location as the actuator, using the same load protocol used in the tests. The reference point is tied to the beam cross-section at this location by defining a rigid body constraint to prevent stress concentrations at the loading point.

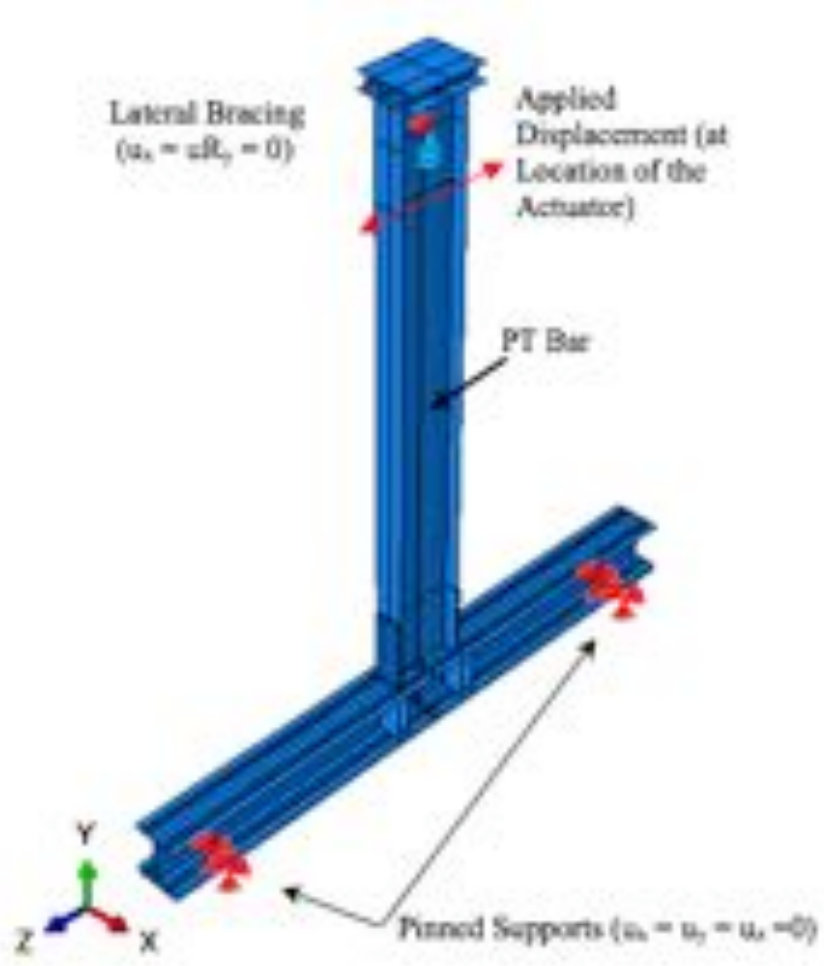

Figure 3.7: Typical ABAQUS model boundary conditions and restraints

In addition to the boundary conditions, material models are also the same for each numerical simulation. As previously outlined, the reinforcing plates, stiffeners, bearing plates, and anchorage assembly were made of steel with a nominal yield strength of 50 ksi, while the PT bars were made of high strength steel with an ultimate strength of 150 ksi in compliance with ASTM A722 specifications. Columns and beams were made of A992 steel material with a nominal yield strength of 50 ksi. The columns, reinforcing plates, stiffeners, bearing plates, and the anchorage assembly, all termed structural steel (SS) in

Figure 3.8 (b), as well as the PT elements, are defined using nominal yield strengths, as shown in Figure 3.8 (b), and remained essentially elastic during the analyses.

The beams, on the other hand, are expected to experience yielding due to the local buckling behavior under investigation, thus material models are calibrated to more accurately simulate actual, rather than nominal, material properties of the beams in the test specimens. ABAQUS requires material input to be in terms of true stress and true strain; therefore, engineering stress and strain results from the coupon tests are used to calculate true stress and strain values for the beam material as given in Equations 3.2 and 3.3, respectively.

$$\sigma = \sigma_{eng}\left(1 + \epsilon_{eng}\right) \quad \text{(Eq. 3.2)}$$

$$\epsilon = ln\left(1 + \epsilon_{eng}\right) \quad \text{(Eq. 3.3)}$$

where, σ_{eng} and ϵ_{eng} are engineering stress and strain, respectively, while σ is the Cauchy (true) stress and ϵ is the logarithmic (true) strain. Subsequently, logarithmic plastic strains, ϵ_{pl},will be:

$$\epsilon_{pl} = \epsilon - \sigma/E \quad \text{(Eq. 3.4)}$$

The beam material is simulated using a multi-linear backbone with linear isotropic hardening as shown in Figure 3.8 (a), where key points of the backbone true stress-true plastic strain behavior defined in the ABAQUS model for each beam uniquely. As an example, for W18x76 beam flange, material model is shown in Figure 3.9 and defined as and: σ_y=54 ksi, σ_t=72 ksi, σ_u=100 ksi, and $\epsilon_{pl,y}$= 0, $\epsilon_{pl,t}$=0.045, $\epsilon_{pl,u}$=0.241. Other material properties are provided in Appendix A. It has been observed that both in the strain

gage measurements in the experimental tests and all numerical analyses conducted as part of this study, plastic strains remain under the defined ultimate strain value (even under 0.16 plastic strain).

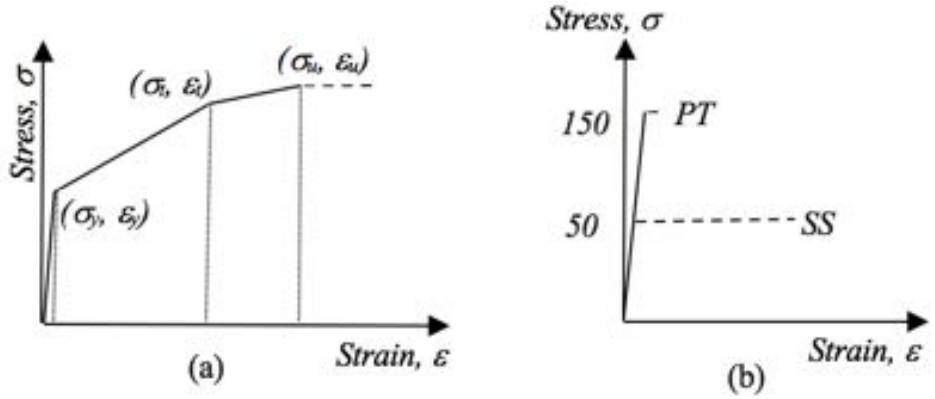

Figure 3.8: Constitutive laws for: (a) beams; (b) structural steel (SS) (e.g., reinforcing plates, column, stiffeners, anchorage assembly, and top plates) and post-tensioned bars (PT)

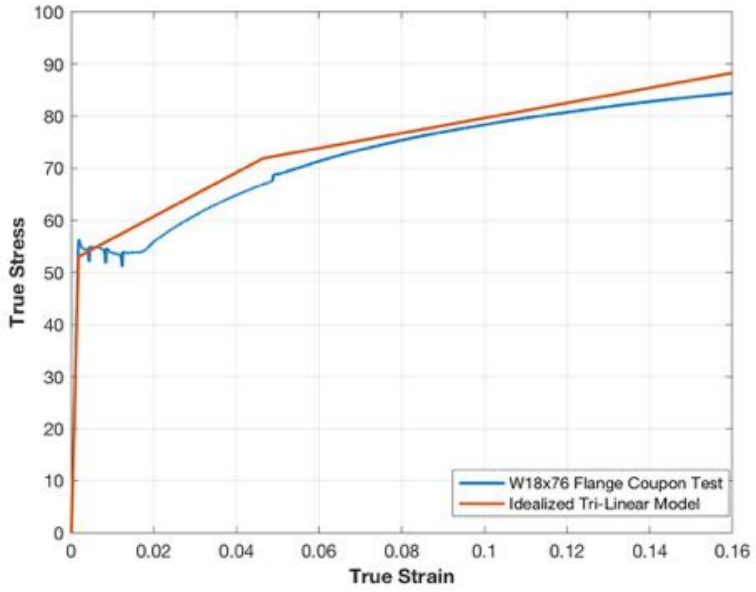

Figure 3.9: Idealized Tri-Linear Material Model for W18x76 Flange Coupon Test

3.4 SHELL ELEMENT MODELS

3.4.1 Model Description

In the shell element models, the S4R element is used to model the main members of the PT beam to-column connections. The S4R element is a four-node, quadrilateral, shell element with reduced integration, and these shell elements have been shown to be computationally efficient and capable of capturing local buckling within a cross section (Elkady and Lignos, 2015). Modeling of beam, column, reinforcing plates, stiffeners, and the anchorage assembly members are done using S4R shell elements with hourglass control in ABAQUS. Bearing plates are not explicitly modeled here.

Post-tensioned bars are modeled using truss elements that are tied to the column flange at the bottom and to the anchor assembly at the top. The initial post-tension force is defined using bolt loads in ABAQUS. Initial post-tension load can also be applied using a temperature load (as a predefined field on ABAQUS) with a defined coefficient of thermal expansion.

The gap opening and closing behavior of the post-tensioned connections are modeled using compression-only springs connecting the nodes at the end of the reinforcing plates and the nodes on the column flange face, where compression-only springs are defined using axial connectors in ABAQUS. Forces are transferred between the beam and column through the defined springs. The axial compressive stiffness, k_{CS} (shown in Figure 3.10), of the springs are defined as recommended by Kim (2007) and Kamperidis (2016), which is equal to 15-20 times the beam axial stiffness, as this value matched well with experimental data without significantly affecting computational time. In addition, a slot constraint is defined between the beam web and column flange to represent the behavior of the bolted shear tab with slotted holes used in the connection.

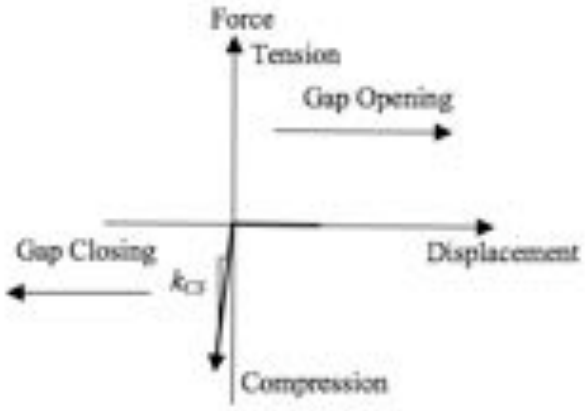

Figure 3.10: Force-displacement relationship for compression-only springs modeled in shell finite element models

3.4.2 Analysis and Application of Imperfections

First, preloads are generated in the post-tensioned bars using the bolt-load command in ABAQUS. Following this, to help trigger local instabilities, initial geometric imperfections representing local beam buckling modes are included by revising the nodes of post-tensioned beam models. The imperfections are applied following the recommendations of Elkady and Lignos (2017), Kim and Lee (2002), and Seif and Schafer (2017). This initial imperfection is achieved by scaling the typical buckling mode given in Figure 3.11 as determined from an eigen analysis of the model. Figure 3.11 shows the upper bounds of local imperfections that can be introduced as per AISC 360 (AISC 2016b) and ASTM (2015) which are *d/150* and $b_f/150$ for the web and flange, respectively, where *d* is the beam depth and b_f is the flange width. These upper bound imperfection limits were used to set the scale factor for the local buckling mode. Finally, cyclic displacements defined in Figure 3.2 are applied to the system via a nonlinear static analysis in ABAQUS/Standard considering geometric and material nonlinearity.

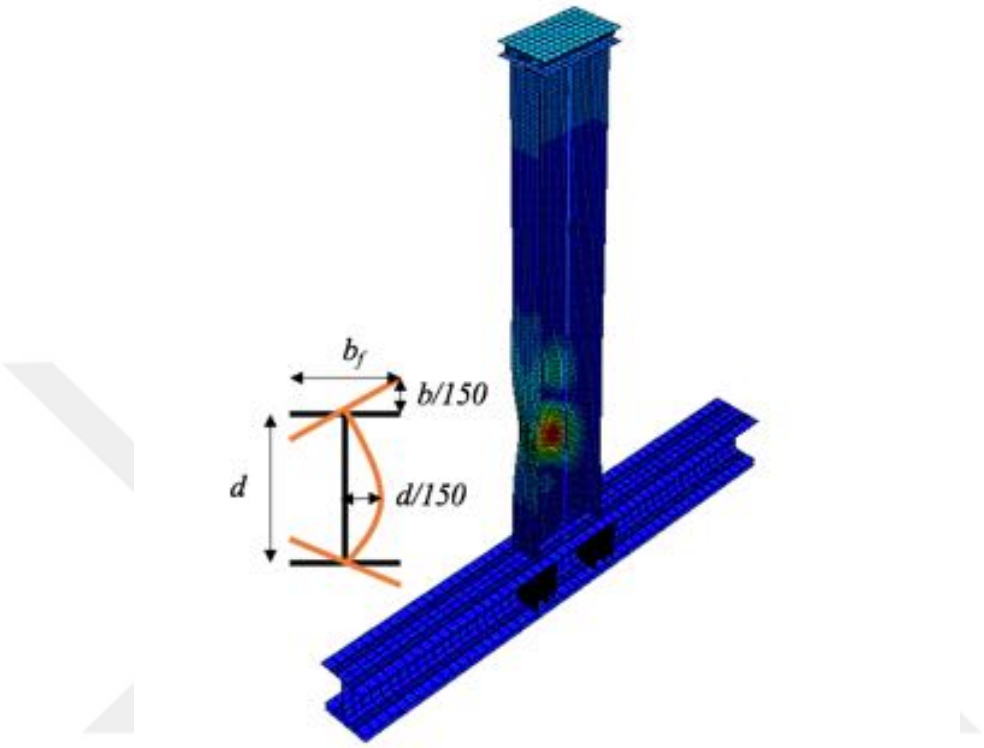

Figure 3.11: Typical buckling mode considered in the analysis for local geometric imperfections

3.4.3 Meshing

Mesh refinement of the beam is performed until no substantial change in the response is achieved. Meshing has been performed with elements ranging from 6.5 inch to 0.9-inch square quadratic four-node S4R shell elements. Figures 3.12 and 3.13 show results from a mesh sensitivity study that is performed for Specimen 3, which showed the most extensive local buckling of all the test specimens. In the given figures, "maximum moment" is defined as the largest moment capacity observed from the positive (i.e. south) loading direction, and "minimum moment" is defined as the peak moment from the positive 9% drift loading cycle after significant strength degradation has occurred. These values are

normalized with respect to the value measured during the experiments, where a value of 1 would indicate a FE result that perfectly matches the corresponding value observed in the test. According to the comparison results shown in Figures 3.12 and 3.13, mesh sensitivity evaluations for the normalized “maximum moment” and “minimum moment” reaches to the unit value as the element number is increased in the beam. A mesh size of 1.1-inch square, which corresponds to 3924 elements, is chosen as the selected mesh for the analyses presented in this study, as the observed moments do not change significantly with more refined meshes beyond this point. Additionally, the “verify mesh section” command in ABAQUS is used to check the quality of the mesh with respect to element aspect ratio (ABAQUS 6.14 documentation, 2014).

To model the connections between the welded components (e.g., between the beam and the reinforcing plates, etc.), tie constraints are employed. According to ABAQUS, to avoid convergence problems, mesh density of the constrained surfaces must be finer than the retained surfaces. A detailed view of the selected mesh is shown near the connection in Figure 3.14. A mesh refinement study is not performed for the column as the column remains essentially elastic during the entire loading protocol.

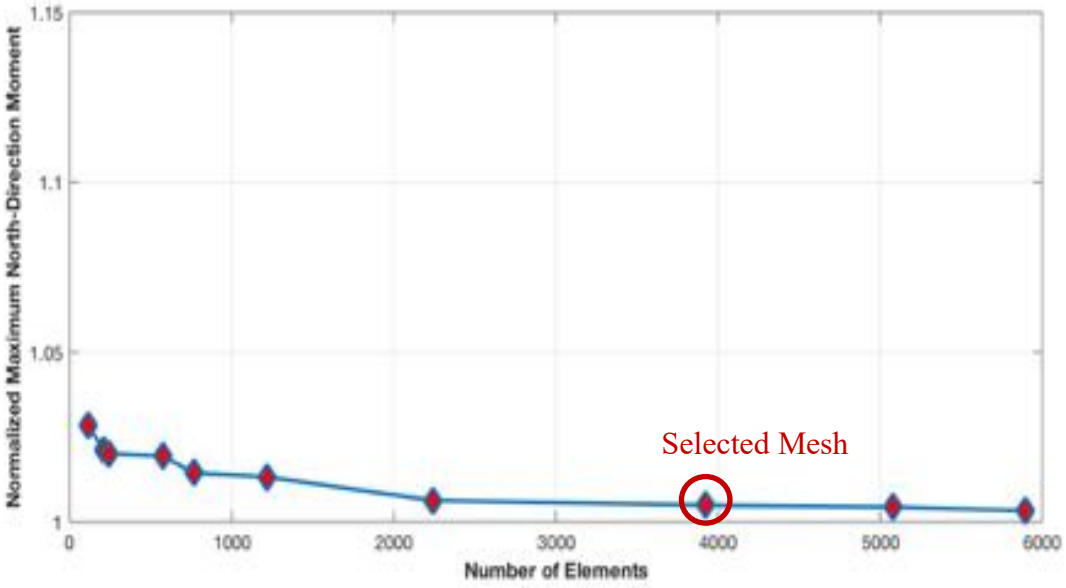

Figure 3.12: Mesh sensitivity study of Specimen 3 showing maximum moment obtained in simulation normalized with experimental data

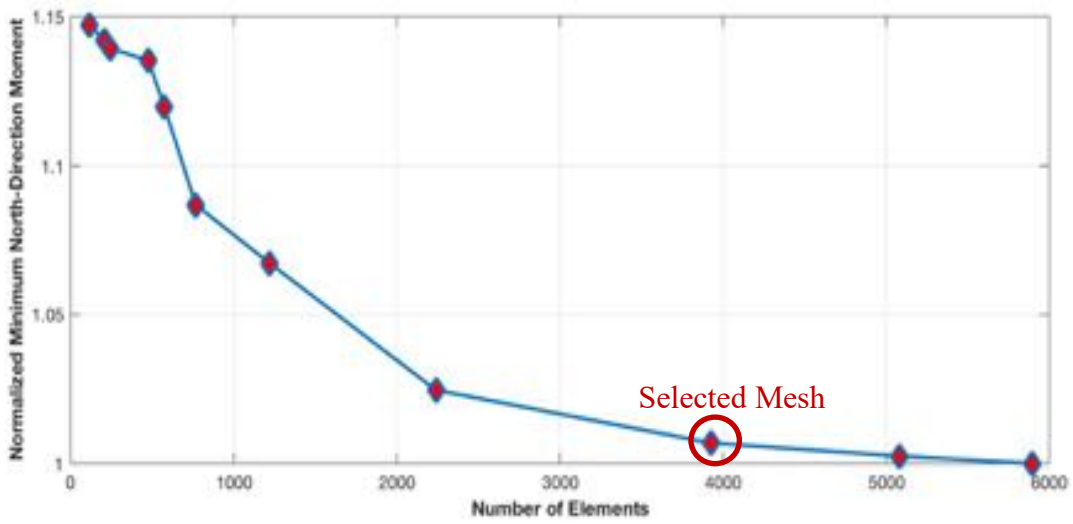

Figure 3.13: Mesh sensitivity study of Specimen 3 showing minimum moment obtained in simulation normalized with experimental data

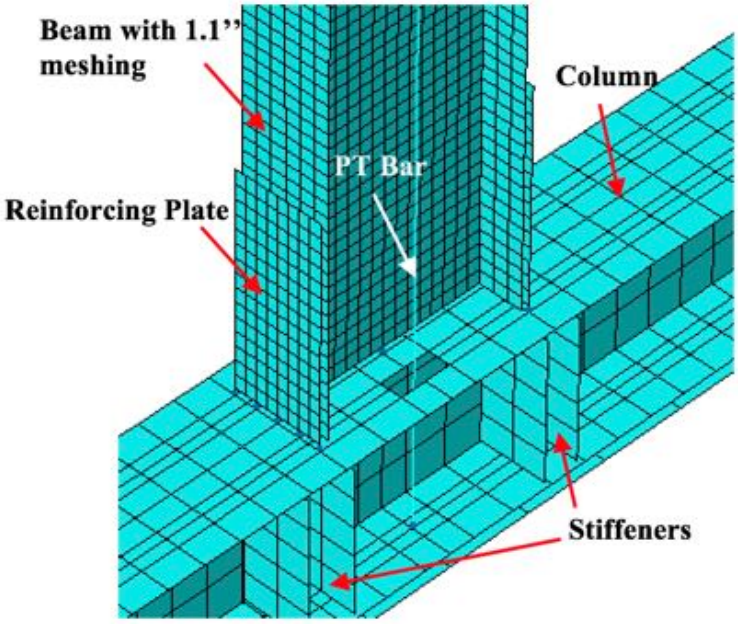

Figure 3.14: View of connection region showing selected mesh

3.5 SOLID ELEMENT MODELS

3.5.1 Model Description

Solid element models are also created in the ABAQUS FE software using *C3D8R*, eight node brick elements with reduced integration. These three-dimensional solid (continuum) elements are employed to model the beam, column, PT elements, PT anchorage assembly, reinforcing plates, and stiffeners. To model interactions between welded components (e.g., between the beam and the reinforcing plates and bearing plates, etc.), tie constraints are employed. PT bars are tied to the column flange at the bottom and tied to the anchorage assembly at the top. To define contact interaction between bearing plates and the column face, surface-to-surface contact interaction is used. Contact behavior in ABAQUS is simulated through tangential and normal behavior between the contact surfaces. The

normal behavior is defined by hard contact, while the tangential behavior is simulated using a penalty method with a friction coefficient of 0.33 as suggested by Moradi et al (2015).

3.5.2 Analysis

ABAQUS analyses for the solid elements are performed in two steps. First, preloads are generated in the PT bars, then cyclic displacements are applied to the system via a nonlinear static analysis considering geometric and material nonlinearity in ABAQUS/Standard. The displacement history given in Figure 3.2 is applied at the same location as the actuator in the test. For solid models, initial imperfections are not assigned.

3.5.3 Meshing

ABAQUS employs a retained/constrained formulation for tie constraints and for contact interactions. Meshing for these surfaces should be performed carefully to prevent convergence problems, as the mesh on the constrained surface should be denser than its retained surface. Therefore, mesh sensitivity analysis is not performed for the solid element models; rather the suggested method by Moradi (2015) is used, where a finer mesh, with a mesh size equal to 1.2 inch, is assigned in the end region of the beam closest to the beam-column contact surface to capture the buckling behavior and stress concentrations within the connection as shown in Figure 3.15.

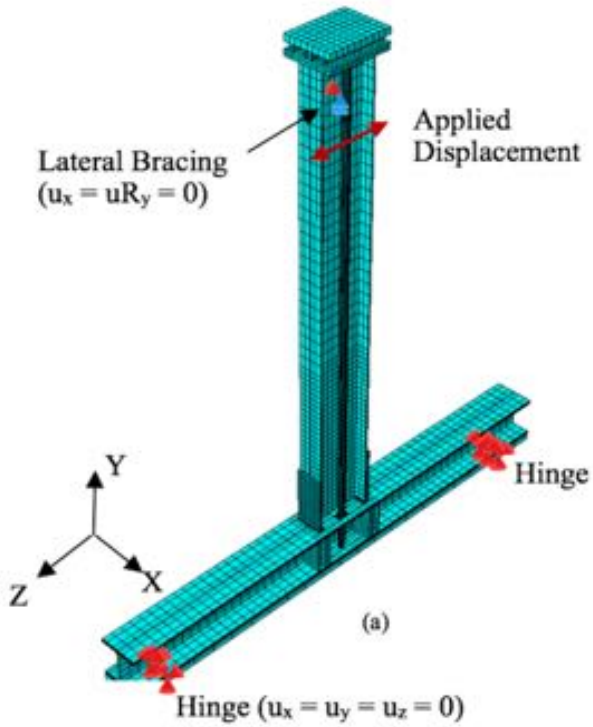

Figure 3.15: Typical ABAQUS model of solid elements showing meshing

3.6 Analysis Results and Model Validation

The results from the three experimental tests from Hulsey (2015) are compared with the FE results, including comparisons of the shell and solid element models using the implicit solution algorithm, as well as a comparison of implicit and explicit solution algorithms for the shell element models. The comparisons show the reliability of the numerical results to capture rocking and strength degrading behaviors of the PT connection, including local buckling.

A detailed comparison between the results of the experimental tests and the FE models is provided for the shell element models, including comparisons of the global moment-drift behavior and PT force-drift response of the PT connections; whereas only

the comparison of the global moment-drift behavior is included for the solid element models, and the applicability of the solid element models are discussed. Comparison of the results and a detailed explanation for selecting the shell element models for the following parametric studies are provided.

3.6.1 Numerical Results for Test Specimen 1

During the testing of Specimen 1, consisting of a W18x65 beam, slight local buckling was observed. The moment-drift response of the FE models is shown with the experimental results in Figures 3.16 and Figure 3.19 for implicit (ABAQUS/Standard) and explicit (ABAQUS/Explicit) analyses, respectively. For the implicit analysis results in Figure 3.16, both solid and shell element models are shown. For the explicit analysis results in Figure 3.18, only the shell element model is shown. The south direction is represented by positive drifts in the simulation and experimental results. According to the figure, connection decompression, as represented be the green star in Figure 3.16, occurred between 0.55% and 0.7% drift for both numerical models and experimental specimen. In terms of capturing the connection hysteresis, the solid element model showed better performance compared to the shell element model. This observation could be due to explicit modeling of friction using the contact interaction between solid elements at the beam-column interface, while the slot constraints and the gap opening springs in the shell element model do not simulate energy dissipation due to friction. The softening of the connection started to occur after the 3% drift cycles, as a few diagonal lines started to appear in the mill scale on the face of the web. The softening of the connection and the lines in the mill scales increased in number and length throughout the 4% and 5% drift cycles. While the flanges were never visibly buckled, the center of the web had buckled slightly, and this buckling is also observed at the end of FE analysis.

In addition to the moment-drift response, the total PT force vs. drift response is also shown for the shell element models in Figures 3.17 and 3.19 for implicit and explicit solution algorithms, respectively. As can be seen, the initial PT force and the overall behavior of the post-tensioned bars are well captured in the shell element models. The initial PT force during the experiments was 187 and 185 kips for the east and west bars, respectively, for a total of 372 kips. According to experimental results, and as can be also observed in Figure 3.16, the maximum PT force and moment occurred in the first 5% drift cycle for both the South (S) and North (N) peaks, and the values are given in Table 3.3. At the end of the test, the total PT force was 272.5 kips, corresponding to a PT loss of 100 kips, and the shell element implicit FE results showed a total PT force of 274 kips, corresponding to PT loss of 98 kips. According to PT loss results, it can be concluded that FE models can predict the loss in PT force caused by plastic shortening of the beam.

Table 3.3 Comparison between the Experimental and Shell Element FE results

Drift level of interest	**Experimental Results**		**FE Results (Response Ratio)** [a]			
	Moment (kip-ft)	**PT Force (kips)**	**Moment (kip-ft) (Implicit)**	**Moment (kip-ft) (Explicit)**	**PT Force (kips) (Implicit)**	**PT Force (kips) (Explicit)**
1st 5% -South	375	514	400 (1.06)	401 (1.07)	526 (1.02)	534 (1.03)
1st 5% -North	-408	502	-398 (0.97)	-395 (0.97)	529 (1.05)	533 (1.06)

[a] Response Ratio: ratio between FE results and corresponding value from experiment.

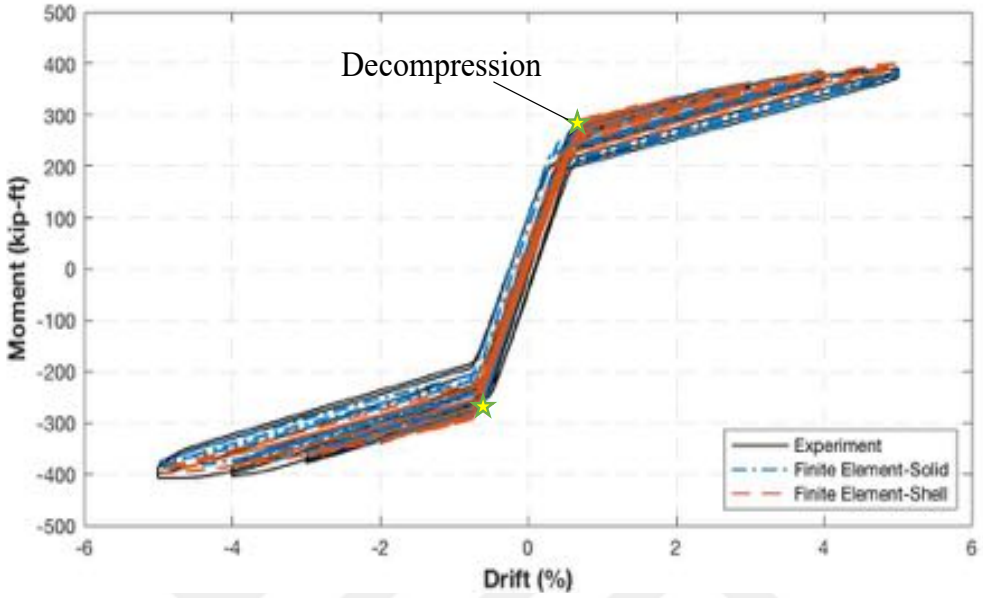

Figure 3.16: Moment-drift response validation results for test Specimen 1 using implicit analysis algorithm

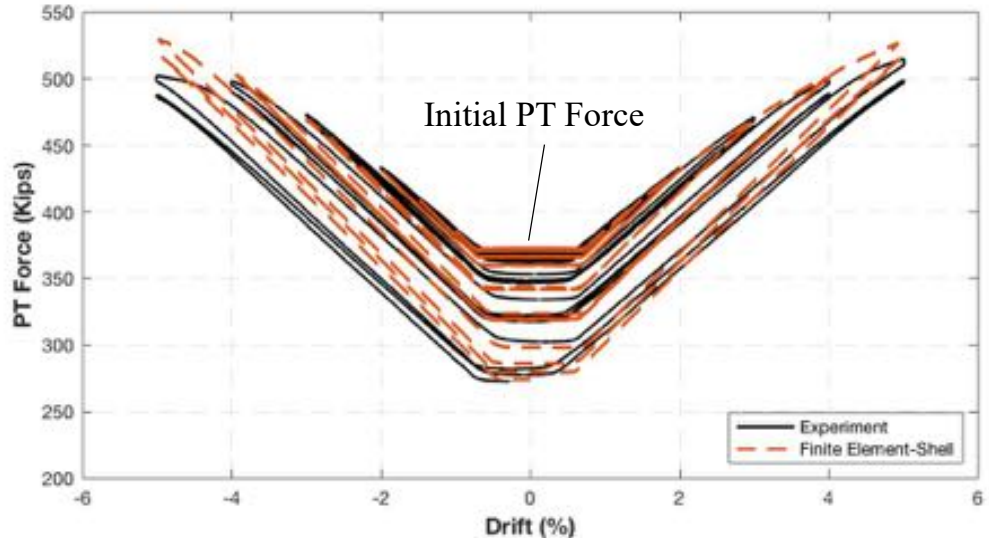

Figure 3.17: PT force-drift validation results for test Specimen 1 using implicit analysis algorithm

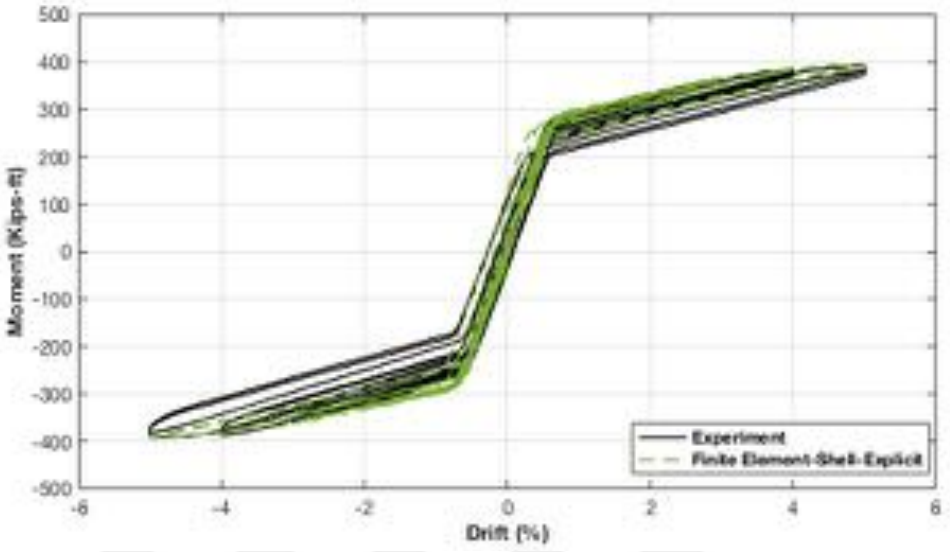

Figure 3.18: Moment-drift response validation results for test Specimen 1 using explicit analysis algorithm

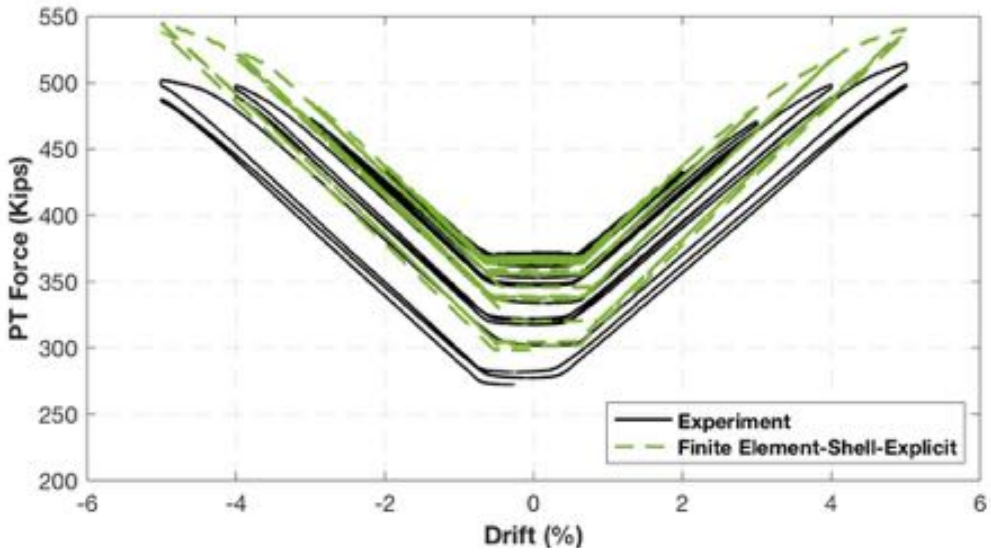

Figure 3.19: PT force-drift validation results for test Specimen 1 using explicit analysis algorithm

3.6.2 Numerical Results for Test Specimen 2

For the second experiment, two additional cycles at 5% drift are applied to further investigate the buckling behavior of the connection. Figures 3.20 to 3.23 show the comparison of experimental and FE simulation results for Specimen 2. Similar to Specimen 1, computational results for both solid and shell element models can successfully capture the gap opening and self-centering behavior of the tested PT beam-to-column connection. Furthermore, the strength degradation behavior due to beam local buckling is also well demonstrated by the ABAQUS model as shown in the given figures.

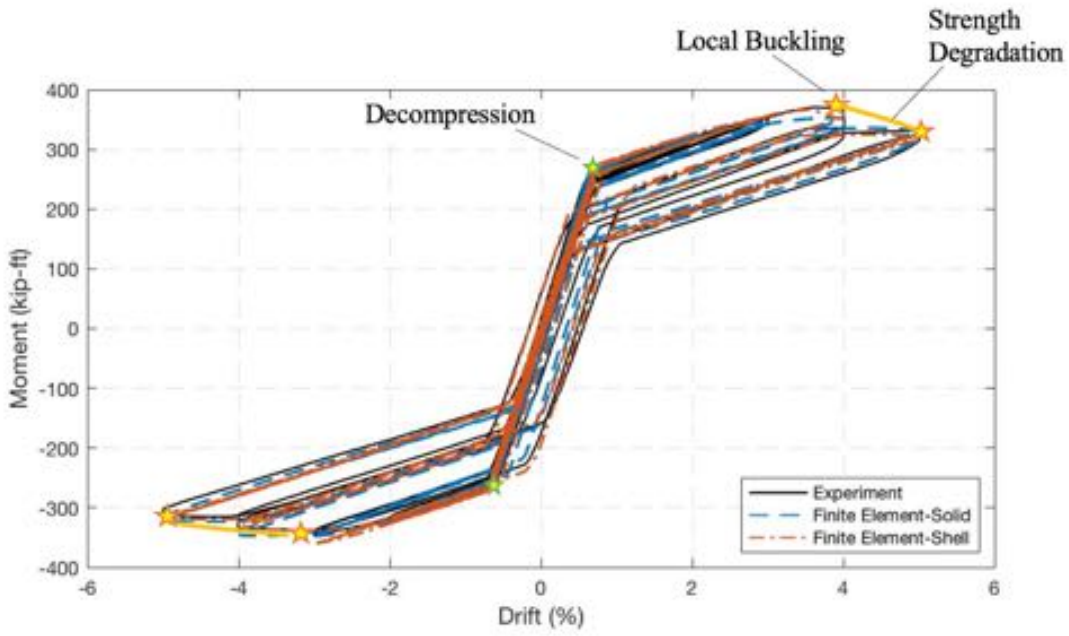

Figure 3.20: Moment-drift response validation results for test Specimen 2 using implicit analysis algorithm

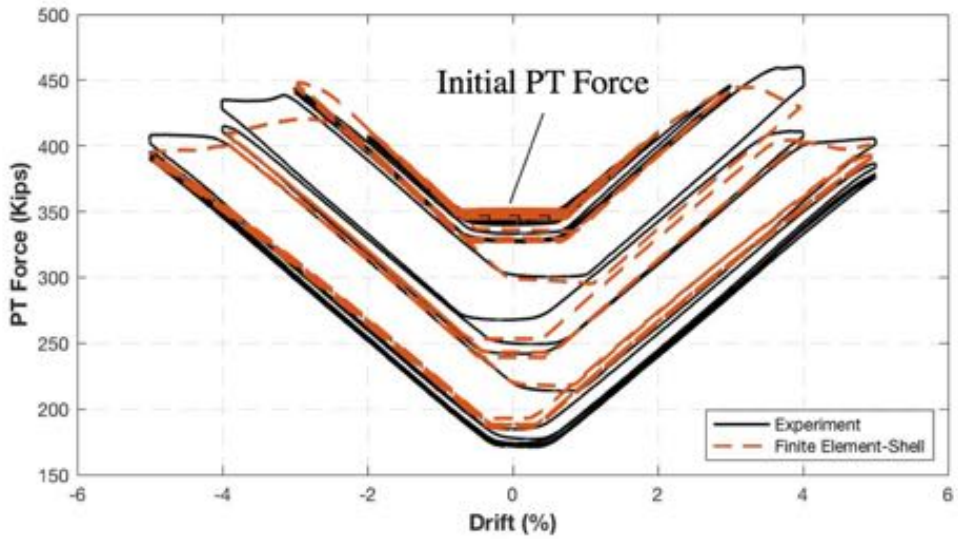

Figure 3.21: PT force-drift validation results for test Specimen 2 using implicit analysis algorithm

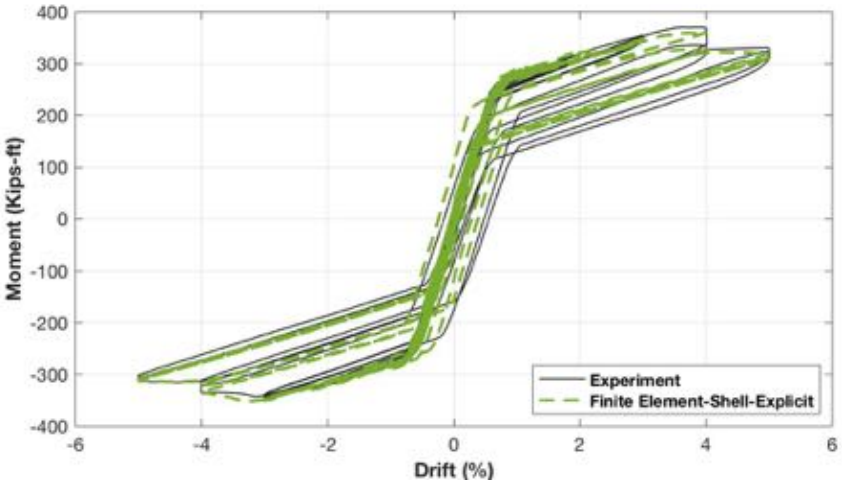

Figure 3.22: Moment-drift response validation results for test Specimen 2 using explicit analysis algorithm

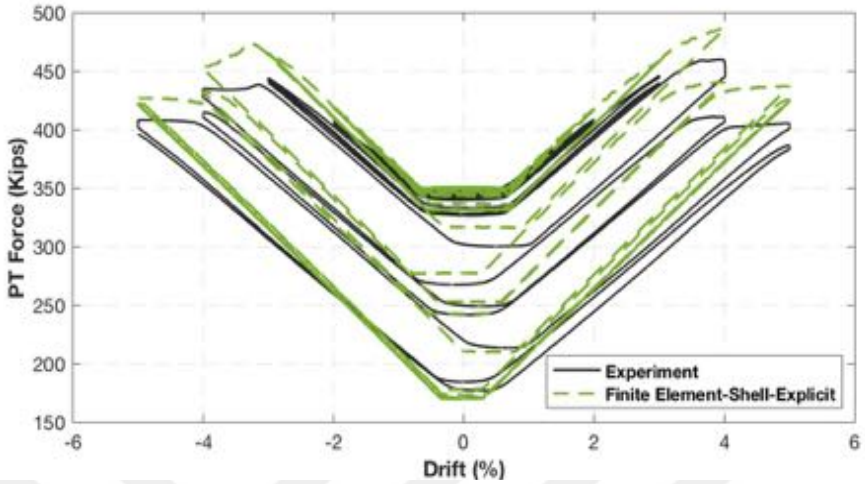

Figure 3.23: PT force-drift validation results for test Specimen 2 explicit analysis algorithm

According to Figures 3.20 and 3.22, the gap opening/decompression behavior, marked by the green star in Figure 3.20, occurred between 0.6% and 0.75% drifts during the experiments and gap opening behavior is well captured by the numerical models. The initial PT force in the east PT bar is 174.5 kips and 175.5 kips in the west PT bar, with a total force of 350 kips, as can be observed in Figures 3.21 and 3.23. According to these figures, the initial PT force from the FE models is equivalent to the experimental results. A summary of the comparison between experiment and FE results is shown in Table 3.4.

Table 3.4 Comparison between the Experimental and Shell Element FE results

Drift level of interest	**Experimental Results**		**FE Results (Response Ratio)** [a]			
	Moment (kip-ft)	**PT Force (kips)**	**Moment (kip-ft) (Implicit)**	**Moment (kip-ft) (Explicit)**	**PT Force (kips) (Implicit)**	**PT Force (kips) (Explicit)**
1st 4% -South	370	460	352.3 (0.95)	357 (0.96)	444 (0.97)	441 (0.96)
1st 3% -North	-345	445	-346 .7 (1.0)	347 (1.0)	448 (1.01)	448.5 (1.01)
4st 5% -South	331.3	402.6	331.3 (1.0)	328 (0.99)	415.9(1.03)	415.6 (1.03)
1st 4% -North	-334.3	432.6	-346.2 (1.04)	336 (1.0)	441.1(1.02)	443 (1.03)

[a] Response Ratio: ratio between FE results and corresponding value from experiment.

Following the experimental results, the maximum PT force and moment occurred at the N peak of the first 3% drift cycle, while for the S direction the maximum responses occurred at the peak of the first 4% drift cycle. The PT connection during the experiment starts to experience strength degradation behavior while going from 3% to 4% drift in the N direction (negative drift). Slight buckling, as noted a with yellow star in Figure 3.20 was observed in the northwest flange edge causing the aforementioned strength degradation. This behavior is also observed in the ABAQUS models. After completing the last 5% drift cycle, both flanges showed clear buckling with additional out-of-plane deformation of the web, which led to increased strength degradation (the behavior represented with a yellow line in Figure 3.20) in the connection. At the end of the tests, the total PT force was 171.2 kips, corresponding to a PT loss of 174 kips; while the shell element implicit analysis FE results showed a total PT force of 173.2 kips, corresponding to a PT loss of 177 kips. According to PT loss results, it can be concluded that FE models can predict the loss in PT force caused by plastic shortening of the beam.

Figure 3.24 and Figure 3.25 show a comparison between the simulated and experimental buckled shapes at the end of test, where the simulated results are shown for the shell element model with the implicit solution algorithm. According to all given results, it is clear that the shell and solid element models can capture strength degradation behavior due to beam local buckling, and most notably the shell element models accurately capture the PT force loss and resulting moment capacity reduction caused by local buckling and subsequent plastic shortening of the beam.

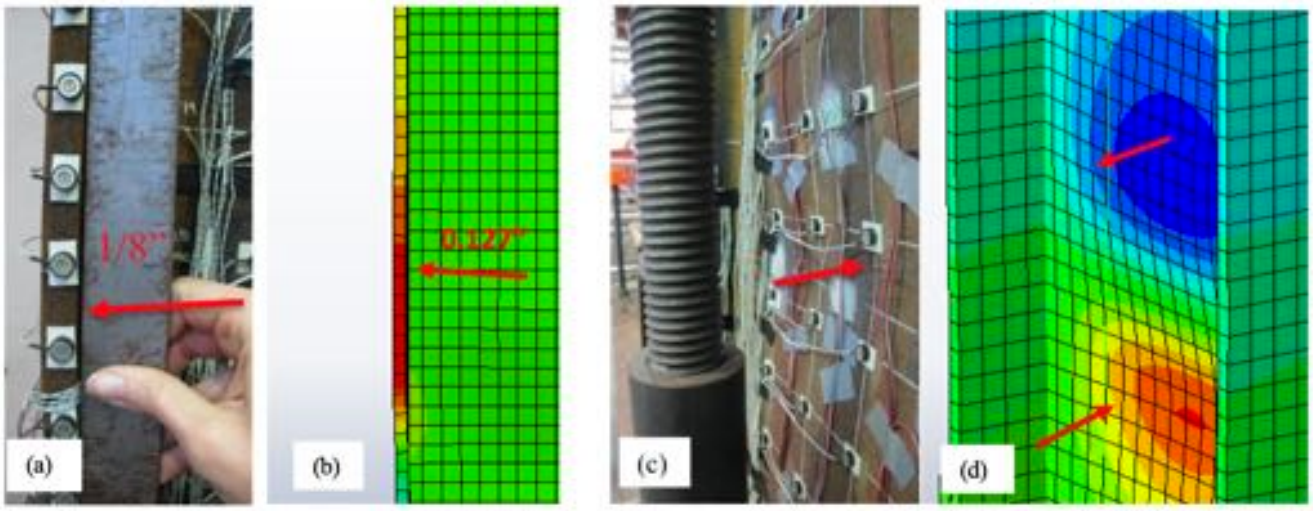

Figure 3.24: Comparison between (a, c) experimental and (b, d) simulated shell models flange and web buckled shapes at the end of the first N 4% drift cycle

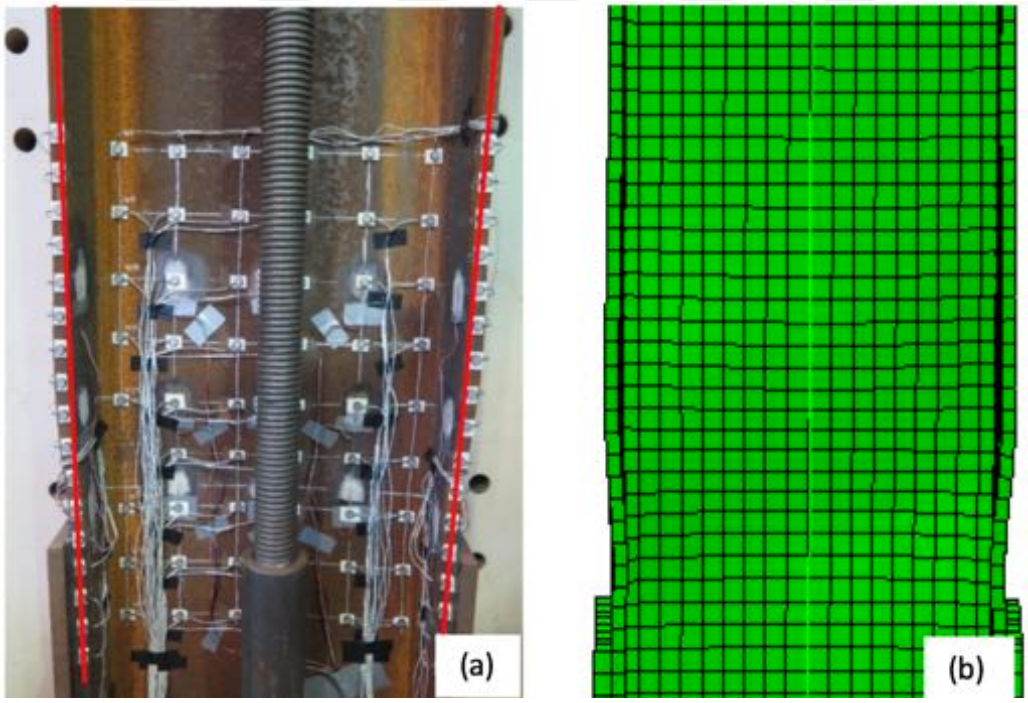

Figure 3.25: Comparison between (a) experimental and (b) simulated shell model flange buckled shapes at the end of 5% drift cycle

3.6.3 Numerical Results for Test Specimen 3

As previously discussed, the PT bars used in the Specimen 3 were larger in cross-sectional area compared to the previous test specimens, and the length of the beam is shorter as compared the previous ones to accommodate displacements up to 9% drift. Figures 3.26 and 3.28 shows the moment vs. drift comparison of experimental and FE results for both the shell and solid models using implicit and explicit solution algorithms, respectively, while Figures 3.27 and 3.29 show the PT force vs. drift response for the experiment and shell element models only using implicit and explicit solution algorithms, respectively. The results show the shell element model can effectively capture the gap opening and self-centering behavior of the tested PT beam-to-column connection. Furthermore, the strength degradation behavior due to beam local buckling is also well demonstrated by the FE models as shown in the given figures. According to Figure 3.26, the solid FE model failed to reach the 9% drift cycles, as the model failed to converge after the 8% drift cycle due to excessive deformation/distortion in the bearing plate, and it failed to capture the strength degradation behavior. As shown in Figure 3.30, similar behavior of the bearing plates is observed at the end of the experimental test of Specimen 3, where the beam is no longer fully bearing on the column face.

The initial PT force, which is equal to 337 kips, including 166 kips in the east PT bar and 171 kips in the west PT bar, is obtained in the shell element model as shown in Figures 3.27 and 3.29. Furthermore, decompression occurred between 0.3% and 0.5% drift both in both experimental and numerical models. A comparison of the results between experiments and FE simulations is summarized for Test Specimen 3 in Table 3.5.

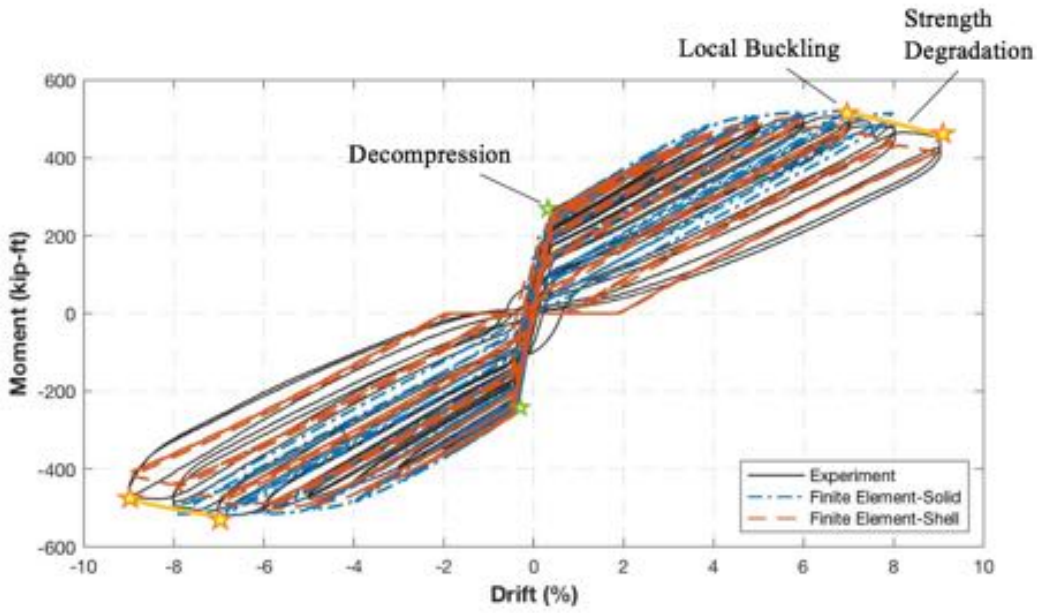

Figure 3.26: Moment-drift response validation result for test Specimen 3 implicit analysis algorithm

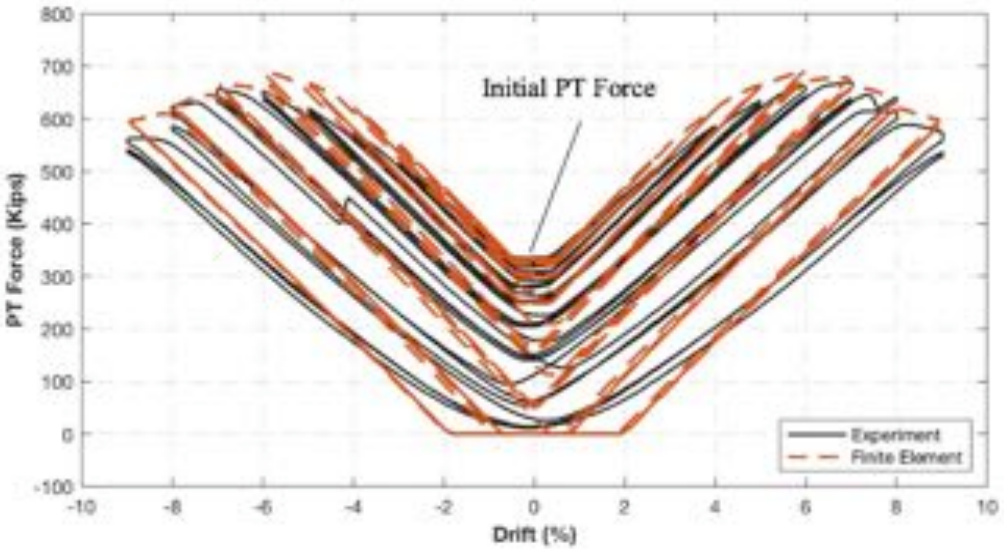

Figure 3.27: PT force-drift validation result for test Specimen 3 implicit analysis algorithm

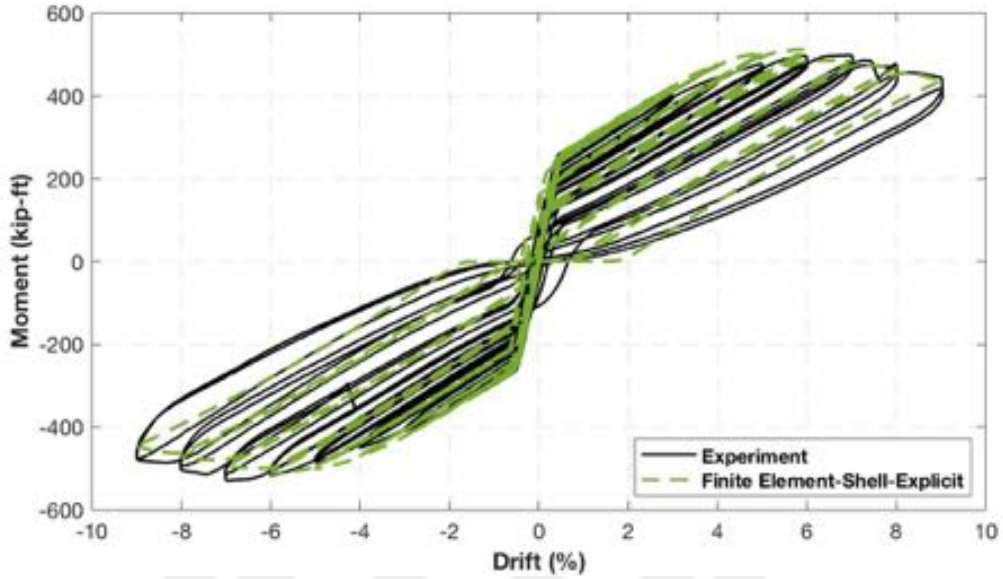

Figure 3.28: Moment-drift response validation result for test Specimen 3 explicit analysis algorithm

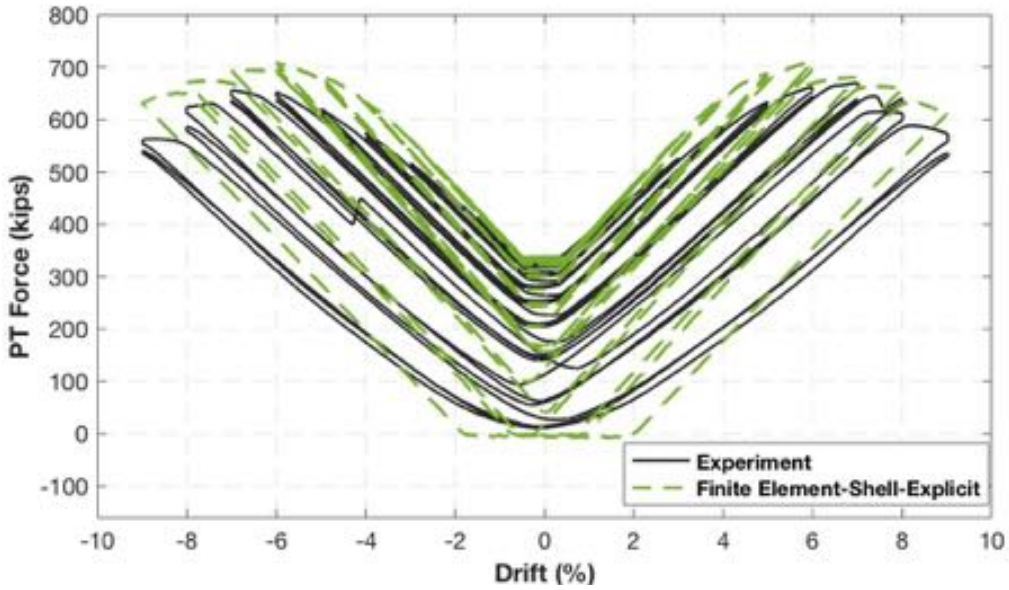

Figure 3.29: PT force-drift validation result for test Specimen 3 explicit analysis algorithm

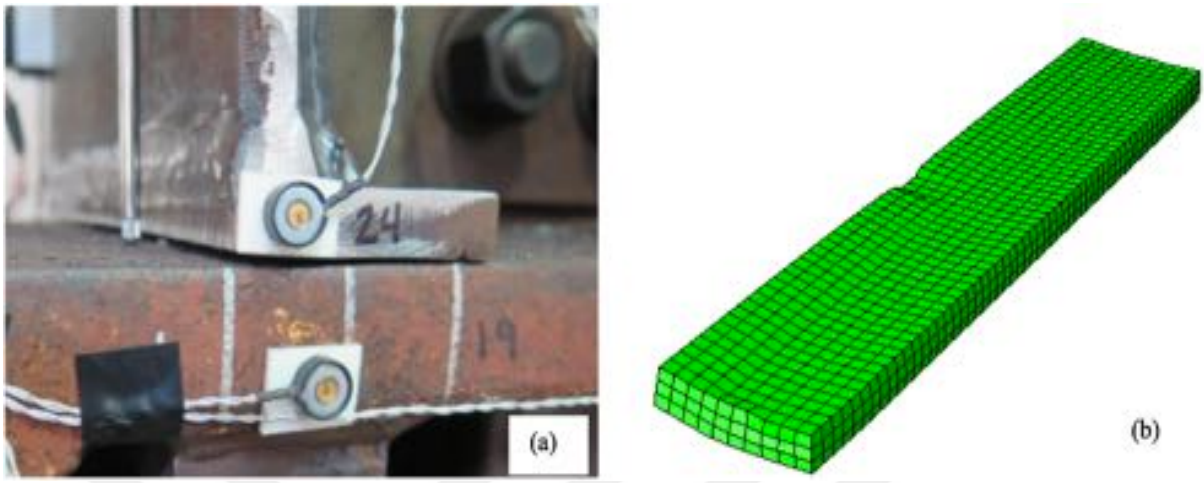

Figure 3.30: Bearing plate deformations at north bearing plate (a) at the end of the test, Hulsey (2015) and (b) at the end of the 8% drift cycles in the solid element FE model

Table 3.5 Comparison between the Experimental and Shell Element FE results

Drift level of interest	Experimental Results		FE Results (Response Ratio) [a]			
	Moment (kip-ft)	PT Force (kips)	Moment (kip-ft) (Implicit)	Moment (kip-ft) (Explicit)	PT Force (kips) (Implicit)	PT Force (kips) (Explicit)
1st 7% -South	498	670	478 (0.96)	478 (0.96)	677 (1.01)	677 (1.01)
1st 7% -North	-529	655	-488 (0.92)	-488 (0.92)	663 (1.01)	663 (1.01)
1st 9% -South	441	570	412 (0.93)	412 (0.93)	597 (1.05)	597 (1.05)
1st 9% -North	-477	561	-418 (0.88)	-418 (0.88)	595 (1.06)	595 (1.06)

[a] Response Ratio: ratio between FE results and corresponding value from experiment.

During the experiment, the connection response began to soften during the second cycle at 5% drift when very slight buckling was observed. Similarly, slight buckling also started to occur at the end of the 5% drift cycles in the FE simulations. During the first 6% drift cycle, increased buckling is observed in both flanges with softening of the PT force. With increasing drifts up to 7% drift, buckling in both flanges increased, and web buckling also became more pronounced, leading to further strength degradation within the connection. After reaching the 7% drift cycle, the connection experienced cyclic

degradation. The buckled shape at the end of the 7% drift cycles increased both in the flanges and web.

The simulated results for the shell model could capture the strength degrading behavior after the onset of local buckling as shown in Figures 3.26 to 3.29, while the solid model fails to capture the degradation behavior. Moreover, the buckled shapes are also compared for the FE shell implicit model and experimental specimen in Figures 3.31 and 3.32, showing the local instabilities are accurately captured by the shell element model. Figure 3.31 shows the bucked shape at the second 8% S peak. At this drift level, the computational model can accurately simulate local deformation of Specimen 3. Similar results are also obtained for the buckled shapes that were obtained at the end of the test, as illustrated in Figure 3.32. According to this figure, the buckling shape of the northwest flange is accurately captured by the simulation results; however, the buckled shape of the southwest flange is more similar to a full sine-wave shape in the experiment as compared to the approximate half-sine shape of all the other flanges in the experiment and simulation results. This result could be related to the initial shape and out-of-straightness of the flanges in the experiment, which were not fully characterized before testing.

As demonstrated in the PT force vs. drift figure (Figures 3.27 and 3.29), the PT force in the simulated results from the FE shell model reach zero at earlier drifts compared to the experimental results, which results in the loss of recentering capabilities in the moment vs. drift response (i.e., having residual drift at zero moment) in the model. As can be observed in the moment vs. drift response at larger drift cycles, the FE model reasonably captures the unloading stiffness at large drift demands; however, as the connection unloads to smaller drift levels, the experimental specimen response appears to soften (i.e., the stiffness reduces), whereas the FE shell model continues to unload with the same unloading stiffness until the PT force and moment go to zero. This softening of the experimental

unloading response after large drift demands is believed to be due to local deformations of the bearing surface in the experiments that are not simulated with the compression-only gap springs in the FE shell model. Hence, without the simulation of this softening response after unloading from very large drift demands, the FE shell model unloads to zero PT force earlier than is observed in the experiment.

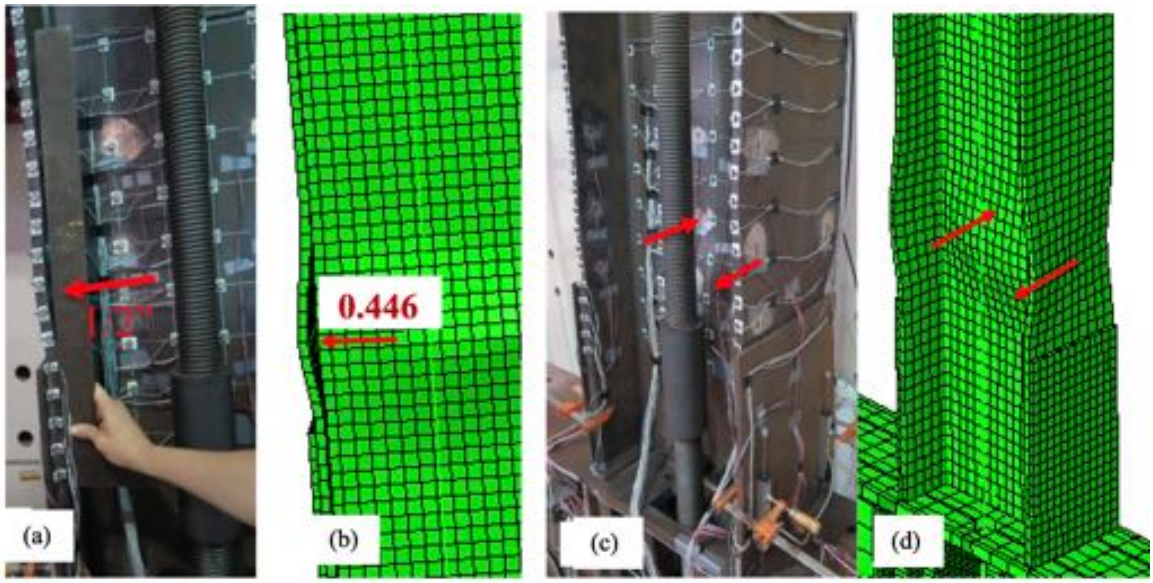

Figure 3.31: Comparison of simulated shell models and experimental buckled shapes (a, b) at peak of first 8% N cycle-northwest edge (c, d) at the end of second 8% S drift cycle

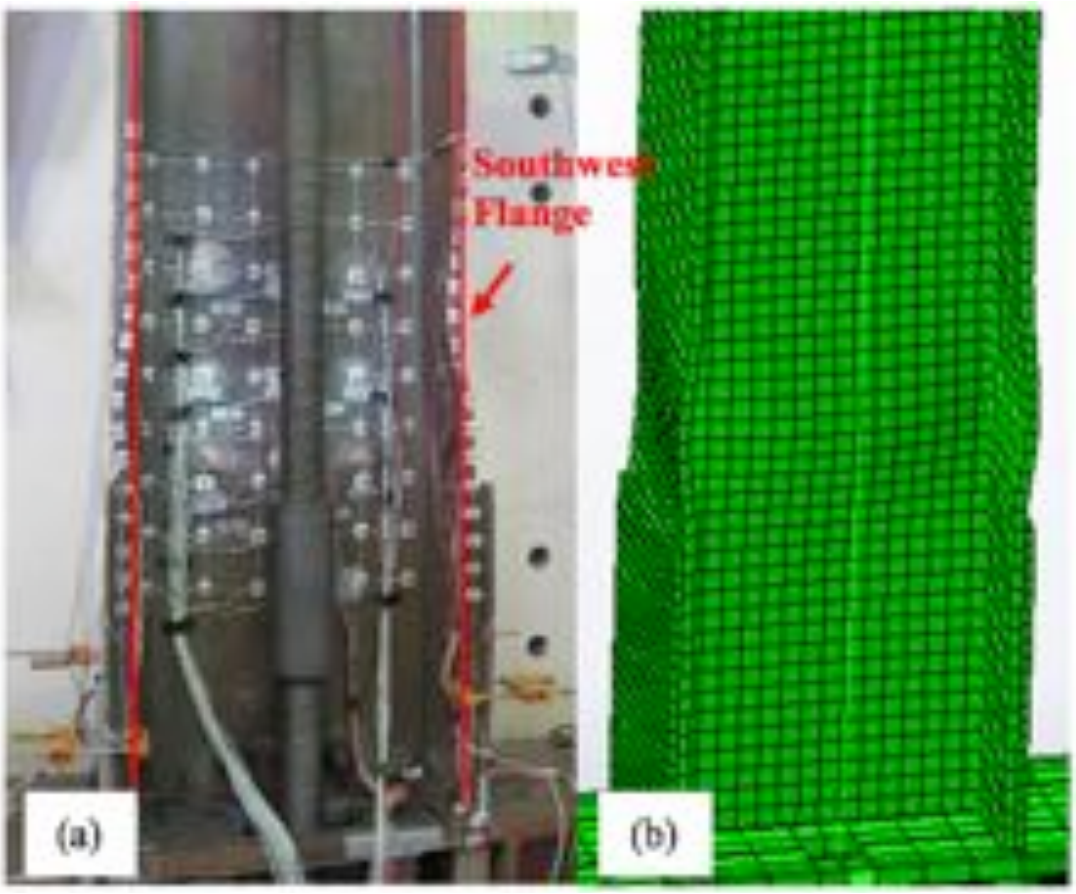

Figure 3.32: Comparison between simulated and experimental buckling shapes at the end of 9% drift (a) experimental buckling shape and (b) simulated buckling shape

3.6.4 LED Data and Buckled Shape

To investigate the buckled shape of the specimens in detail, displacement measurements from the LED markers used in the experiments are compared with the simulation results. Figure 3.33 shows the details of the LED marker locations. Six markers were located on the column flanges (not shown in Figure 3.33), while the rest of the markers are located along the edges of the beam flanges and on the beam web. Markers on the beam surfaces were placed in the region ranging from six inches below the end of the reinforcing plate to eighteen inches beyond the end of the reinforcing plate. As an example,

LED marker displacements are shown for Specimen 2, which showed significant local buckling in the test.

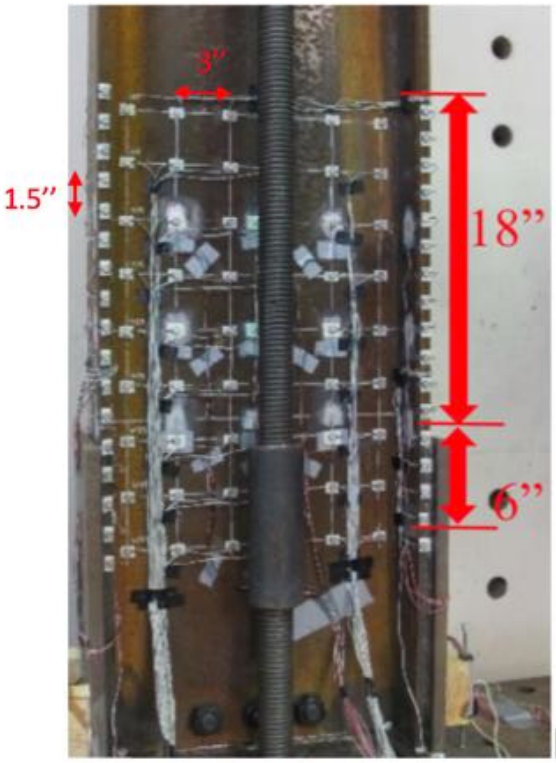

Figure 3.33: LED marker locations on the beam web and flanges [Hulsey, 2015]

Measured buckled shapes are shown for specific loading cycles. Figures 3.34 to 3.36 show the deformed shape of the beam flanges from the simulation and as measured by the LED markers in the experimental specimen for Specimen 2. Experimental results are shown as blue circles representing the location of each LED marker along the beam flanges, while simulation results showing the mid-thickness edge of the beam flange shell elements from the implicit analyses are shown as red lines. According to the data, the buckled shape and the buckling length from the ABAQUS simulation results are in agreement with the experimental LED markers.

The buckled shape, and more importantly the length over which buckling occurs, is critical in characterizing the strength degrading behavior of the beam, where such strength degrading behaviors are defined over the localization length (i.e., buckling length). The next chapter provides a detailed study on the determination and importance of the localization length.

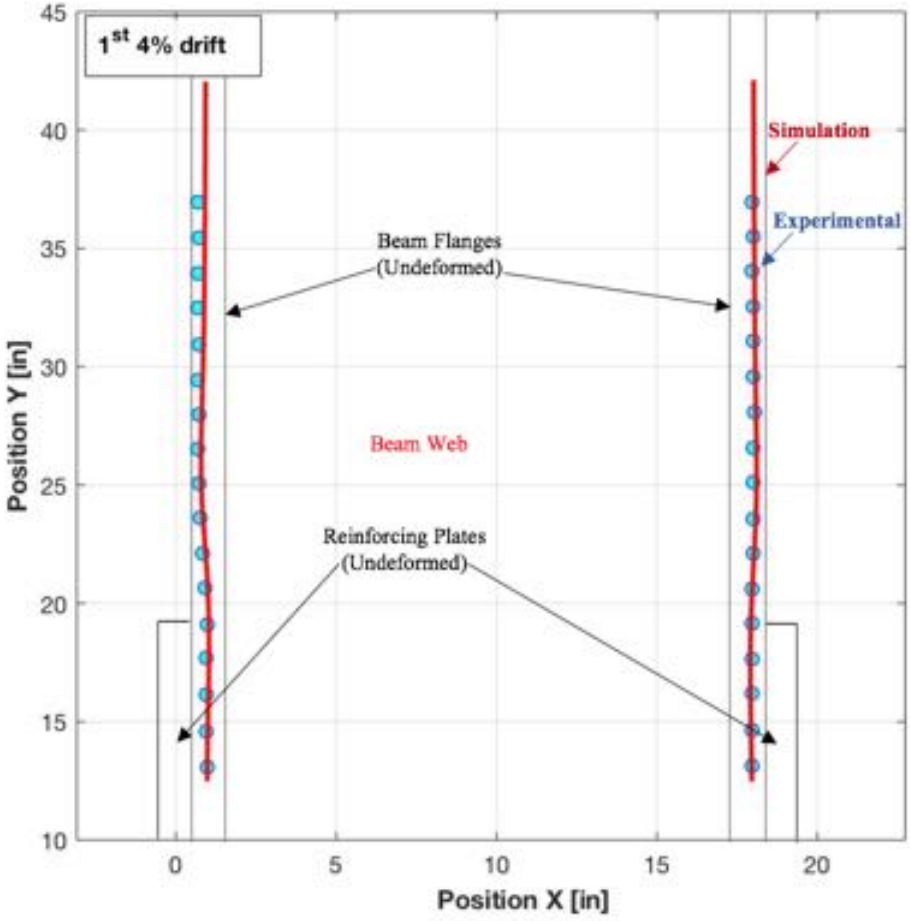

Figure 3.34: Experimental vs. simulation results for specimen with W18x55 beam at the end of the first north 4% drift cycle.

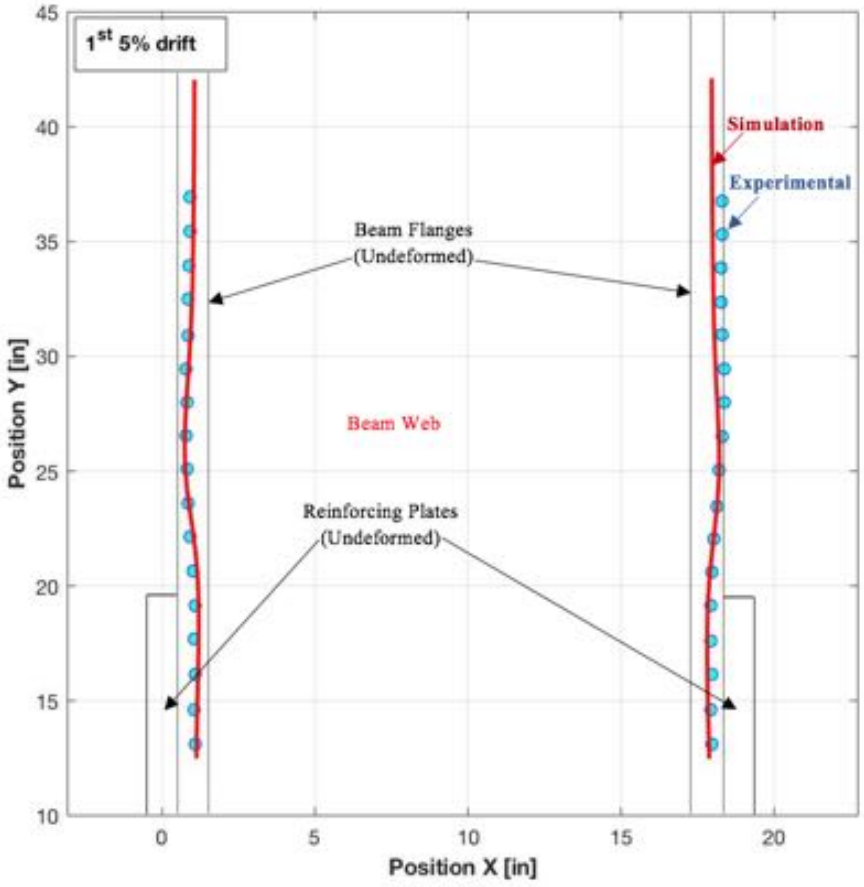

Figure 3.35: Experimental vs. simulation results for specimen with W18x55 beam at the end of the first 5% drift cycle.

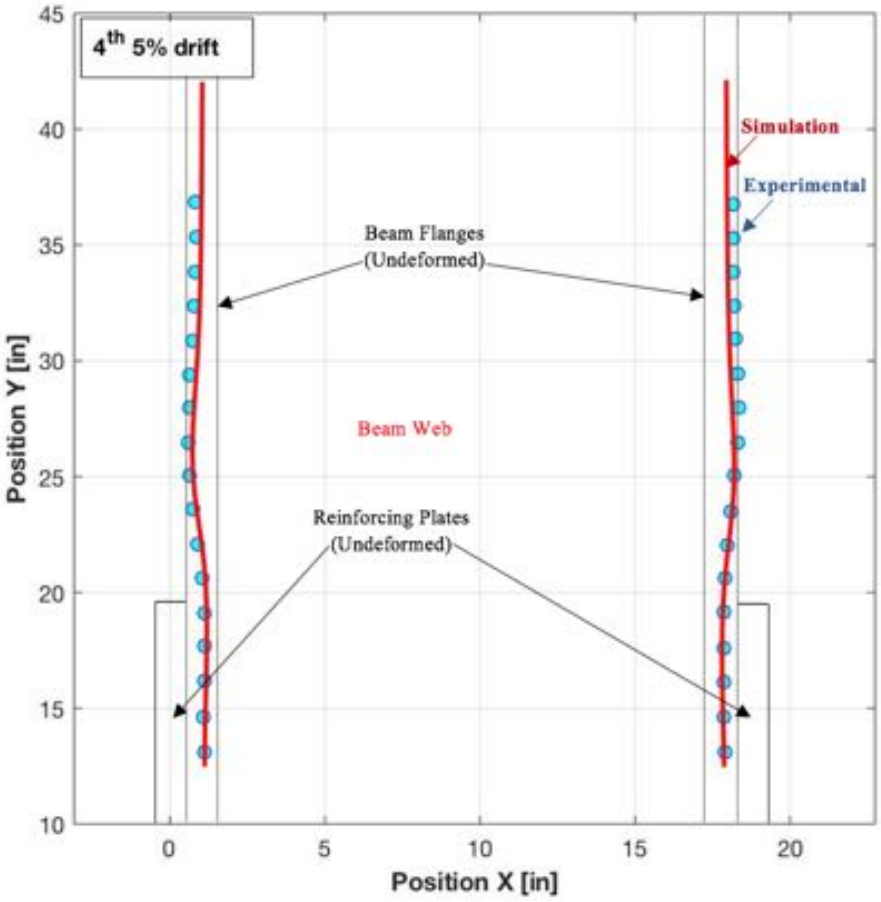

Figure 3.36: Experimental vs. simulation results for specimen with W18x55 beam at the end of the test

3.7 SUMMARY AND MODELING RECOMMENDATIONS

This section provides details of the finite element models used to simulate the strength degrading behavior of PT connections caused by beam local buckling. Details are described for modeling the PT connection structural members with shell and solid elements, modeling of post-tensioned tendons, and modeling of gap opening and closing behavior in the connections. Geometric and material nonlinearities, initial imperfections, and a mesh refinement study are included and explained in this section. Validation of the

finite element models are performed by comparing the simulation results with the results from PT connection experiments conducted by Hulsey (2015).

As previously mentioned, the S4R shell elements in ABAQUS are computationally efficient and can capture the observed local buckling within the cross section and associated connection strength loss when conducting analyses both with implicit and explicit solution techniques. The shell models are able to capture local buckling shapes and the associated strength degradation behavior. Modeling of PT connections with shell elements has previously only been documented in Clayton (2015) and Ahmadi (2016); therefore, modeling techniques presented in this chapter could be used in future studies of PT connections. As a result of this study, shell element models are selected for use in the parametric studies described in the following chapters, and the modeling and analysis techniques that are explained in this chapter are used in the following chapter for the parametric FE studies.

Chapter 4: Parametric Study to Investigate Local Buckling Behavior of PT Beam-to-Column Connections

4.1 INTRODUCTION

To investigate collapse performance of self-centering moment-resisting frames with PT beam-to-columns connections, initiation and progression of local buckling behavior must be investigated in detail. Modeling of strength degradation requires capturing changes in axial loads caused by PT forces due to the gap opening and closing phenomena or/and plastic shortening of beams. Previous studies on the strength degradation of PT connections due to beam local buckling and subsequent collapse performance of self-centering moment-resisting frames are limited. The initiation and the progression of local buckling behavior in PT connections is investigated in the experimental studies conducted by Hulsey (2015), and there are limited specimens in other experimental studies of PT connections that exhibited beam local buckling such as Garlock (2002) and Kim and Christopoulos (2009). Furthermore, Ahmadi et al. (2018) studied the collapse performance of self-centering moment-resisting frames numerically using the ABAQUS finite element software, where the beam-local buckling limit state was the primary strength degrading limit state leading to collapse. Guan et al. (2015) modeled self-centering frames with PT beam-to-column connections in the OpenSees analysis platform, where they studied the seismic performance of self-centering systems; however, they did not account for beam local buckling as beams are defined as elastic beam-column elements. To investigate collapse performance of self-centering systems with PT beam-to-column connections, it is necessary to capture strength degrading behavior caused by beam local buckling. Therefore, accurate modeling of strength deteriorating behaviors should be investigated, and models that are able to simulate these behaviors in computationally efficient ways are needed.

In beams of self-centering moment-resisting frames, the moment demand is proportional to the beam axial force demand from the PT elements, which varies as the PT elements elongate due to the gap opening phenomena. Thus, when the beam buckles locally due to the high axial demands, the beam shortens, thus reducing the PT force and beam moment demands, resulting in a high degree of coupling between the moment capacity of the PT connection and the shortening of the beam due to local buckling. Considering there have been limited studies on degradation behavior of these connections, parametric studies are performed in this research to further understand strength degradation behavior for a wide range of design parameters.

In this section, a detailed FE parametric study is conducted to understand degrading behavior and the parameters influencing the degrading behavior. The strength degradation behavior could be characterized by connection moment response, as well as localized beam stresses and axial shortening behavior of the beam. In this study, an effective stress-strain behavior is extracted from the buckling portion of the beam, which is then employed in simplified fiber-based models to model local buckling-induced strength degradation. Using an effective stress-strain behavior for modeling strength degradation behavior associated with local buckling has been studied for wide-flange sections and hollow structural steel sections by Kolwankar et al. (2015) and Suzuki et al. (2018), respectively. In reference studies, the effective stress-strain behavior is extracted over the buckling length to characterize the shortening of the beams, which is essential in capturing the localization of plasticity within the beam.

To obtain the effective stress-strain relationship, in this study, the connection model used in the FE parametric studies are similar in configuration to the specimens tested by Hulsey (2015), where a single connection is loaded cyclically without the presence of energy dissipation devices in the connection to focus only on the limit state behavior due

to beam local buckling. Due to limited experimental studies on this topic, parametric analyses using experimentally validated, detailed finite element models are performed to further study the strength degradation behavior of PT beam-to-column connections with a wide range of design parameters. The models in this parametric study have varying parameters including beam flange width-to-thickness ratio, beam web width-to-thickness ratio, initial PT force, and reinforcing plate length. Following the parametric studies, the buckling length of each model and the corresponding effective stress-strain behavior is obtained.

4.2 FINITE ELEMENT PARAMETRIC MODELS

To investigate strength degradation behavior of PT beam-to-column connections, a detailed parametric study is performed for untested cross-sections to supplement the limited existing experimental data. Parameters expected to affect the local buckling behavior most are considered in this study (Lignos, 2008; Moradi, 2015; Suzuki, 2018). These parameters include beam flange width-to-thickness ratio, beam web width-to-thickness ratio, initial PT force, and reinforcing plate length.

4.2.1 Finite Element Modeling

Detailed finite element models are prepared in this section based on the modeling recommendations presented in Chapter 3, and the material model for beam sections are chosen as the material model for the W18x76 flange given in Chapter 3. Furthermore, the models have the same basic geometric configuration as the Specimen 1 and Specimen 2 models presented and validated in Chapter 3. The designed connections are subjected to the cyclic loading discussed in Section 4.2.4, and results of the simulations are presented.

In design of PT beam-to-column connections, the beams are intended to remain essentially elastic under design earthquake demands. Thus, beam sections with local slenderness ratios beyond the highly ductile limit, such as those specified in the AISC *Seismic Provisions* (2016b), could feasibly be selected for the structures. (Note, that PT beam-to-column connections and self-centering systems are not currently codified in the AISC *Seismic Provisions*, thus there are no slenderness limits specified for this system.) Thus, a wide range of beam flange and web width-to-thickness ratios, which are known to be a critical parameter in local buckling behaviors, are considered in this study. Other parameters of interest include variation of the reinforcing plate length, beam depth, and the initial PT force, all of which affect the relative moment and axial force demands at the location where local buckling is expected.

The aim of this parametric study is to vary these design parameters to investigate their effects on the local buckling strength degradation behavior. Strength degradation behavior is characterized by extracting an effective stress-strain behavior from the FE model in the region of flange local buckling. This effective stress and strain are determined from the force in the flange and the axial shortening within the localized buckling region. The parametric studies are performed for the wide-flange steel beams with member slenderness $L_b/r_y < 50$ (where, L_b is the member's unbraced length, and r_y is the radius of gyration of the wide-flange cross-section), which mitigates the occurrence of global lateral buckling limit states. Therefore, only local buckling limit states are considered in the parametric studies and subsequent simplified models. The effective stress-strain behaviors characterized in this chapter will later be employed to simulate the strength degrading effects of local buckling in beam-column line element models with fiber cross-sections presented in Chapter 5.

4.2.2 Investigated Beam Cross-Sections and Design Parameters

A total of 40 wide-flange cross-sections are investigated in this study. The simulated cross-sections include web slenderness ratios between $32.9 < h/t_w < 57.5$ and flange slenderness ratios between $4.44 < b/2t_f < 9.47$ as shown in Figure 4.1. The figure also shows the highly ductile and moderately ductile web and flange slenderness limits according to AISC *Seismic Provisions* (2016b). λ_{md} and λ_{hd} in the figure represents limiting slenderness parameters for moderately and highly ductile compression elements, respectively. The selected sections are characterized with respect to the moderately and highly ductile slenderness limits, where sections that exceed the highly ductile limits for webs and flanges are Type I; those that exceed the web highly ductile h/t_w limit are Type II; and remaining sections that have highly ductile webs are represented with Type III (note, that all of the Type III sections except for one also have highly ductile flanges). The sections considered in the parametric studies are deep cross-sections varying between W16 and W36. The cross-sections are chosen based on the beam sections that are used in self-centering moment-resisting frame designs from previous studies (Garlock et al., 2007; Chou et al., 2006; Christopoulos et al., 2003; and Lin et al., 2013).

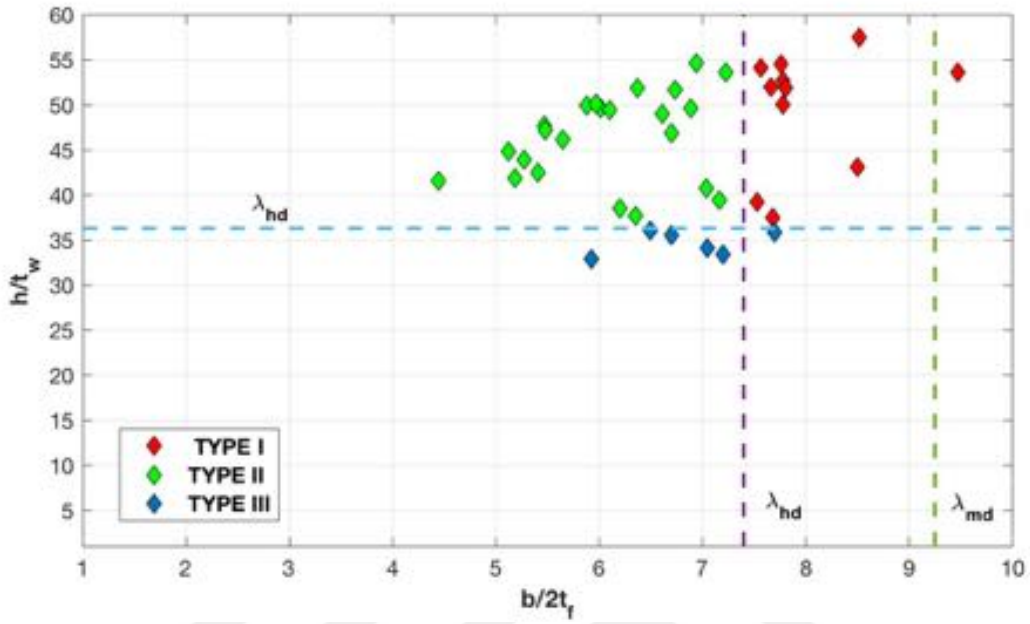

Figure 4.1 Local slenderness ratios of selected beam sections for parametric simulations, shown with respect to AISC Seismic Provisions (2016b) limits

For the PT beam-to-column connections generated for this parametric study, a W14 x 342 columns is used, which is larger than the column section used in the experimental study presented in Chapter 3. The larger column size is selected to accommodate the larger beam flange widths considered in the parametric study. The column members are intended to remain elastic, as the focus of this study is on beam local buckling limit states. All of the beams are laterally braced via restraints to prevent twist of the cross-section to maintain a member slenderness ratio, L_b/r_y, less than 50 to mitigate the occurrence of lateral torsional buckling limit states (at the location of 75.75 inches away from the beam contact region).

To prevent PT yielding, the initial PT force, T_{in}, for each model is selected around 30-40% of the ultimate strength of the PT material. According to a PT connection design procedure proposed by Christopoulos (2002), an initial PT stress of 30% of their ultimate stress is a good starting point to limit the occurrence of PT yielding at target drift levels.

Under this initial PT force, if no local buckling is observed in the beam, then the initial PT force is increased until local buckling is observed. The initial PT force for each simulation model is typically around 0.25-0.35 P_y, where P_y is nominal beam area times its nominal yield stress, which is consistent with the level of initial PT force with respect to beam yield strength in designs from previous researchers (Garlock et al., 2004). Details of the beam section and initial PT forces considered in this parametric study are given in Table 4.1.

The initial PT force is decided based on the observation of buckling in the parametric studies. In the first round of analyses, all beams had an initial PT force of 365 kips (30% of the PT ultimate stress), and beams with lower $b/2t_f$ ratios (beams from Type II and III categories) did not result in significant buckling and, therefore, did not exhibit strength degradation due to beam local buckling. To obtain degradation behavior for the considered beams, the initial PT force is increased incrementally to 0.25, 0.30, and 0.35 P_y until significant buckling was observed. The resulting initial PT forces that led to observed buckling are those reported in Table 4.1. The initial PT cross-sectional area is 4.08 in^2, and for the models that have increased initial PT force, the area is changed to 5.19 in^2 and 6.85 in^2 to maintain an initial PT force around 30-40% of the PT ultimate strength.

Table 4.1 Beam and initial PT force data used for parametric studies

Model Number	Beam Section	$\frac{h}{t_w}$	$\frac{b}{2t_f}$	T_{in} (kips)	$\frac{T_{in}}{P_y}$
# 1	W24x94	41.9	5.18	365	0.25
# 2	W24x131	35.6	6.7	481	0.25
# 3	W24x76	49	6.61	340	0.30
# 4	W24x104	43.1	8.5	380	0.25
# 5	W27x84	52.7	7.78	365	0.30
# 6	W30x99	51.9	7.8	365	0.25
# 7	W36x135	54.1	7.56	365	0.20
# 8	W30x90	57.5	8.52	390	0.30
# 9	W24x117	39.2	7.53	365	0.20
# 10	W27x146	39.4	7.16	539	0.25
# 11	W24x68	52	7.66	365	0.35
# 12	W33x118	54.5	7.76	365	0.25
# 13	W21x44	53.6	7.22	163	0.25
# 14	W21x48	53.6	9.47	176	0.25
# 15	W21x55	50	7.87	203	0.25
# 16	W21x101	37.5	7.68	365	0.30
# 17	W18x86	33.4	7.2	365	0.30
# 18	W30x132	43.9	5.27	385	0.20
# 19	W30x191	37.7	6.35	704	0.25
# 20	W30x148	41.6	4.44	544	0.25

Table 4.1 Continued

Model Number	Beam Section	$\frac{h}{t_w}$	$\frac{b}{2t_f}$	T_{in} (kips)	$\frac{T_{in}}{P_y}$
# 21	W30x108	49.6	6.89	365	0.25
# 22	W30x173	40.8	7.04	638	0.25
# 23	W27x178	32.9	5.92	656	0.25
# 24	W27x161	36.1	6.49	595	0.25
# 25	W36x170	47.7	5.47	626	0.25
# 26	W36x182	44.8	5.12	668	0.25
# 27	W33x130	51.7	6.73	365	0.17
# 28	W33x141	49.6	6.01	593	0.25
# 29	W16x67	35.9	7.7	371	0.30
# 30	W36x160	49.9	5.88	588	0.25
# 31	W36x150	51.9	6.37	553	0.25
#32	W33x221	38.5	6.2	815	0.25
# 33	W33x152	47.2	5.48	560	0.25
# 34	W30x124	46.2	5.65	548	0.25
# 35	W27x114	42.4	5.41	503	0.25
# 36	W21x111	34.1	7.05	371	0.25
# 37	W24x55	54.6	6.94	284	0.25
# 38	W24x62	50.1	5.97	320	0.25
#39	W21x62	46.9	6.7	320	0.25
#40	W21x50	49.4	6.1	257	0.25

In the PT connection, flange reinforcing plates are used to prevent flange yielding under the large compressive stresses generated by the rocking behavior. Reinforcing plate thickness is defined according to given formula, Garlock (2004):

$$A_{rp} \geq \frac{C - C_{f,y}}{\sigma_{rp,y}} \quad \text{(Eq. 4.1)}$$

where C is the contact force within the connection, $C_{f,y}$ is the beam flange yield force that is equal to the beam flange area multiplied with the yield stress of the beam, and $\sigma_{rp,y}$ is the nominal yield stress of the reinforcing plate. The reinforcing plate length is selected as the nominal beam depth for each model as recommended by Kim (2008), who states that the nominal beam depth is the minimum reinforcing plate length that should be chosen to prevent yielding in the beams at early drift cycles.

4.2.3 Modeling Techniques

Details of the shell finite element models for ABAQUS/Standard and ABAQUS/Explicit analyses are discussed in Chapter 3. Recall that ABAQUS/Standard, which employs implicit solution algorithms, was used primarily due to its computational efficiency; however, when implicit static analyses failed prior to completion of the prescribed loading protocol (described in Section 4.2.4) due to convergence challenges, ABAUS/Explicit was used, which employs explicit solution algorithms over long durations to simulate quasi-static loading as described in Chapter 3. The majority of sections with web slenderness ratios, h/t_w, higher than 45 needed to be analyzed with explicit analyses, as shown in Figure 4.2.

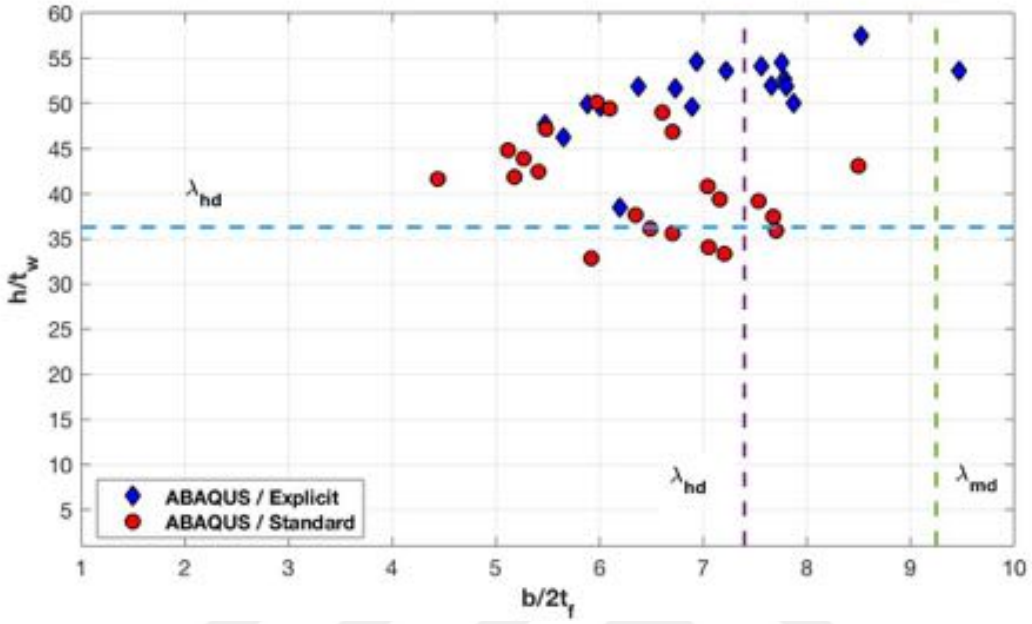

Figure 4.2 Distribution of analysis method with respect to beam local slenderness ratios

It should be noted that for ABAQUS/Explicit analyses, mass scaling is used to decrease computational runtime but is limited such that the ratio of the kinetic energy to internal energy is kept less than 10% of the internal energy as recommended by Behbahanifard (2004). As explained in Chapter 3, for the implicit analysis in ABAQUS/Standard, PT initial stresses are defined using the bolt load function; while for ABAQUS/Explicit, which does not include the bolt load function, initial stress is applied by introducing a temperature "load" in the first analysis step with a coefficient of thermal expansion in the PT element, before any other load is applied to the system. This temperature "load" is held constant during the analysis.

4.2.4 Displacement Load History

For the parametric studies that are conducted with ABAQUS/Standard, the load protocol from the AISC *Seismic Provisions* (2010) is applied, as shown in Figure 4.3. The

models are loaded up to 10% drift to investigate strength degrading behavior of PT connections.

For quasi-static loading of the parametric models in ABAQUS/Explicit, the same number of cycles and drift amplitudes are used, and the time scale of the applied loading is long enough to ensure that inertial effects are negligible in the model. The kinetic energy of the deforming material should be monitored such that the ratio of the kinetic energy to internal energy should be less than 10% during the simulation Behbahanifard (2004). Therefore, the mass scaling for parametric studies decreased to 5 based on the high kinetic energy values compared to threshold value of 10%. In addition, the loading sequence is applied as a *Smooth Step* loading history in ABAQUS to obtain a smooth response and prevent the large changes in acceleration and velocity that come with a ramp function. The displacement-time history used in ABAQUS/Explicit analyses is shown in Figure 4.4.

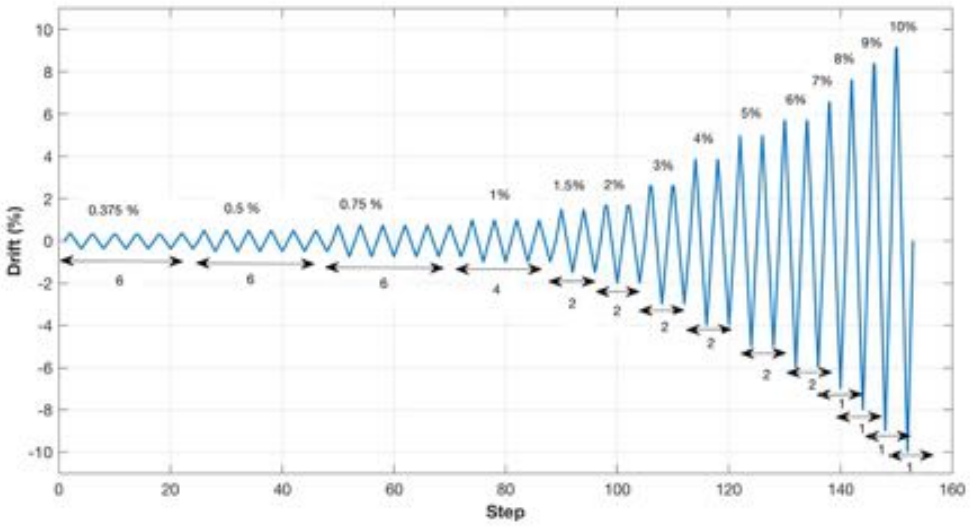

Figure 4.3 Displacement loading history for parametric analysis in ABAQUS/Standard

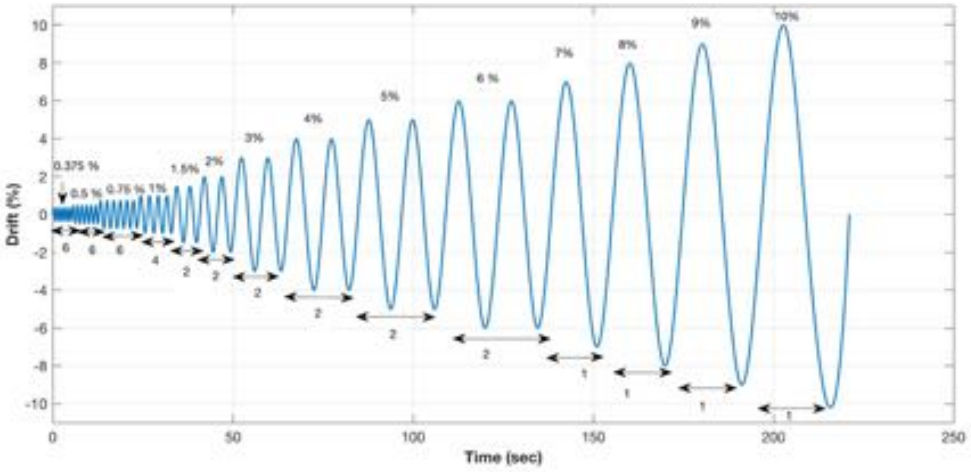

Figure 4.4 Displacement loading history for parametric analysis in ABAQUS/Explicit

4.3 RESULTS OF PARAMETRIC STUDIES

In this section, results of the parametric studies are discussed, starting with the buckling length that is obtained as a result of parametric studies. Following the buckling length, the effective stress-strain behavior is defined and parameters affecting the degradation behavior are explained.

4.3.1 Observed Buckling Length

The definition of the buckling length, or the localization length, is critical for modeling the strength degradation behavior for more simplified *OpenSees* models, which will be described in more detail in Chapter 5. As demonstrated in Chapter 3, the buckling length observed in the finite element validation models are similar to those observed during the experimental tests. In this section, the observed buckling length from the finite element models are investigated.

To extract a buckling, or localization, length from the finite element model, a methodology proposed by Kolwankar et al. (2018) has been used. In this methodology the

equivalent longitudinal strain, $\varepsilon_{\text{equivalent}}$, along the length of the beam is used to evaluate the length over which localized shortening, or buckling, occurs. The equivalent longitudinal strain is essentially the change in length between two arbitrary points on the beam flange divided by the original distance between them, which can be calculated as

$$\varepsilon_{\text{equivalent}}\ (x,z) = \frac{\left|\overrightarrow{\Delta L^{flange}(x,z)}\right| - \left|\overrightarrow{\Delta L^{flange}(x,z)}.\overrightarrow{\Delta L^{web-centerline}(x)}\right|}{\left|\overrightarrow{\Delta L_0^{web-centerline}(x)}\right|} \quad \text{(Eq. 4.2)}$$

where $\varepsilon_{\text{equivalent}}\ (x,z)$ is the equivalent longitudinal strain determined at each location of the reference coordinates x (along the beam length) and z (along the flange width). $\overrightarrow{\Delta L^{flange}(x,z)}$ and $\overrightarrow{\Delta L^{web-centerline}(x)}$ are the vectors representing the local orientation and length of a line segment on the flange and web centerline, respectively. Relatedly, $\left|\overrightarrow{\Delta L_0^{web-centerline}(x)}\right|$ denotes the magnitude of a line segment on the web centerline in the undeformed state. The details of the equation can be found in Kolwankar et al. (2018) and is shown schematically in Figure 4.5. Once the equivalent strains are calculated at each location along the flange width, strain rates can be determined by numerical differentiation of the equivalent strain with respect to loading increments (i.e., time), and the localization length can be obtained. Particularly, the localized region experiences a negative strain rate, while the strain rate outside of this region is positive.

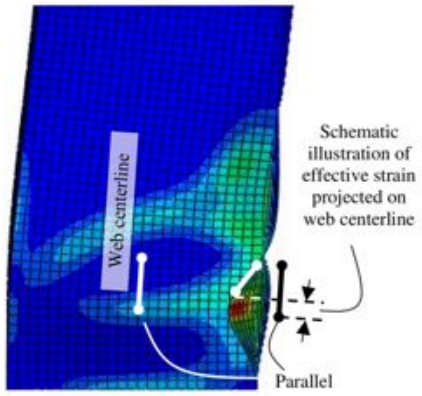

Figure 4.5 Projected strains [Kolwankar et al., 2018]

For each parametric model, the given formulation is performed to observe the buckling length. Kolwankar et al. (2018) found in a study of beams with conventional moment-resisting connections that the buckling length, L_b, tended to be around *2.25* times the beam flange width, b_f, under applied cyclic loading, which appears to be consistent with results from this parametric study. Figures 4.6 and 4.7 show examples of the resulting buckled shape and length for simulation results of Model Number 3 and Model Number 12, as documented in Table 4.1. For Model Number 3, $L_b = 2.25 \times 8.97 = 20.18$ *inches*, and the model was found to have a buckled length of 22.4 inches as shown in Figure 4.6, and for Model Number 12, $L_b = 2.25 \times 11.5 = 25.875$ *inches*, and the model was found to have a buckled length of 27 inches as shown in Figure 4.7.

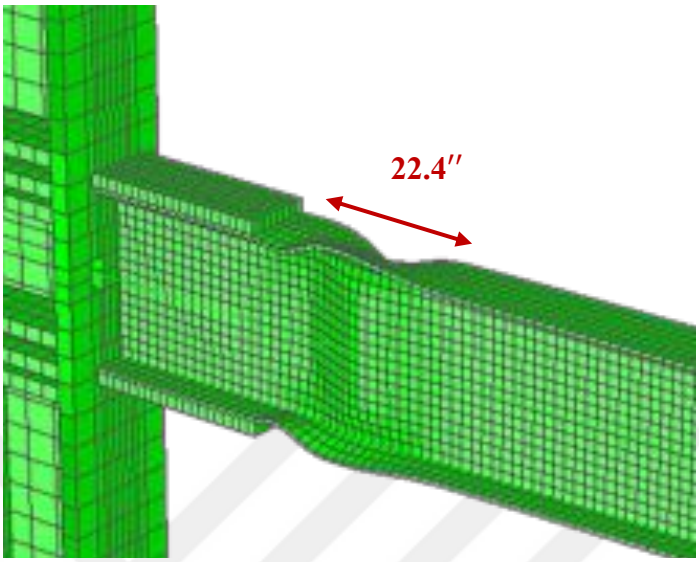

Figure 4.6 Buckling length of Model Number 3

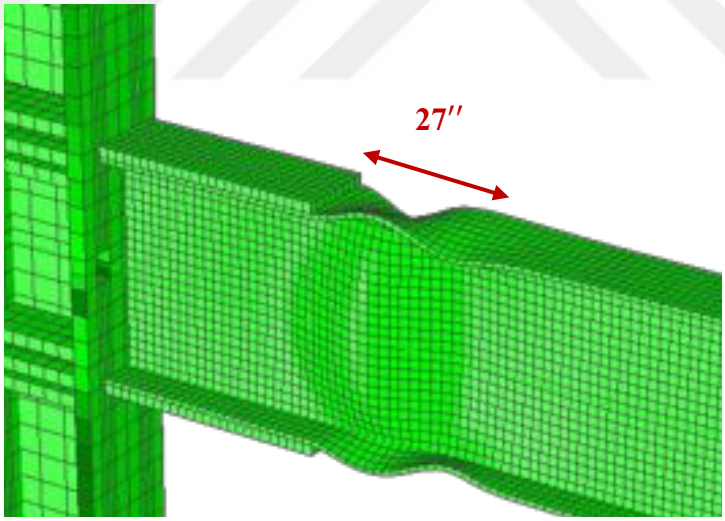

Figure 4.7 Buckling length of Model Number 12

4.3.2 Characterization of post-buckling behavior under cyclic load

To characterize the degrading behavior of locally buckled beams in PT beam-to-column connections, effective stress and strain data is extracted from the buckled region of the FE models. Buckling occurs when a critical stress is reached, after which the compressive strength begins to degrade. Observations of extracted stresses and the overall response behavior of the connection indicate that strength degradation between repeated cycles at the same displacement is not significant. Therefore, the effective stress-strain response of the buckled region of the beam in a PT connection is characterized by its backbone response. Later in Chapter 5, this effective stress-strain backbone behavior with a softening compression branch will be employed in a fiber cross-section beam-column element to simulate the strength degrading behavior associated with local buckling.

The effective stress-strain response for the beams is extracted from the FE models along the buckling length, as determined by $2.25*b_f$. Strain values are calculated as the net shortening divided by the defined buckling length, and stresses are obtained directly from the FE model. The effective stresses and strains are averaged across the flange width to provide one effective stress and strain value at each location along the longitudinal axis of the flange. The effective stress can be determined at any location along the buckled length; however, the effective stresses presented in this study are taken at the end of the reinforcing plate (taken from the nodes just beyond the end of the reinforcing plate). The selection of this location for extracting effective stress-strain responses will become apparent in Chapter 5 when discussing the location of different integration points in the beam-column element formulation. Figures 4.8 and 4.9 show typical effective stress-strain responses for the beams of Model Number 22 and Model Number 11, respectively. Due to applied compressive loads in the beam due to the PT elements, the effective stress-strain response only exhibits compressive strains and never reaches the yield stress in tension. The

backbone or envelope response in compression can be characterized by a multi-linear response. Initially the response is elastic and exhibits a hardening response after reaching the yield stress. After reaching a peak stress at some stress larger than yield, the post-buckling region starts, as characterized by a negative slope. At increasing deformations, the negative slope flattens out and the residual strength stabilizes. This behavior is related to stabilization of local buckling waves (Suzuki, 2018).

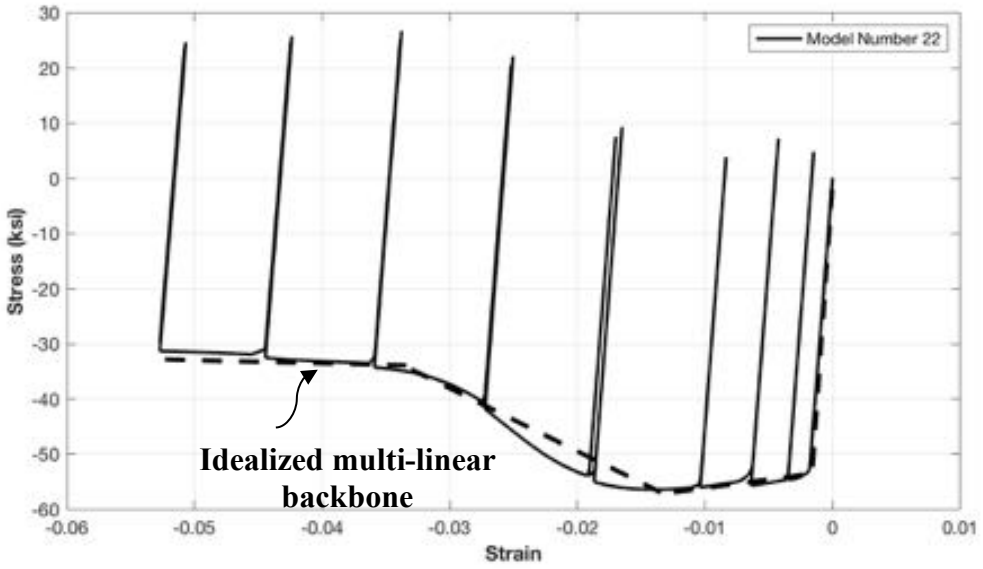

Figure 4.8 Extracted effective stress-strain relationship and idealized multi-linear backbone curve for Model Number 22

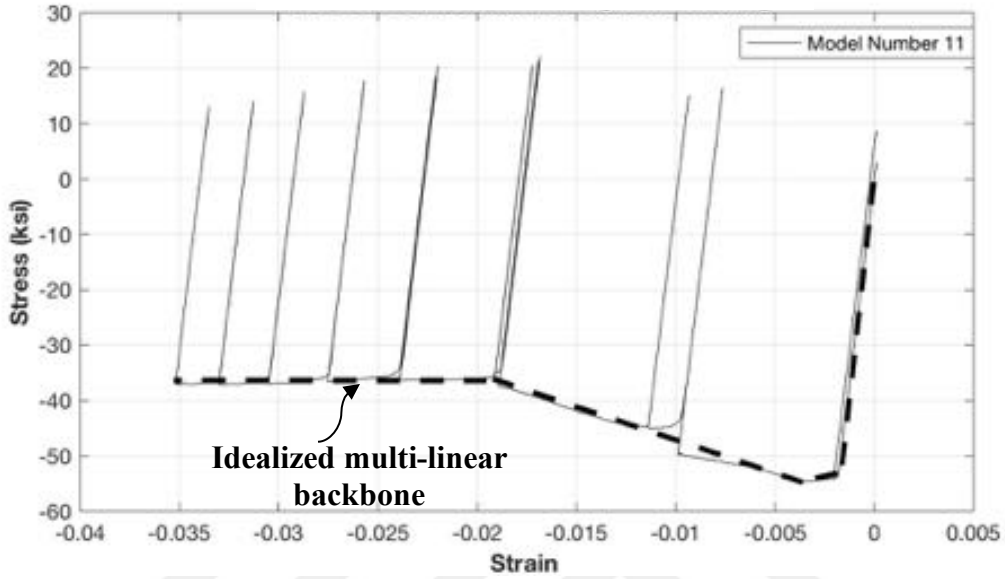

Figure 4.9 Extracted effective stress-strain relationship and idealized multi-linear backbone curve for Model Number 11

As shown in Figures 4.8 and 4.9, under applied PT loads and lateral loads, there are three main loading regions: an elastic region, a post-yield region, and a post-buckling region that is initiated at the critical stress, where this peak stress is less than the ultimate stress that is obtained from the coupon test results. Determining the transition points between these distinct regions of the effective stress-strain response provides the key parameters to develop an idealized multi-linear backbone, and these key parameters can be determined based on key connection design values. The proposed multi-linear backbone formulation can also be easily implemented in material models that are already available in various finite element software. The key parameters for the idealized multi-linear backbone curve are defined using the variables shown in Figure 4.10.

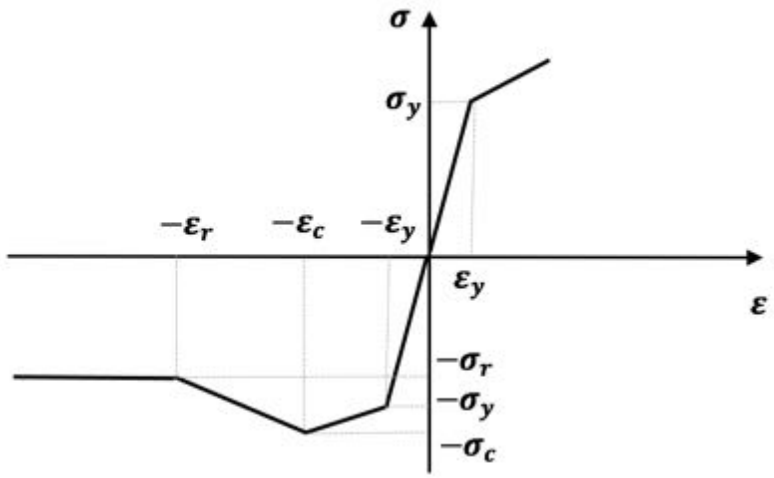

Figure 4.10 Key parameters for the idealized multi-linear backbone curve

In this figure, σ_y and ε_y denote yield stress and yield strain, respectively, which can be obtained directly from the material coupon tests. The critical stress, σ_c, is the peak stress at which strength degradation initiates and this value is less than the ultimate stress, σ_u. The corresponding strain value for the critical stress is ε_c. Finally, σ_r and ε_r are residual stress and strains representing the stress and strain value at which the negative slope of the post-buckling region ends, after which the stress remains constant. The tension side of the material can be defined based on the results of the material coupon test as it is expected that PT connections do not experience yielding in tension.

As previously outlined, each key point can be generalized for different beam sections through statistical analysis of the results obtained from the parametric studies. The parameters that will be defined and extracted from the FE results are: σ_c, σ_r, ε_c, and ε_r, and corresponding empirical equations will be provided in Chapter 5.

4.3.3 Variation in Initial PT Force and Reinforcing Plate Length

The length of the reinforcing plates is important in preventing the initiation of local buckling. It has been shown in previous research (Garlock, 2002; Moradi et al., 2015) that connections with shorter reinforcing plate lengths or no reinforcing plates experience local buckling and strength degradation earlier than ones with well-designed reinforcing plates. Figure 4.11 shows the effect of reinforcing plate length on the effective stress-strain response for Model Number 22. As observed in this figure, reinforcing plate length has a slight effect on ε_c, and ε_r while there is no significant effect on the other key parameters. Figure 4.11 shows the backbone curve for each model to emphasize the difference in the critical stresses.

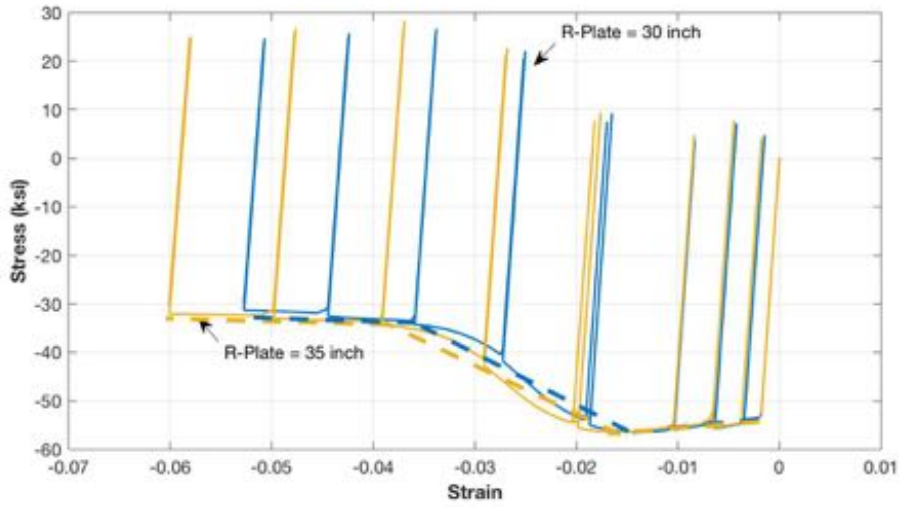

Figure 4.11 Effect of reinforcing plate (R-Plate) length on effective stress-strain response for Model Number 22

Secondly, the same researchers (Garlock, 2002; Moradi, 2015) observed that connections with higher initial PT force experience beam local buckling earlier than ones with lower initial PT force. Figure 4.12 and 4.13 shows comparisons for Model Specimen

12 and Model Specimen 11, respectively. According to these figures, the effect of initial PT force on the effective stress-strain behavior is a slight lowering of σ_r with increased initial PT force.

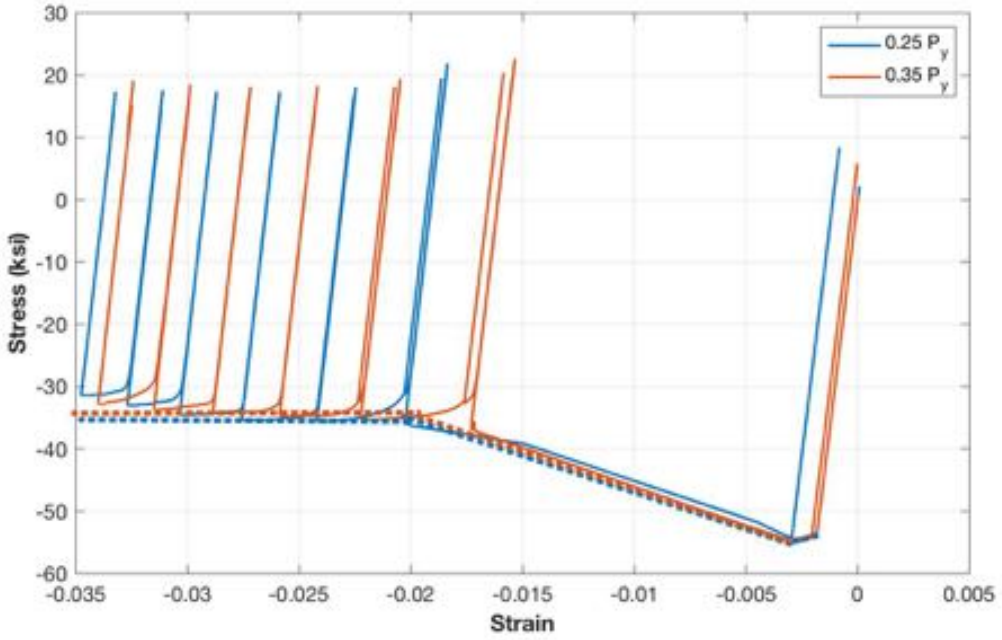

Figure 4.12 Effect of initial PT force (as a proportion of beam yield force, P_y) on effective stress-strain response for Model Number 12

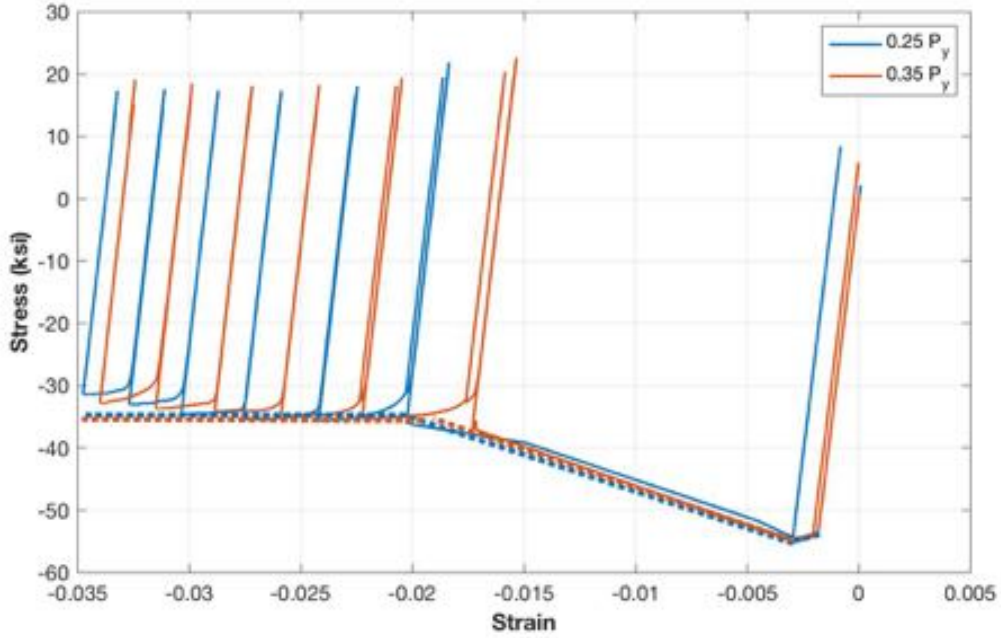

Figure 4.13 Effect of initial PT force (as a proportion of beam yield force, P_y) on effective stress-strain response for Model Number 11

4.4. SUMMARY AND CONCLUSIONS

This chapter investigates local buckling-induced strength degradation for PT beam-to-column connections through characterization of effective stress-strain relationships for the beam flanges. The degradation of strength occurs due to beam local buckling that is caused by the excessive compression forces in the beam flanges. To investigate the PT connection design parameters affecting the strength degradation behavior, a parametric study is performed using detailed FE models. The effective stress-strain relationship within the buckling length is extracted from the FE analysis results, which shows the beam experiences only compressive strains throughout its reverse cyclic load history due to the large compressive forces from the PT elements; thus, only the compressive nonlinear response is of interest in this study. Results show that the backbone of the compressive

stress-strain behavior follows a multi-linear trend. Key points of this generalized multi-linear backbone will be characterized using regression analysis in the following chapter.

As will be presented in the subsequent chapter, this nonlinear stress-strain behavior will be applied to fiber sections at predefined hinge locations in the beams to capture the strength degrading effects of local buckling in simplified beam-element models that cannot explicitly simulate local buckling phenomena. The very minor changes in stress-strain behavior due to changes in initial PT force and reinforcing plate length are also discussed.

Chapter 5: Fiber-Based Modeling of Strength Degradation in PT Beam-to-Column Connections

5.1 INTRODUCTION

Collapse assessment of buildings has gained large attention in the field of performance-based earthquake engineering (e.g., Christopoulos et al., 2003; Deierlein et al., 2003; Moehle et al., 2004; Burton et al., 2016) and in evaluation of seismic design building codes (FEMA P-695). A significant number of numerical and experimental studies have been conducted to assess the seismic performance of various structural building systems, including steel moment resisting frames (e.g., Roeder, 1993; Medina and Krawinkler, 2003; Khandelwal and El-Tawil, 2006) and reinforced concrete frames (e.g., Liel, 2008; Feng et al., 2015); however, there has been limited research on the collapse performance of self-centering moment resisting frames with PT beam-to-column connections. Previous work by Ahmadi et al. (2018) has shown that beam local buckling in PT beam-to-column connections could be a leading factor in the strength degradation and collapse of self-centering steel moment frames, warranting further research on this topic.

Various modeling approaches have been proposed to simulate strength and stiffness degradation behaviors in beams. Deterioration modeling of beams is typically based on concentrated plasticity models with specified moment vs. rotation responses. This method has been applied previously to simulate the behavior of beams with conventional moment resisting beam-to-column connections (Lignos and Krawinkler, 2011). However, traditional moment vs. rotation concentrated plasticity models do not account for the variable axial load in PT connections that influences the coupled flexural-axial response in the beam, which is essential when modeling the beams of PT beam-to-column connections, as axial load in the beams varies greatly due to the gap opening and closing phenomena

within the connection. Therefore, accurate modeling of strength degradation behaviors in PT beam-to-column connections considering axial-flexural interactions should be investigated.

In this chapter, a fiber-based model is proposed for use in a nonlinear beam-column element to capture the strength degradation associated with local buckling in PT beam-to-column connections. The strength degrading behavior is modeled using key parameters derived from the effective stress-strain relationships that are extracted from the finite element simulation results presented in Chapter 4. These generalized effective stress-strain models are then applied to fiber cross-sections in beam-column elements in the OpenSees simulation platform (McKenna 1997). A plastic hinge integration approach is employed to model the beams using the *beam with hinges* force-based beam-column element in OpenSees. The degrading stress vs. strain model parameters are applied via the *Hysteretic* material model that is available in OpenSees material library, which are then applied to the fibers of a fiber cross-section defined for the integration points within the predefined beam hinge regions. The results from the proposed fiber-based modeling approach are compared with those from PT beam-to-column connection experiments performed by Hulsey (2015).

It is worth noting that this approach of implementing FE-extracted effective stress-strain behaviors, which are used to characterize the strength loss and beam shortening associated with beam local buckling, into OpenSees fiber-based models uses nonlinear fiber material models to simulate section-level geometric nonlinearity. OpenSees is able to capture global geometric nonlinearity that arises from differential displacement of element nodes through various geometric transformations available in the software, which can be used to capture system-level instabilities, as well as member-level buckling if multiple elements are used to simulate the deflected shape of the member. OpenSees fiber-based elements are not, however, able to capture local section-level buckling. Thus, this approach

of simulating local geometric nonlinearity as an equivalent material softening behavior is employed.

5.2 FIBER-BASED MODELING

Modeling the softening behavior in the beam members of PT beam-to-column connections requires consideration of axial-bending interaction. This interaction can be simulated through nonlinear force-based or displacement-based beam-column elements that employ fiber cross-sections at integration points as shown in Figure 5.1. In these models, integration of force-deformation response is performed at sections along the member length (Scott and Fenves, 2006). Displacement-based beam-column elements assume a linear curvature along the element length with a weak enforcement of equilibrium, thus requiring many elements to simulate a nonlinear curvature distribution; while force-based beam-column elements assume linear moment distributions along the element length and strictly enforce force equilibrium (Neuenhofer and Filippou, 1997). In this research, a force-based beam column element is selected to model the beams, because (1) the force-based formulation helps to minimize the number of degrees of freedom in the structure (Scott and Fenves, 2006), (2) and it allows the use of different types of distributed plasticity and plastic hinge integration methods. Plastic hinge integration methods, which are used in this study, confine softening behavior into a predefined plastic hinge length, while the remainder of the element is linear elastic. Therefore, if a fiber cross-section is applied to the hinge integration points, the strength degradation at the end of a beam due to local buckling can be modeled accounting for axial-bending interaction. Figure 5.2 shows an example of a force-based beam-column element with plastic hinges, modeled with the midpoint hinge integration approach.

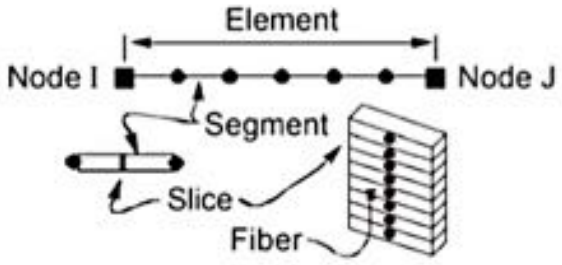

Figure 5.1 Fiber line element geometry and description in OpenSees [Garlock, 2002]

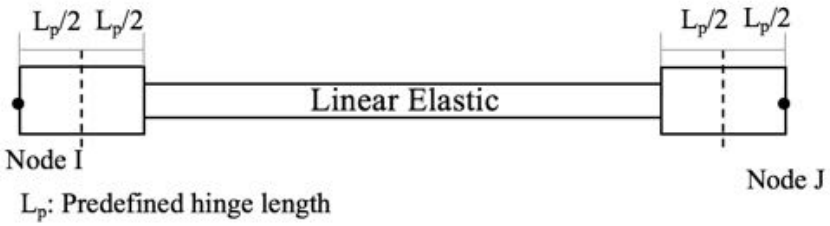

Figure 5.2 Beam with hinges model employing a midpoint hinge integration

5.3 OpenSees Modeling of PT Beam-to-Column Connections

Simplified fiber-based modeling of PT beam-to-column connections is performed in the OpenSees (Version 2.5.0) simulation platform (McKenna 1997). Figure 5.3 shows the details of the proposed connection model.

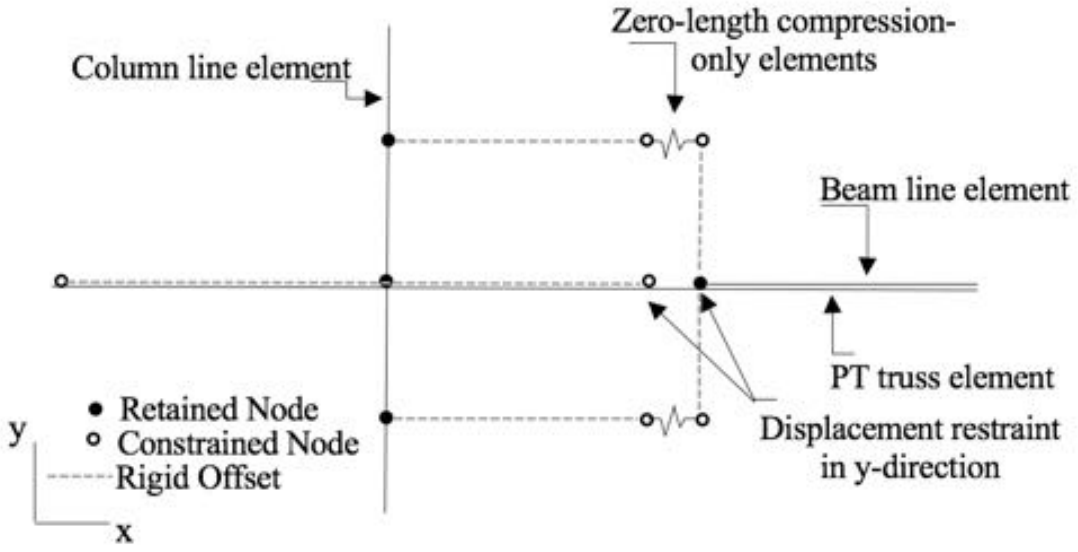

Figure 5.3 Schematic of PT beam-to-column connection modeling in OpenSees

The column is modeled by using force-based beam-column distributed plasticity line elements with five Gauss-Lobatto integration points. Although the columns are expected to remain elastic during the simulations, since this study focuses on beam nonlinearity, fiber cross-sections are defined with a Giuffre-Menegotto-Pinto (*Steel02*) stress-strain model for the column with a 50 ksi yield strength and 1% hardening ratio. The column is connected to the beam via zero-length compression-only elements that simulate the gap opening behavior at the extreme fibers of the beam reinforcing plates that bear on the columns. The zero-length compression-only elements are defined using the *Elastic No Tension* (ENT) material model with a compression stiffness of twenty times of the axial stiffness of the beam as explained in Chapter 3. Rigid offsets (modeled using stiff beam-column elements) are used to model the depths of the column and beam within the connection, as shown in Figure 5.3. To restrict the beam displacement in the y-direction, similar to the restraint provided by the slotted holes in the shear tab, the *equalDOF*

command is used to ensure the node at the ends of the beam and the node offset from the column to the column flange have the same y-direction displacement.

The beam line element is modeled in two sections to represent the portion of the beam with the flange reinforcing plates and the portion without. Along the main portion of the beam without flange reinforcing plates, a force-based beam-column element with predefined hinge lengths is used, where fiber sections are assigned to the integration points within the hinges. The predefined hinge length is defined as *2.25 times the flange width* based on the results presented in Section 4.3.1. The *Hysteretic* material model is used to model the nonlinear effective stress-strain behavior extracted from the FE models in Chapter 4. The details of *Hysteretic* material model are given in the following section.

While it is expected to remain elastic, the rest of the beam with the flange reinforcing plates is modeled with distributed plasticity force-based beam-column elements with five Gauss-Lobatto integration points to capture any potential nonlinearity, where the fiber cross-sections account for the added flange thickness from the reinforcing plate. The Giuffre-Menegotto-Pinto (*Steel02*) material model is used for the stress-strain response of the reinforced sections of beam with a yield strength equal to the yield strength assigned to the *Hysteretic* material used for the interior portion of the beam.

Finally, PT members are modeled using corotational truss elements, and the total area of the PT bars are lumped into one cross-sectional area located at the centroid of the PT bar group, which is typically colinear with the centroid of the beam. The PT elements are modeled using the *Steel02* material in OpenSees, which allows for input of an initial stress, with yield strength of 150 ksi and a 5% hardening ratio. The first step in each analysis was the application of the initial PT forces using an analysis step without any external applied load; then, cyclic loads are applied to the system using displacement-controlled analysis.

5.4 *HYSTERETIC* MATERIAL MODEL

The proposed stress-strain constitutive model used to model the strength degrading behaviors associated with local buckling in the predefined hinge length is implemented using the *Hysteretic* material from the OpenSees Uniaxial Material Library. Figure 5.4 shows the multi-linear backbone response of the *Hysteretic* material. This material is also able to capture cyclic unloading stiffness degradation and hysteretic pinching using model parameters not shown in the figure, although these features are not employed in this study. The backbone relationship is defined using stress and strain values for key transition points in the backbone. According to the definition of the *Hysteretic* material, if there is a negative stiffness between the second and third points of the backbone (i.e., *$s3p*≤*$s2p* and |*$s3n*|≤|*$s2n*| in Figure 5.3), the envelope of the material after it exceeds the strain of the third point (i.e. beyond *$s3p* or *$s3n*) is a flat response with a constant stress equal to *$s3p* or *$s3n*. The values selected to define the backbone response are determined based on the effective stress-strain relationships extracted from the detailed finite element modeling, as discussed in the next section.

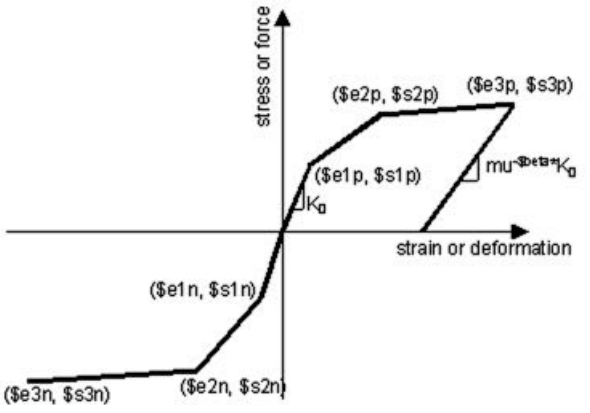

Figure 5.4 Definition of *Hysteretic* material in OpenSees

5.5 APPLICATION OF EFFECTIVE STRESS-STRAIN RELATIONSHIP

A schematic showing the process of extracting the effective stress-strain relationship from finite element parametric study results and applying them in OpenSees fiber models is shown in Figure 5.5. Referring to the figure, the focus of this research is to capture the degradation behavior due to beam local buckling in PT beam-to-column connections without energy dissipation devices. The parametric studies are discussed in Chapter 4 and results are used to obtain the effective stress-strain relationships in the buckled region of the beam. In Chapter 4, the effective stress-strain relationship is extracted from the flanges at the end of reinforcing plates to represent the general behavior of the degradation response, where stresses are averaged through the flange width and strains are obtained as the net displacement divided by the buckling length and averaged through the flange width.

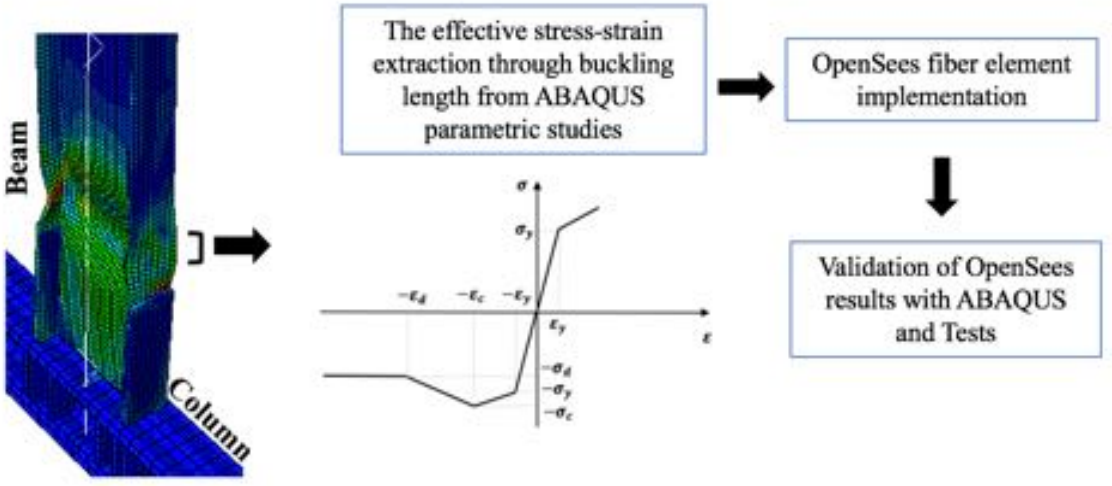

Figure 5.5 Schematic and organization of the research in extraction and application of the effective stress-strain relationship

At this point, the strength degradation behavior observed in the effective stress-strain plots from ABAQUS must be generalized to a form that can be implemented in

OpenSees. The general behavior of the extracted stress-strain behavior follows a post-yield hardening slope, a post-buckling strength degradation, and a post-buckling residual stress as discussed in Section 4.3.2. Figure 5.6 shows the effective stress-strain behavior extracted from *Model Number 22*, whose properties are defined in Table 4.1, at the end of reinforcing plates, and the superimposed lines are used to represent important regions in the degradation behavior. Referring to the figure, line 1 and line 2 are chosen based on points where the slope changes from degradation to stabilization. The intersection point of these two lines is chosen as the key parameters of σ_d and ε_d, or the third point in the *Hysteretic* material backbone. Determination of these and other critical points from the backbone response are discussed in more detail in Section 5.7. Lastly, in Section 5.9, results implementing the proposed *Hysteretic* material model in OpenSees are verified by comparing them with results from experiments and from ABAQUS finite element models, as shown in Figure 5.7 for *Model Number 5*, which has a W27x84 beam section and an initial PT force of 365 kips. Similar results are obtained for the other parametric study specimens and reference experiments.

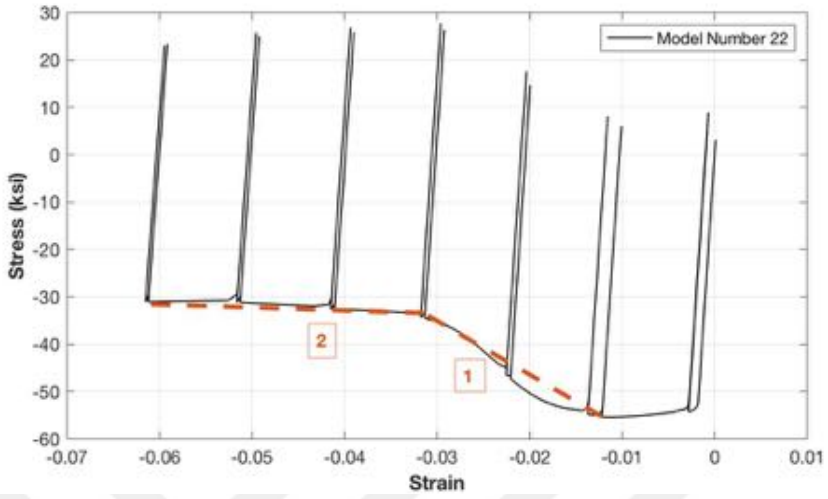

Figure 5.6 Generalized strength degrading slope and residual stress extracted from effective stress-strain responses

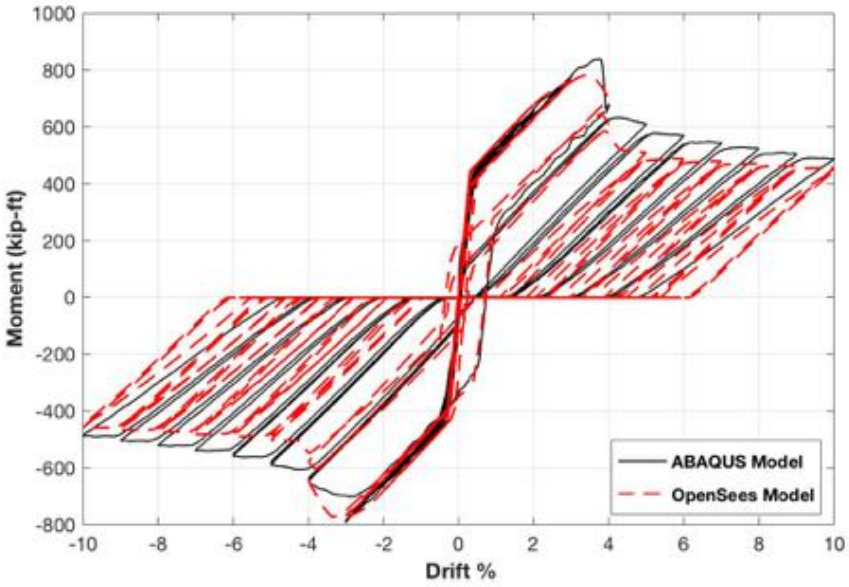

Figure 5.7 Comparison of OpenSees and ABAQUS modeling results for *Model Number 5*

Figure 5.7 shows results for connection moment vs. drift response for the OpenSees model that uses the modified Gauss-Radau hinge integration method available in OpenSees, where the effective stress-strain behavior is extracted from the end of reinforcing plates in the ABAQUS models. A discussion of the selected integration approach is provided in the following section.

5.5.1 Selected Numerical Hinge Integration Method

Multiple predefined plastic hinge integration methods are implemented within the force-based beam-column element developed by Scott and Fenves (2004) that are intended to produce objective responses for softening behaviors. In their research, the authors presented four plastic hinge integration methods, including those that place integration points at the end of the plastic hinge regions and at the midpoint of the plastic hinge region. They concluded that to capture strain softening behavior, the integration methods should satisfy the following criteria: (1) the integration method should sample section forces at the member ends, where the moments are largest in the absence of member loads; (2) the integration approach should provide an exact solution for linear curvature distributions; (3) the integration approach should use a single section to integrate the deformations along the hinge length. In the current research, the modified Gauss-Radau integration is selected based on the following criteria: (1) the modified Gauss-Radau integration method satisfies criteria (1), (2) and (3); and (2) under applied lateral loads, the maximum flexural demands in the beams are expected to occur at the end of the beam, suggesting an integration approach employing integration points at the member's end is preferred over an approach placing an integration point at the midpoint of the hinge. Figure 5.8 shows a schematic of the modified Gauss-Radau hinge integration method, where ξ_i represents the location of the integration points and ω_i represents the weighting functions. The effective stresses

extracted from the end of the reinforcing plate in the parametric FE analyses are used as the basis for the proposed hinge fiber model, as this location aligns with the location of the hinge integration point in the modified Gauss-Radau hinge integration approach.

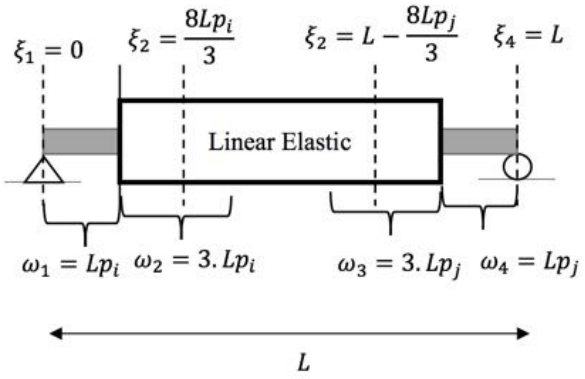

Figure 5.8 Modified Gauss-Radau integration (Scott et al., 2006)

Figure 5.9 shows the application of the plastic hinge integration method in a force-based beam-column element. The effective stress-strain behavior that is obtained from the buckling length in the FE studies is applied to the fiber cross-sections at the integration points in the predefined hinges as seen in the figure, while the inside region defined with fiber sections that remain elastic. Lp_i and Lp_j denote the predefined hinge lengths on each end of the beam, while the interior portion of the element is linear elastic.

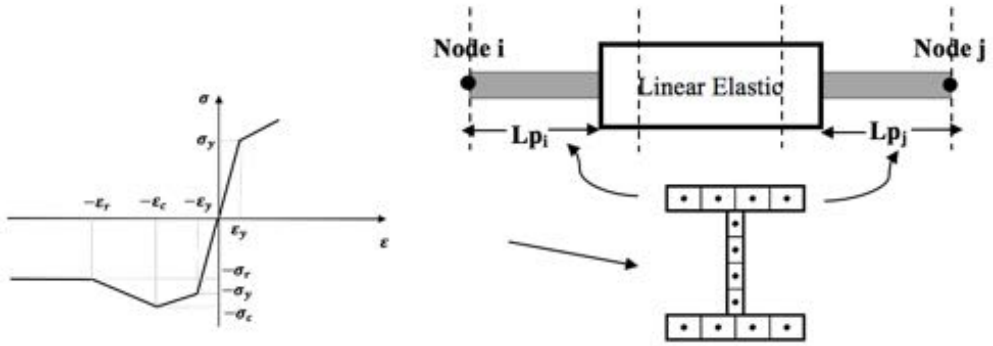

Figure 5.9 The effective stress-strain behavior applied to fiber sections in the predefined plastic hinges of a force-based beam column element

5.6 TRENDS OF KEY PARAMETERS

Previous research (Lignos, 2008) has shown cross-sectional element width-to-thickness ratios to be key drivers of local buckling response. Here, the relationship between these width-to-thickness ratios and the local buckling-induced strength degrading response in PT connections is investigated. The key backbone parameters detailed in Section 4.3.2 are determined from the effective stress-strain responses extracted from each FE model in the parametric study presented in Chapter 4, and these extracted backbone values are plotted with respect to web and flange slenderness ratios to evaluate relationships between them.

Figures 5.10 and 5.11 show dependence of key parameters with respect to flange slenderness, which is indicator of flange local buckling (Lignos, 2008). Figure 5.10 shows the critical stress and strain at which buckling and strength degradation initiates, and Figure 5.11 shows the residual stress and strain at which the stress-strain response stabilizes to a constant residual stress. R^2 represents the coefficient of determination for the linear fit between the response parameter and the flange slenderness ratio, as shown by a red dashed

line. The coefficient of determination indicates how the obtained values can be explained by variation in the dependent variable, and it is used here to indicate the dependence of key backbone response parameters to beam properties. According to Figures 5.10 and 5.11, each key parameter shows clear dependence on the beam flange slenderness ratio. It could be concluded that beam flange slenderness has an effect on the negative post-buckling stiffness and the post-buckling residual stress.

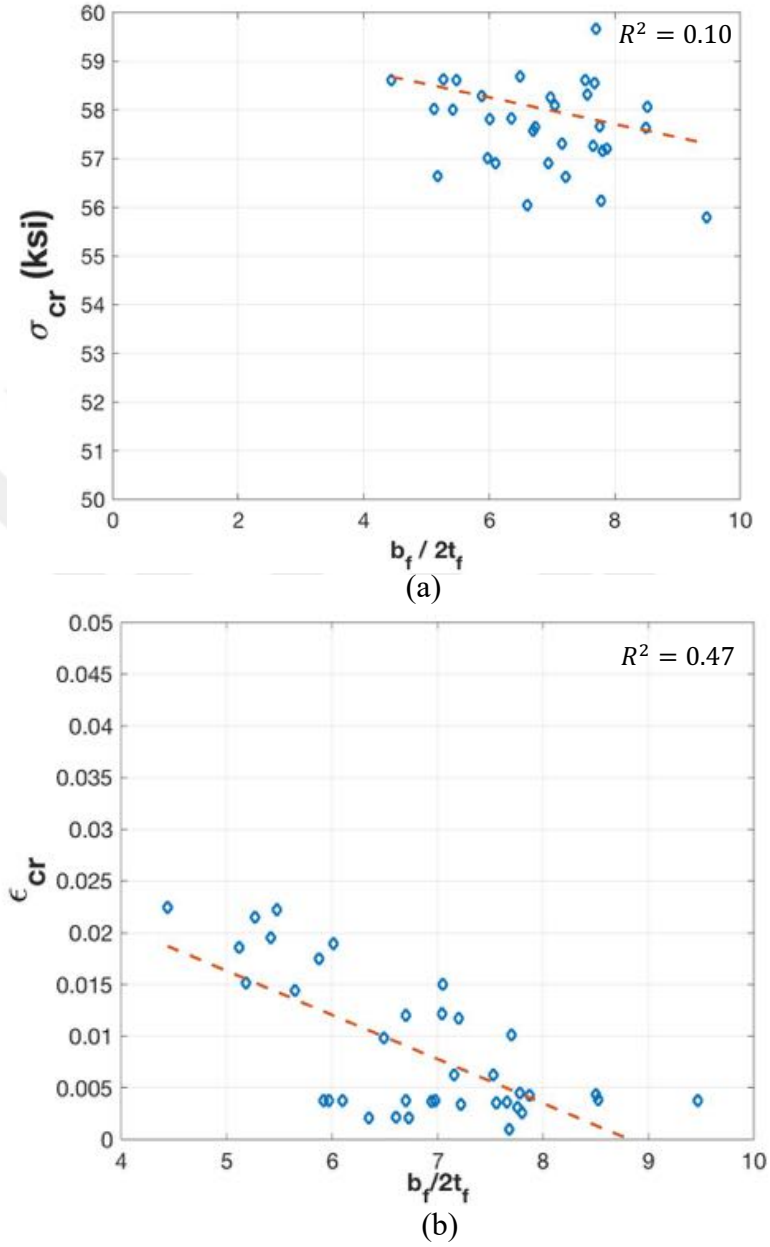

Figure 5.10 Trends for the key backbone parameters with respect to $b_f/2t_f$ (a) critical (maximum) stress; (b) corresponding critical strain

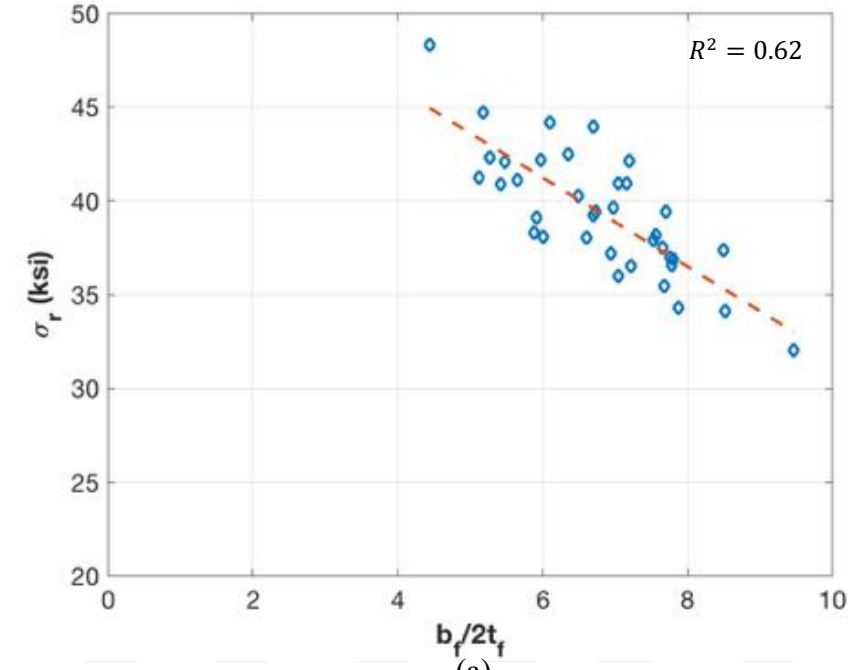

(a)

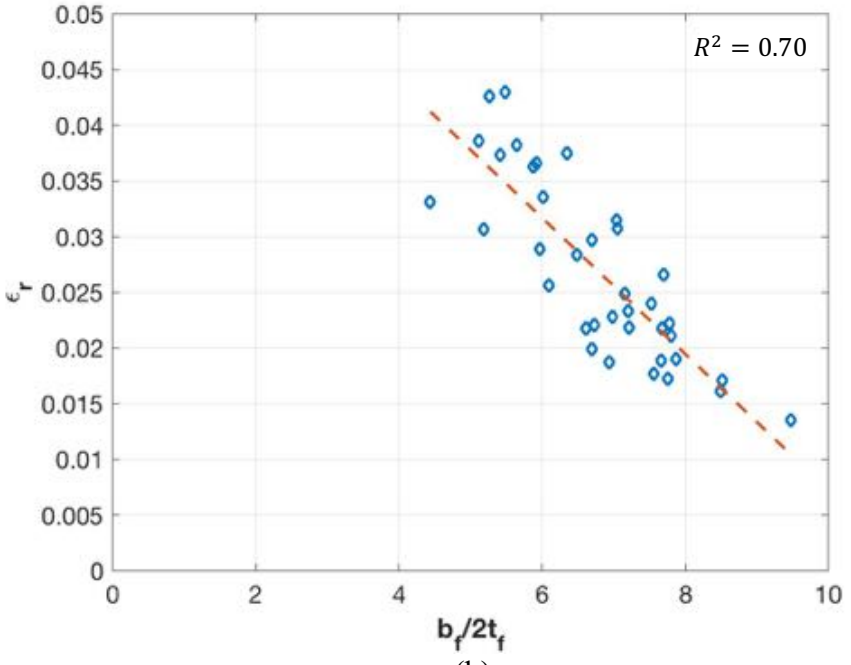

(b)

Figure 5.11 Trends for the key backbone parameters with respect to $b_f/2t_f$ (a) residual stress at which slope changes from degradation to stabilization; (b) corresponding residual strain

The dependence of key parameters with respect to h/t_w is presented in Figure 5.12 and Figure 5.13. As compared to flange slenderness, the key parameters follow a flatter slope with respect to web slenderness and lower R^2 values, except for the critical stress, which indicated the key buckling response parameters are less dependent on web slenderness. A multivariate linear regression analysis is performed in the following section to obtain generalized equations to predict key backbone parameters based on different geometric properties.

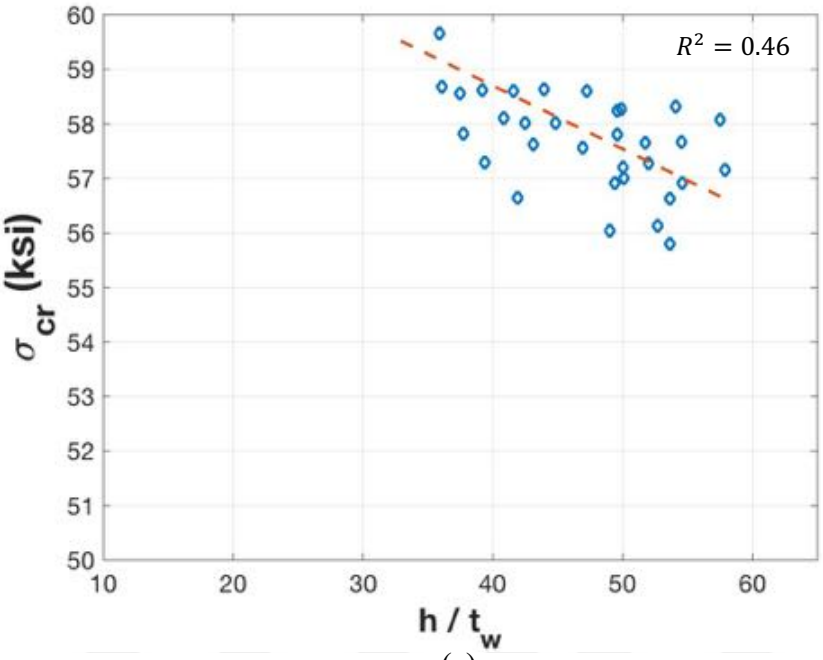

(a)

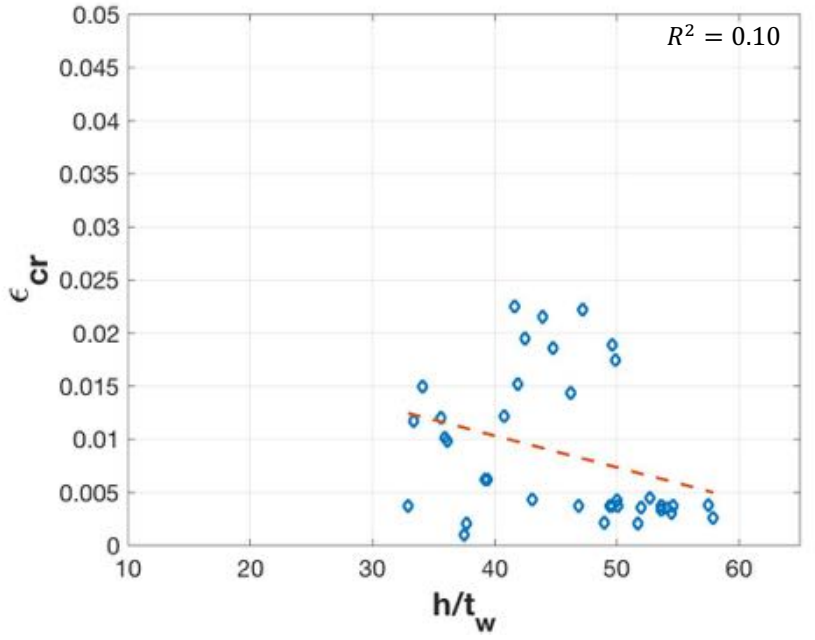

(b)

Figure 5.12 Trends for the key parameters with respect to h/t_w (a) critical (maximum) stress; (b) corresponding critical strain

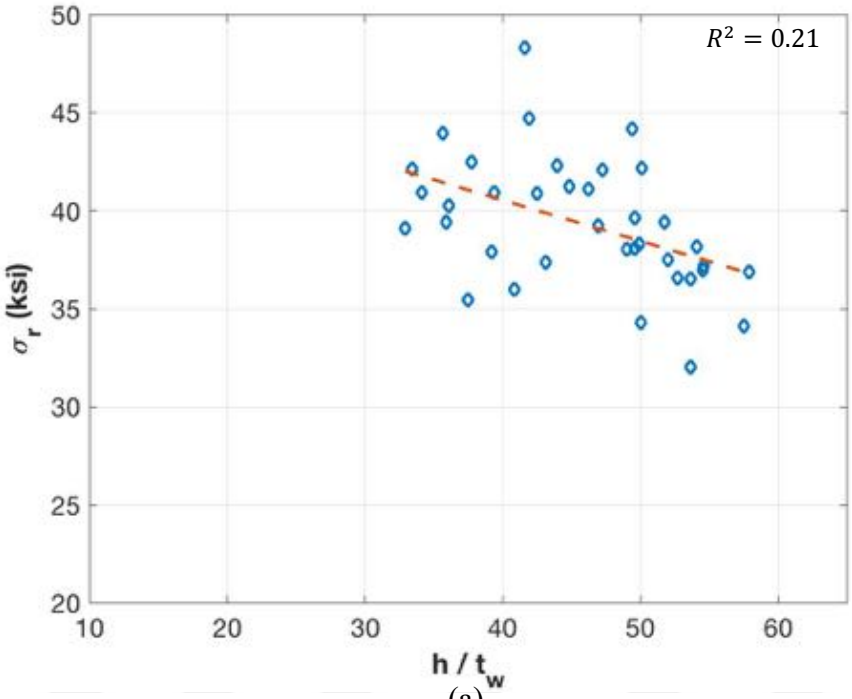

(a)

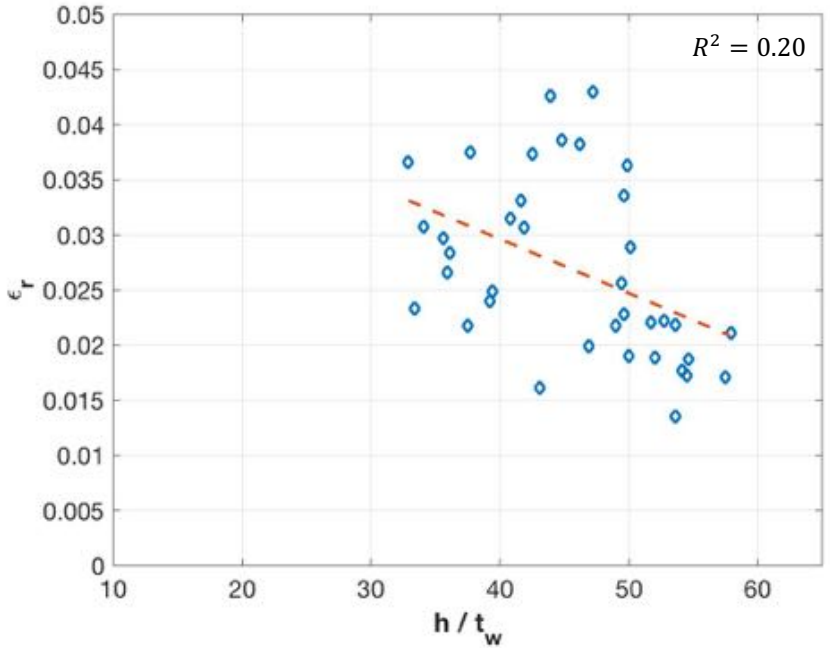

(b)

Figure 5.13 Trends for the key parameters with respect to h/t_w (a) residual stress at which slope changes from degradation to stabilization; (b) corresponding residual strain

5.7 Regression Analysis of Key Constitutive Parameters

As investigated in the previous section, two parameters important to predicting buckling response, beam web and flange slenderness ratios, are included in the regression analysis. Both flange and web parameters are included, because the initiation of buckling in beam flange also triggers web buckling, or, in other words, they are coupled with each other (Lignos 2008).

It is important to choose a comprehensive model that can functionally predict the response parameters. A generalized log-space linear regression model has been used by previous researchers to determine the backbone parameters for strength degradation behavior for wide flange steel beams and hollow structural sections (Lignos, 2008; Suzuki 2018); therefore, a similar model will be used in this study. To predict the response variable (RV), the general log-space linear model is as follows:

$$\log(RV) = \log(a_1) + a_2.\log(X_1) + a_3.\log(X_2) \dots\dots + a_n.\log(X_{n-1}) \quad \text{Eq. 5.1}$$

which can be also be written as:

$$RV = a_1.(X_1)^{a_2}.(X_2)^{a_3} \dots\dots (X_{n-1})^{a_n} \quad \text{Eq. 5.2}$$

Where a_1, a_2,…., a_n are constants identified as regression coefficients and X_1, X_2,…., X_n are the predictor variables. A stepwise linear regression is performed in MATLAB (version R2019b), which considers different models to select the combination of predictor variables that are most important to predicting the response. Stepwise regression is a systematic method for adding and removing terms from a linear model based on their statistical significance in the response variable (MATLAB 2019). The stepwise

linear regression performed here applies a standard *t*-test until all the parameters are statistically significant at the 10% level results. The linear model (Eq. 5.2) is selected based on the coefficient of determination, R^2, values that represent the goodness of fit for each equation, and the *Stepwiselm* function in MATLAB is used to test different equations.

The key parameters that are defined in Chapter 4 can be estimated using the general log-space linear regression model, with local width-to-thickness ratios used as predictor variables. The key backbone parameters, normalized with respect to material properties, are used as the response variable to reflect the material properties of the members (Kolwankar et al. 2018, Suzuki, 2018). The first response variable used to describe the normalized critical buckling strength is σ_{cr}/σ_y , where σ_{cr} is the maximum effective stress (at the critical strain, ε_{cr}) at the onset of strength degradation, and σ_y is the yield stress that is obtained from the material coupon test results:

$$\sigma_{cr}/\sigma_u = 1.05.\left(\frac{h}{t_w}\right)^{-0.088}.\left(\frac{b_f}{2t_f}\right)^{-0.0086} \quad \text{Eq. 5.3}$$

R^2 =0.5

According to linear regression model, the coefficient of determination is estimated as 0.5, where this indicates that h/t_w and $b_f/2t_f$ jointly explain variation in the response variable, σ_{cr}/σ_y, by 50%. Similarly, the corresponding equation to predict the normalized critical strain is:

$$\varepsilon_{cr}/\varepsilon_y = 10^{4.49}.\left(\frac{h}{t_w}\right)^{-0.969}.\left(\frac{b_f}{2t_f}\right)^{-0.286} \quad \text{Eq. 5.4}$$

$R^2 = 0.41$

Similarly, the normalized residual stress at the point where the negative stiffness changes to a more flattened slope is:

$$\sigma_d/\sigma_y = 2.51.\left(\frac{h}{t_w}\right)^{-0.141}.\left(\frac{b_f}{2t_f}\right)^{-0.366} \quad \text{Eq. 5.5}$$

R^2 =0.70

Finally, representing residual strain is:

$$\varepsilon_d/\varepsilon_y = 10^{3.18}.\left(\frac{h}{t_w}\right)^{-0.526}.\left(\frac{b_f}{2t_f}\right)^{-1.409} \quad \text{Eq. 5.6}$$

$R^2 = 0.78$

The parameters E and σ_y can be obtained from the uniaxial material coupon tests data. Figure 5.14 shows one-to-one comparisons of key parameters extracted from FE models and the predicted ones from the regression models.

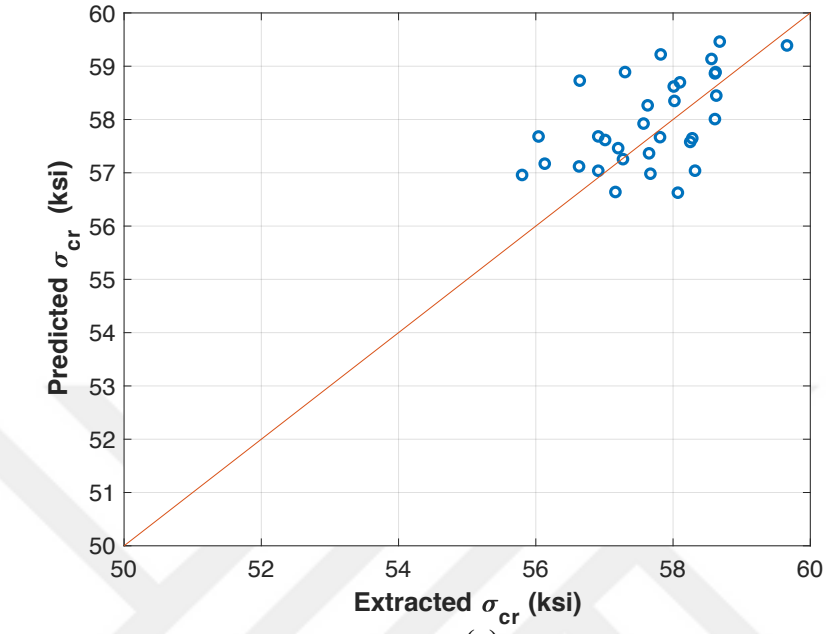

(a)

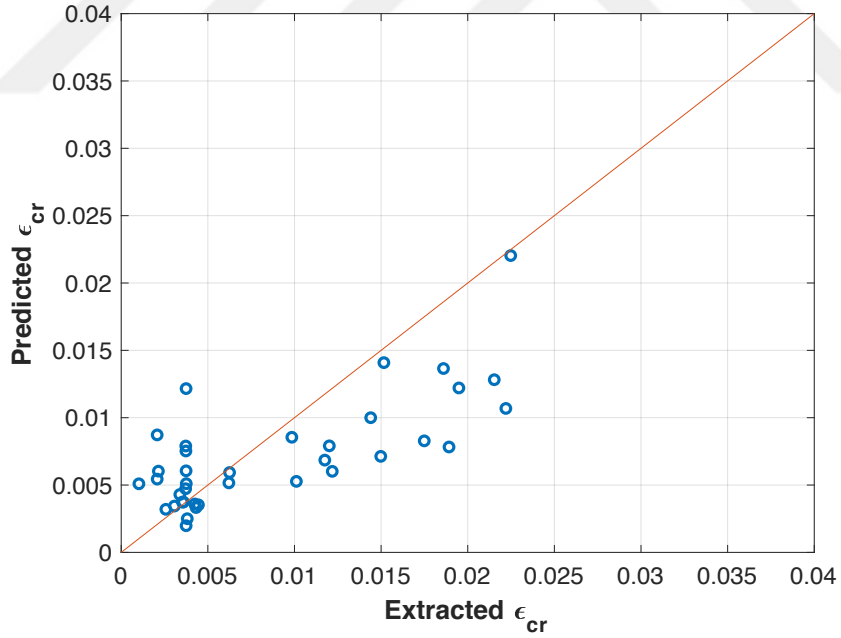

(b)

Figure 5.14 Comparisons between FE-extracted and predicted key parameters (a) critical (maximum) stress; (b) corresponding critical strain; (c) residual stress; (d) corresponding residual strain

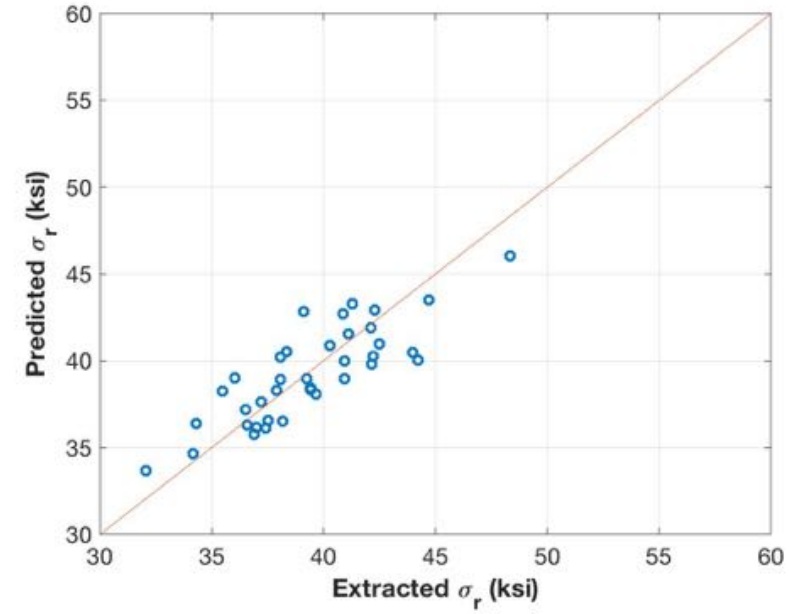

(c)

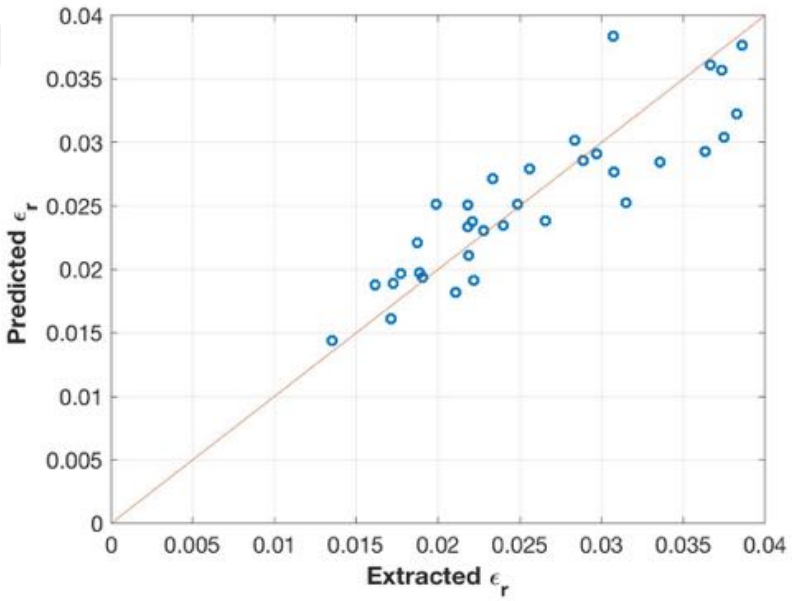

(d)

Figure 5.14 (cont.) Comparisons between FE-extracted and predicted key parameters (a) critical (maximum) stress; (b) corresponding critical strain; (c) residual stress; (d) corresponding residual strain

5.8 Fiber Discretization

A fiber discretization study is performed to achieve balance between numerical accuracy and the computational time. Discretization suggestions by Kostic and Filippou (2012) are followed in this study. The discretization models developed by the authors for wide-flange sections are presented in Figure 5.15. Note that the discretization shown in Figure 5.15 (b) was used by Kostic and Filippou (2012) to explore flange fiber discretization that would impact weak axis bending; however, since strong-axis-only bending is considered in this research, it is ignored in the fiber discretization study. According to the authors' research, for wide-flange sections under complex cyclic load histories of axial force in combination with biaxial bending moments, four fibers in each flange and four fibers in web (Figure 5.15 (a)) gives sufficient accuracy in predicting the cyclic response (Kostic and Filippou, 2012).

Figure 5.16 shows the comparisons of moment vs. drift responses for the current research using different discretization options for *Model Number 5* presented in Table 4.1. The fiber stress-strain behavior presented in this figure is obtained from the empirical equations given in the previous section. As observed in the figure and consistent with the findings of Kostic and Filippou (2012), the discretization with four fibers in each flange and four fibers in the web is selected, both to provide numerical accuracy and reduced computational time, as results do not change significantly with increased number of fibers. For simplicity in modeling, the proposed fiber discretization model is applied to the flanges outside the softening area as well.

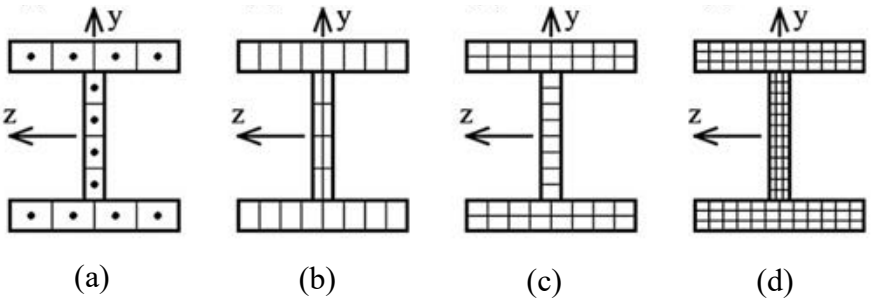

Figure 5.15 Fiber discretization of wide-flange sections (Kostic and Filippou, 2012) (a) 4x1-4x1-4x1 (b) 8x1-4x2-8x1(c) 8x2-8x1-8x2 (d) 12x3-12x3-12x3

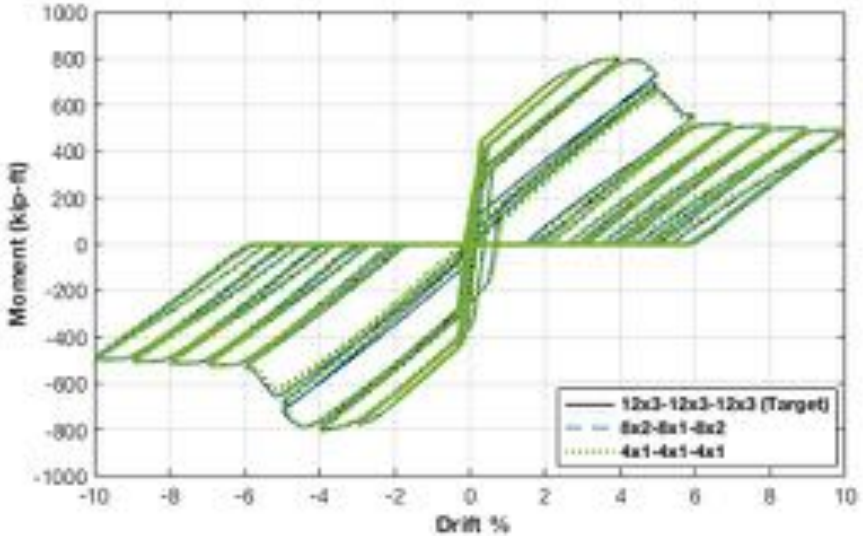

Figure 5.16 Fiber discretization comparisons for moment vs. drift response

5.9 VERIFICATION OF PROPOSED CONSTITUTIVE MODEL

In this section, the proposed fiber-based constitutive model for capturing local buckling-induced softening is compared with each parametric study, as well as experimental results conducted by Hulsey (2015).

5.9.1 Parametric Study

The empirical equations presented in Section 5.7 are first applied to beam sections used in the parametric studies and compared with the ABAQUS results. Figures 5.17 and 5.18 show parametric study comparisons for Model Number 21 and Model Number 3. It can be observed from these figures that predictive equations can capture fairly well strength degradation behavior of PT beam-to-column connections. According to Figure 5.17, the maximum moment of Model Number 21 is with 8% of the ABAQUS results, and the ABAQUS results experience the maximum moment at 4% drift, compared to the 5% drift when OpenSees results reach their maximum moment. Similarly, for Figure 5.18, the ABAQUS model reaches its maximum moment at 3% drift, while the maximum moment in OpenSees is 8 % lower and is reached at 6% drift. Figures 5.19 and 5.20 present one-to-one results for each parametric study for observed maximum moment and the moment at the 10% drift peak. Table 5.1 shows the general trend and errors of OpenSees results by using empirical equations (Section 5.7) and comparison with the ABAQUS results for each parametric study. An average of in 8 % error in maximum moment and 6 % in minimum moment are observed for corresponding forty parametric studies. Furthermore, examples for results of chosen parametric studies are presented in Appendix B with comparisons of extracted and obtained effective stress-strain plots.

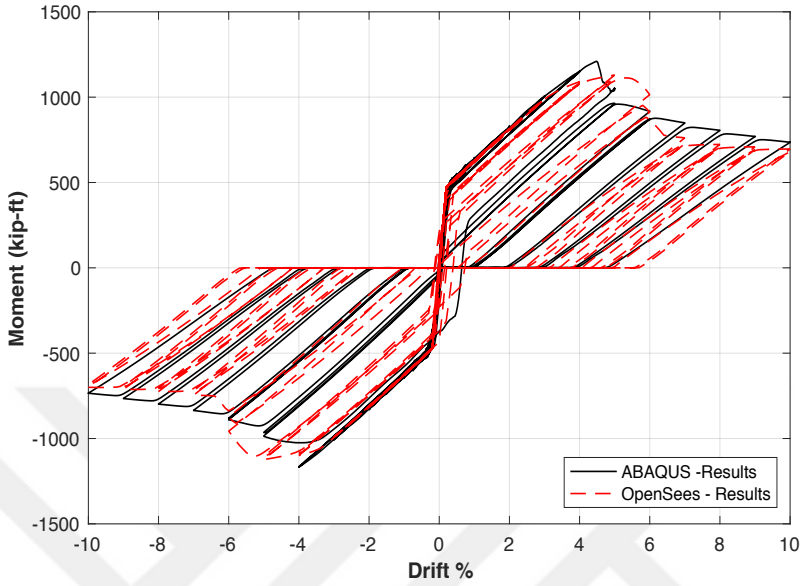

Figure 5.17 Comparisons of ABAQUS results and OpenSees results for predictive equations for Model Number 21

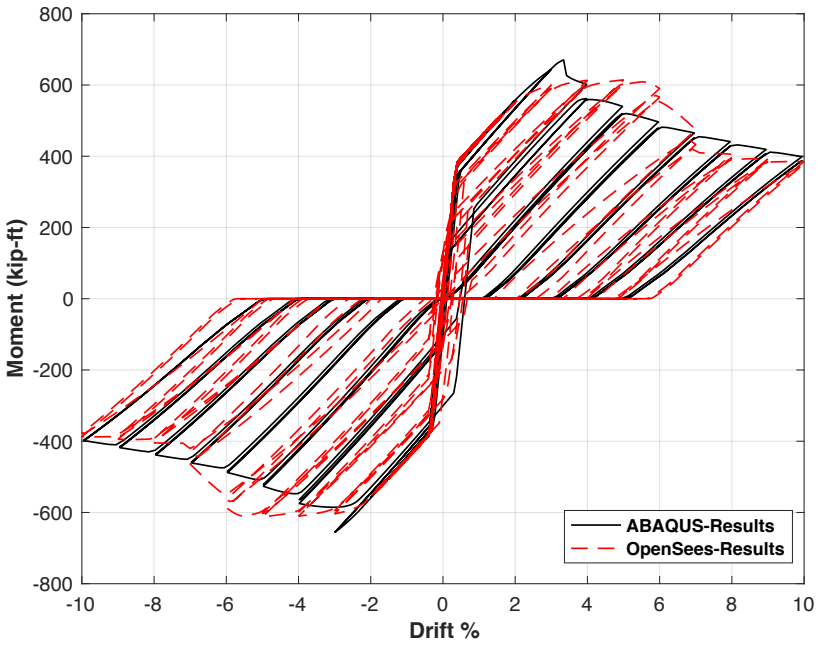

Figure 5.18 Comparisons of ABAQUS results and OpenSees results for predictive equations for Model Number 3

Table 5.1 ABAQUS and OpenSees results comparisons

Model No.	Maximum Moment			Drift at Maximum Moment			Moment at 10% Drift		
	Abaqus (k-ft)	OpenSees (k-ft)	% err	Abaqus (%)	OpenSees (%)	% err	Abaqus (k-ft)	OpenSees (k-ft)	% err
# 1	828	778	6	5	6.8	18	584	566	3
# 2	1219	1087	10	8	8	0	1016	910	10
# 3	667	600	10	3	6	30	399	385	4
# 4	942	843	10	5	6	10	610	509	16
# 5	839	779	7	4	4	0	488	455	7
# 6	1107	1019	8	4	4	0	703	601	14
# 7	1801	1649	8	4	5	10	1107	1107	0
# 8	984	901	8	4	4	0	551	516	6
# 9	1064	981	7	7	7	0	796	894	-12
# 10	1600	1345	15	5	7	30	1149	1022	11
# 11	589	551	6	3	3	0	339	314	7
# 12	1469	1345	8	4	5	10	904	834	7
# 13	318	289	9	3	3	0	174	162	6
# 14	349	306	12	3	3	0	175	162	7
# 15	397	374	6	4	4	0	228	213	7
# 16	771	670	13	6	7	10	562	478	14
# 17	531	481	10	7	7	0	486	360	25
# 18	1542	1311	14	5	5	0	1121	913	18
# 19	2162	2021	7	7	7	0	1960	2006	-2
# 20	1727	1551	10	5	6	0	1242	1463	-17

Table 5.1 Continued.

Model No.	Maximum Moment			Drift at Maximum Moment			Moment at 10% Drift		
	Abaqus (k-ft)	OpenSees (k-ft)	% err	Abaqus (%)	OpenSees (%)	% err	Abaqus (k-ft)	OpenSees (k-ft)	% err
# 21	1204	1110	8	4.5	5	5	740	696	6
# 22	2035	1823	10	5	5	0	1528	1528	0
# 23	1876	1778	5	7	5	-20	1665	1665	0
# 24	1659	1561	6	7	7	0	1413	1468	-5
# 25	2410	2199	9	4	5	10	1762	1485	15
# 26	2547	2335	8	5	6	10	1986	2397	-16
# 27	1590	1503	5	6	7.5	15	1145	1058	8
# 28	1756	1629	7	4	6	20	1305	1120	14
# 29	352	352	0	6	6	0	283	214	24
# 30	2238	1825	8	5	6	10	1599	1915	-20
# 31	2080	1922	8	4.5	6	15	1423	1208	15
# 32	2663	2465	7	7	5	20	1762	1485	15
# 33	1983	1825	8	5	5	0	1512	1512	0
# 34	1408	1288	9	4	6	20	946	888	6
# 35	1168	1073	8	4	5	10	797	744	7
# 36	819	776	5	6	7	10	2343	1975	0
# 37	457	433	5	4	4	0	274	253	8
# 38	527	486	5	4	4	0	336	301	8
# 39	488	424	5	3	4	10	267	258	3
# 40	354	343	3	4	4	0	229	208	9

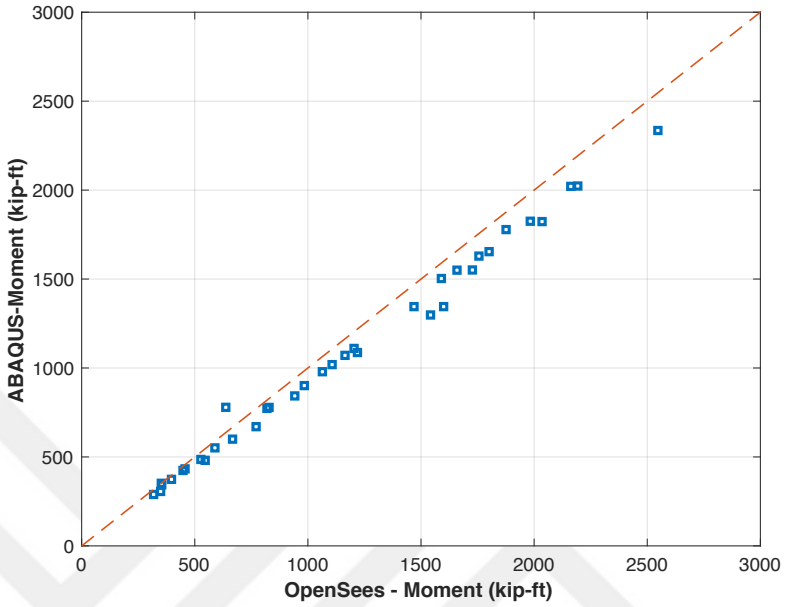

Figure 5.19 Comparisons of maximum moment observed from ABAQUS FE models vs. OpenSees models

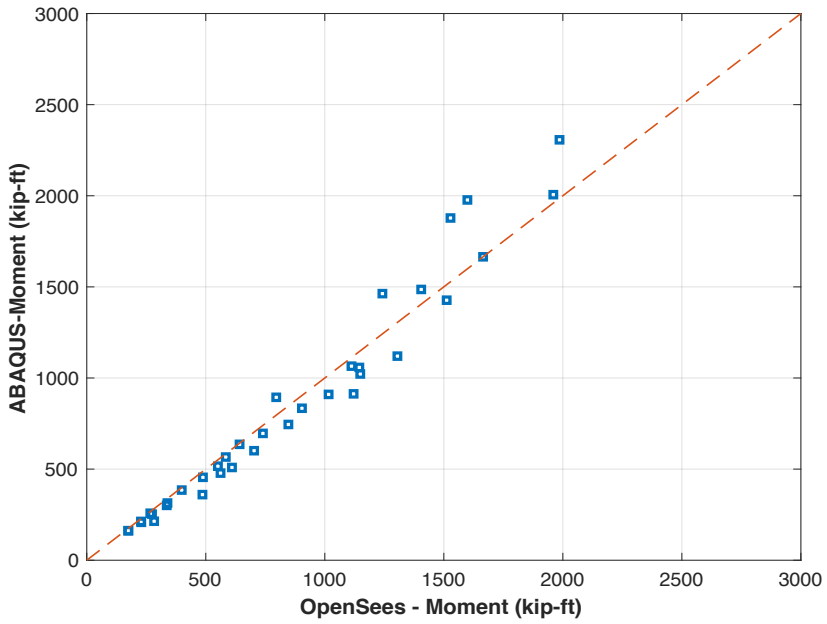

Figure 5.20 Comparisons of moment response at 10% drift from ABAQUS models vs. OpenSees models

5.9.2 Hulsey (2015)

The proposed fiber-based model for local buckling-induced softening is verified by comparing the results with experimental tests conducted by Hulsey (2015), whose details are given in Chapter 3. For Test Specimen 2, which constitutes a W18x55 beam with width-to-thickness ratios of $b_f/2t_f$ = 5.98 and h/t_w = 43.2, experimental results are compared to OpenSees model results using the proposed stress-strain constitutive model. Figures 5.21 and 5.22 compare the experimental moment vs. drift and PT force vs. drift results, respectively, with the proposed model. It is evident from these figures that the proposed constitutive relationship can capture the strength degrading behavior due to beam local buckling, particularly in terms of capture the residual drift at the end of testing (moment equal to zero) and the total loss in PT force, which is directly correlated to the plastic shortening of the beam caused by local buckling. Observed PT loss during the experiment is 171 kips, while a PT loss of 147 kips is predicted from the OpenSees model, resulting in a 14% error. It is worth noting that the moment vs. drift response of the proposed OpenSees model very closely matches the experimental response in the negative drift direction (North direction) with a 6% error in the maximum moment at the 3% drift peak. In the positive loading direction (South direction) at the peak of the first 4% drift cycle, there was a loud sound that was emitted from the experimental specimen, resulting in a sudden drop in strength. The simulated response matches the experimental response after this first 4% drift cycle, indicating that the loud noise and sudden strength loss in the experimental specimen may have been caused by something in the test set-up in this loading direction.

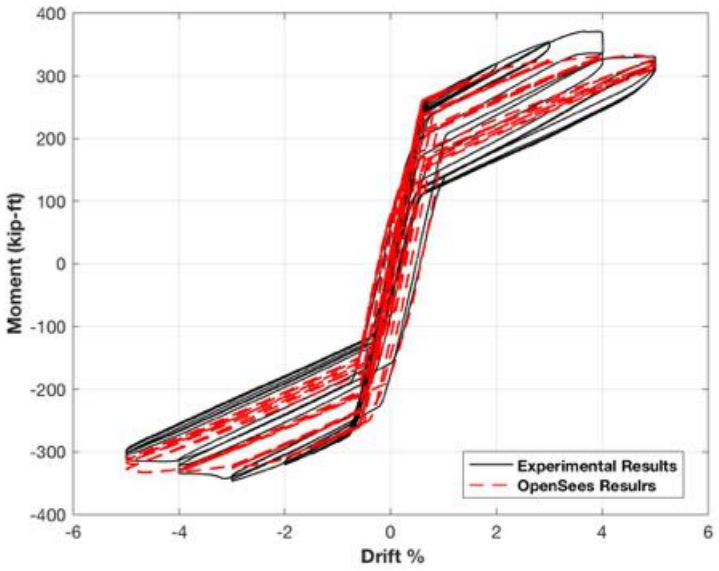

Figure 5.21 Comparison of experimental and OpenSees results for connection moment vs. drift response of Test Specimen 2

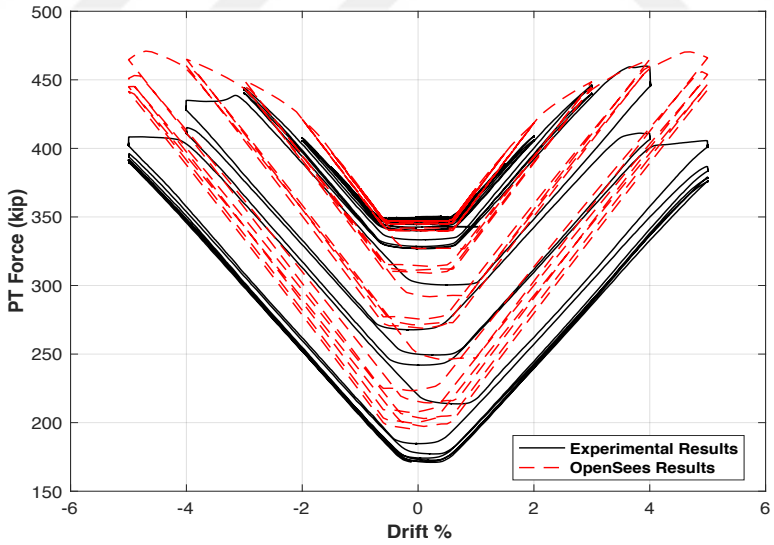

Figure 5.22 Comparison of experimental and OpenSees responses for PT force vs. drift response of Test Specimen 2

Secondly, Test Specimen 3 experimental results have been compared with the OpenSees model employing the constitutive relationship proposed in Equations 5.1-5.4. The web and flange width-to-thickness ratios of $b_f/2t_f = 8.11$ and $h/t_w = 39.6$, respectively, are inserted into the referenced equations. Figure 5.23 shows the moment vs. drift response comparison, and Figure 5.24 shows the PT force vs. drift response. According to the figures, the proposed OpenSees model results can capture the strength degradation behavior of the connection and PT losses due to beam local buckling. The maximum moment predicted by the OpenSees model in the North direction had an 8% error compared to the experimental value. Although the total PT losses in the OpenSees model and the experiment are similar as both reach a zero value by the end of the loading history, the slope of the PT force vs. drift response for the OpenSees model is slightly higher than the experimental results, which means the OpenSees model fully loses its PT force at an earlier drift than the experiment.

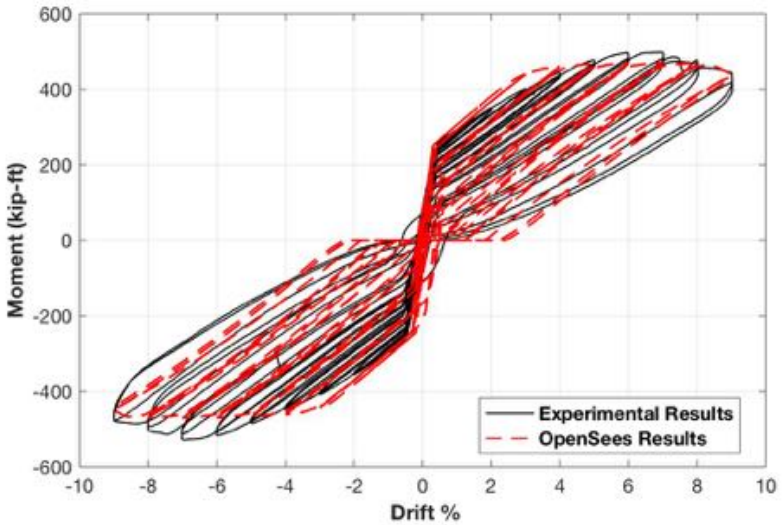

Figure 5.23 Comparison of experimental and OpenSees responses for moment vs. drift response of Test Specimen 3

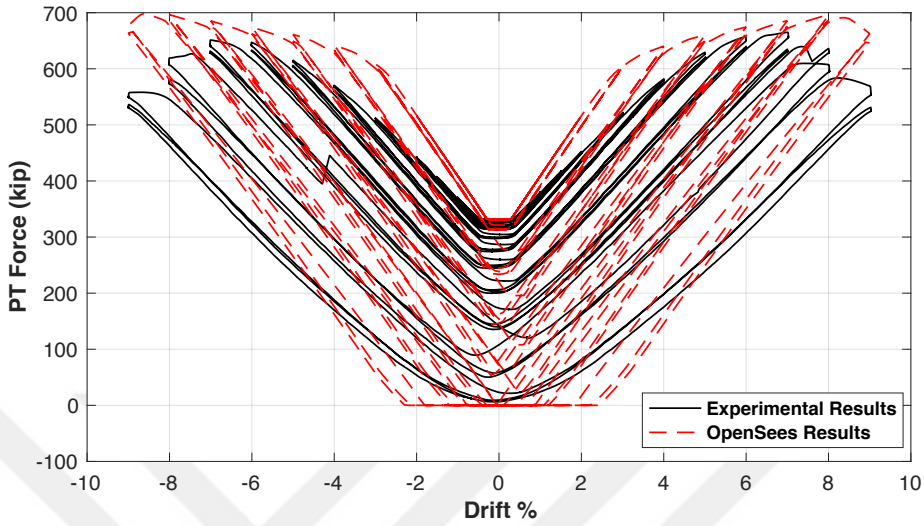

Figure 5.24 Comparison of experimental and OpenSees responses for PT force vs. drift response of Test Specimen 3

5.10 LIMITATIONS OF THE PROPOSED CONSTITUTIVE MODEL

The proposed stress vs. strain hysteretic behavior for modeling strength degradation in PT beam-to-column connections has a number of limitations. Specifically, this research focuses on local buckling induced softening behavior and is intended to simulate the response of connections when lateral torsional buckling of the beams is not of concern. Therefore, the proposed model should not be used for beams with member slenderness L_b/r_y >50.

For the modeling of the strength degradation behavior, force-based elements with end hinges are used. If conventional distributed plasticity force-based beam-column elements are used, models can suffer mesh dependency problems, which is a known limitation for distributed plasticity elements with softening behaviors; therefore, at this point it is recommended to used nonlocal formulations, such as pre-defined hinge lengths, that eliminate mesh dependency (Kolwankar et al., 2018).

5.11 SUMMARY AND CONCLUSIONS

The proposed fiber-based modeling of steel PT beam-to-column connections is implemented in OpenSees. The force-based beam-column element with end hinges is selected to model the beams in the PT connections. The Gauss-Radau hinge integration method was selected based on the effective stress-strain results extracted from the buckling length of the finite element simulations. Statistical trends for the key parameters of the effective stress-strain backbone behaviors obtained from the parametric finite element studies are investigated. Based on statistical trends of the engineering parameters important in capturing the initiation of buckling in wide-flange sections, empirical equations are developed to determine key backbone parameters of the proposed constitutive relationship. Experimental and detailed numerical finite element model results are compared with the simulation results obtained using the proposed fiber-based model implemented in OpenSees. The results obtained by the proposed equations are shown to provide reasonably accurate predictions of PT beam-to-column connection responses for the range of variables and cross-sections considered in this study. Further research is necessary to include models with energy dissipation elements in the connection and to investigate connections with different loading histories.

Chapter 6: Summary, Conclusions, and Recommended Future Research

6.1 SUMMARY

The aim of the research in this dissertation is to investigate numerical modeling of the strength degradation behavior in PT steel beam-to-column connections. One primary contribution of this dissertation is the development of finite element models for capturing local buckling behavior and the progression of buckling with comparisons to experimental tests (Hulsey, 2015) of PT beam-to-column connections in the absence of energy dissipating elements. The proposed methods can also be used in the simulation of PT connections with energy dissipating devices by adding additional axial elements within the connection to simulate the hysteretic response of the energy dissipation device. In this research, a stress-strain constitutive relationship is proposed to model the local buckling-induced strength degradation in PT connections using relatively simple and computationally efficient modeling approaches.

Chapter 3 discussed finite element modeling approaches to simulate the local buckling response in PT connections using solid and shell elements in ABAQUS. Gap opening and closing phenomena were modeled using contact interactions for solid elements, while compression-only axial connecters are used in the shell element models. The vertical restraint provided by the slotted shear tab connection in the PT connection is modeled using slot connectors in the shell element models and using friction in the contact interaction of the solid element models. Another major difference between the shell and solid element models is the modeling of the PT bars; PT bars are modeled with solid elements in the solid element models, and the PT bars are modeled as truss elements in the shell element models. Initial imperfections are included to initiate local buckling in the shell element models, while initial imperfections are not considered in the solid element

models to reflect general modeling recommendations for PT beam-to-column connection up to this time in literature (Moradi, 2015; Kim, 2008). Geometric and material nonlinearities are included in the analysis.

In Chapter 4, to investigate the effect of PT connection design parameters on the strength degradation behavior, a parametric study is performed using detailed FE models with different beam cross-sections. The results of the parametric studies are used to obtain the effective stress-strain relationship that characterized the strength degrading behavior of the locally buckled region. The buckling length is also extracted from these models and compared with estimated buckling length predictions in the literature (Kolwankar et al., 2018; Suzuki, 2018).

Chapter 5 proposes a fiber-based modeling approach for self-centering PT beam-to-column connections in OpenSees. A force-based beam-column element with predefined hinges employing modified Gauss-Radau integration is selected for the implementation of the effective stress-strain behavior. The effective stress-strain behavior is idealized into a multi-linear backbone described by key backbone parameters. Empirical equations are obtained for these key backbone parameters based on the parametric studies and are applied as the material in the fiber cross-sections employed in the proposed beam hinge model in OpenSees. Results from the proposed fiber-based OpenSees model are compared with those from experimental tests and shell-based finite element analyses.

6.2 CONCLUSIONS

This study showed that the shell element FE models can accurately capture the strength degradation behavior due to beam local buckling observed in experimental studies. Based on findings in Chapter 3, shell element models are selected to perform the parametric studies in Chapter 4. According to parametric study results, the extracted effective stress-

strain behavior follows a multi-linear trend and the effective stress-strain behavior showed that the beam experiences only compressive strains throughout its reverse cyclic load history due to the large compressive forces from the PT elements. Key points of this generalized multi-linear backbone are characterized using regression analysis of the FE results, and the proposed empirical equations are shown to reasonably accurately predict extracted values for the range of variables and cross-sections considered in this study. This research showed that an increase in initial PT force has only a slight effect on reducing the residual stress at stabilization, while the reinforcing plate length slightly affects the critical stress where local buckling initiates.

6.3 Recommended Future Research

The study in this dissertation focused only on PT beam-to-column connections without the presence of energy dissipation (ED) devices, thus the resulting FE parametric study and effective stress-strain relationships presented in this dissertation represent the behavior of PT beam-to-column connections without the presence of ED elements. Although, results could still be applied to the beams of PT connections with ED elements, further research should be conducted to confirm this hypothesis. Experimental data investigating the local buckling response of PT connections with ED devices are severely limited; however, the finite element models proposed in this dissertation could be used with the addition of different types of energy dissipation elements added to the connection models to explore this connection type numerically.

Further experimental study is needed to test local buckling behavior for PT beam-to-column connections by considering a wide range of beam sections. Experimental data of PT connections that include local buckling limit state response is limited to beams of sizes W18x76, W18x55, W36x150 and W24x76. Furthermore, the existing test data only

consider cyclic load histories with increasing drift amplitudes. Future experimental studies should also consider other loading histories to investigate the impact of loading history on buckling and strength degrading response.

In collapse risk assessment, models capable of capturing strength degrading behaviors are necessary, and, due to the large number of nonlinear response history analyses that must be run, computationally efficient modeling approaches are preferred. Thus, the proposed OpenSees fiber-based model and constitutive equations that capture strength degrading behaviors associated with beam local buckling can be used in system-level collapse performance studies.

Appendix A

This section provides material properties defined for tri-linear material model defined in ABAQUS as true stress and true strain.

Table A.1 Material Properties for Beam Webs

Specimen Number	Beam Size	σ_y (ksi)	σ_t (ksi)	ε_t	σ_u (ksi)	ε_u
1	W18x65	53	74	0.053	96	0.223
2	W18x55	58	76	0.047	96	0.224
3	W18x76	56	72	0.046	100	0.224

Table A.2 Material Properties for Beam Flanges

Specimen Number	Beam Size	σ_y (ksi)	σ_t (ksi)	ε_t	σ_u (ksi)	ε_u
1	W18x65	51	72	0.045	100	0.226
2	W18x55	55	72	0.048	94	0.224
3	W18x76	54	72	0.045	100	0.241

Appendix B

This section gives examples of effective stress strain relationship comparisons between extracted ABAQUS results and empirical equations given in Section 5.7. Furthermore, comparisons of moment-drift response are also demonstrated for related models.

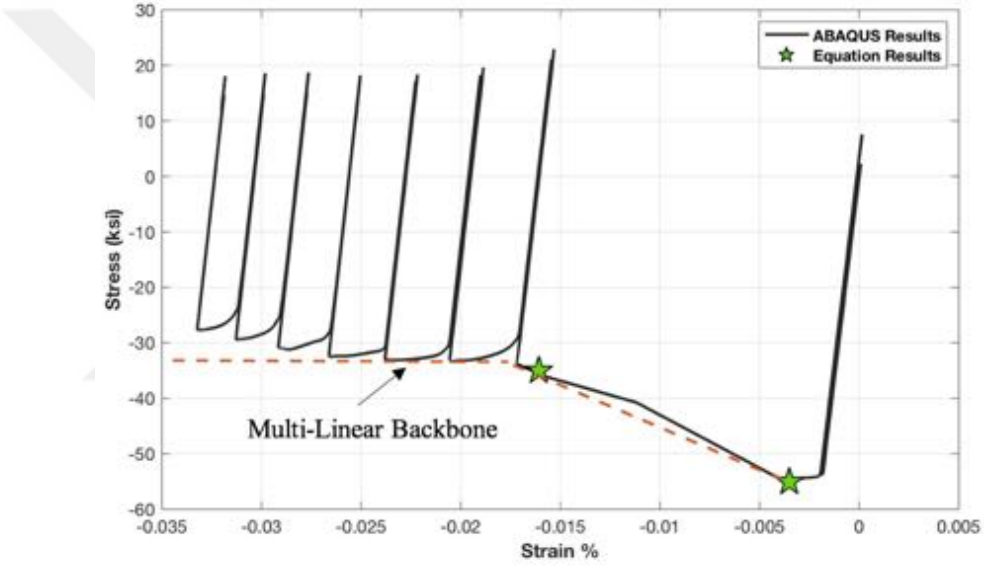

Figure B.1 Comparison between ABAQUS results with multi-linear backbone and Regressed Equation results for Model Number 8

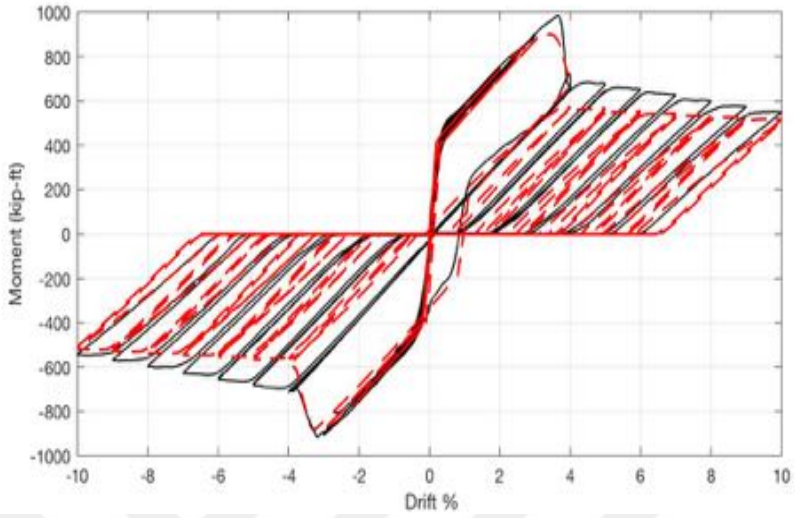

Figure B.2 Comparison of ABAQUS results and OpenSees results for Model Number 8

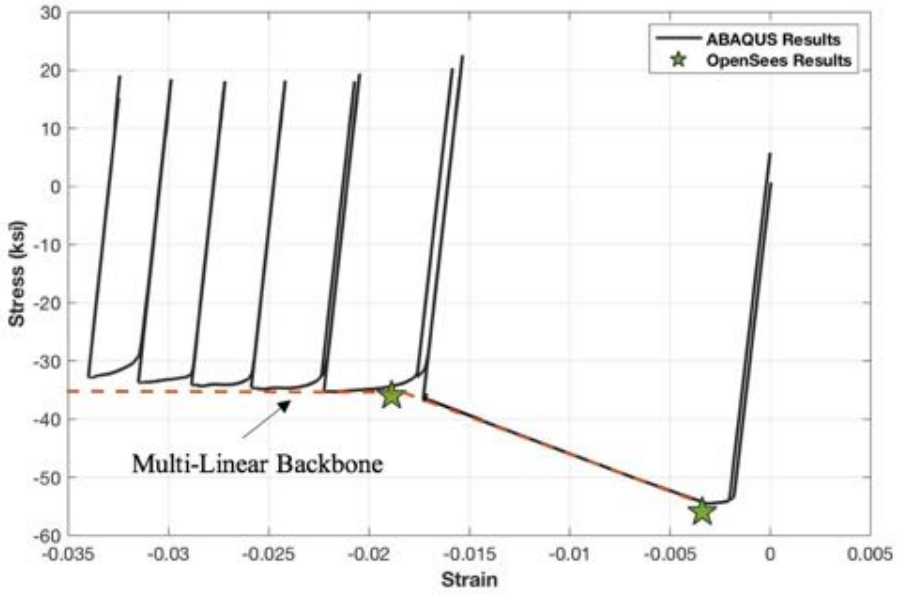

Figure B.3 Comparison between ABAQUS results with multi-linear backbone and Regressed Equation results for Model Number 12

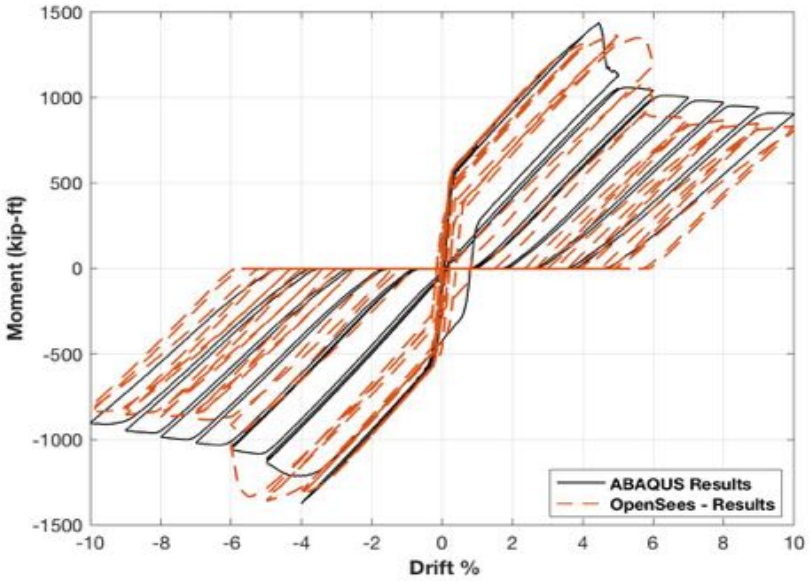

Figure B.4 Comparison of ABAQUS results and OpenSees results for Model Number 12

References

ABAQUS. 2014. *ABAQUS Version 6.14 documentation*. Simulia

ANSYS 15 [Computer software]. Canonsburg, PA, Ansys.

AISC.2016b. *ANSI/AISC 341-16 Seismic Provisions for Structural Steel Buildings.* Chicago, IL: American Institute for Steel Construction (AISC).

Ahmadi, Omid 2016. "Seismic Collapse Assessment of Self-Centering Steel Moment Resisting Frame Systems with Web Friction Devices (Ph.D. Dissertation)." Lehigh University.

Ahmadi, Omid, James M. Ricles, and Richard Sause. 2018. "Modeling of Seismic Collapse Resistance Study of a Steel SC-MRF." *Soil Dynamics and Earthquake Engineering* 113: 324-338.

Behbahanifard, MR, GY Grondin, and AE Elwi. 2004. "Analysis of Steel Plate Shear Wall Using Explicit Finite Element Method." *Proc., 13th World Conference of Earthquake Engineering, Vancouver, B.C., Canada*.

Chancellor, Nathan B., Matthew R. Eatherton, David A. Roke, and Tugce Akbas. 2014. "Self-Centering Seismic Lateral Force Resisting Systems: High Performance Structures for the City of Tomorrow". *Buildings* 4: 520-548.

Christopoulos, C., Filiatrault, A., Uang, C.-M., and Folz, B. 2002. "Post- tensioned energy dissipating connections for moment-resisting steel frames." *Journal of Structural Engineering*, 9 (1111): 1111–1120.

Christopoulos, C., Pampanin, S., Priestley, M. J. (2003). "Performance-Based Seismic Response of Frame Structures including Residual Deformations. Part I: Single-Degree-of-Freedom Systems." *Journal of Earthquake Engineering*, 7 (1): 97-118.

Clayton, Patricia M. 2013. "Self-Centering Steel Plate Shear Walls, Subassembly and Full-Scale Testing (Ph.D. Dissertation)." University of Washington.

Clayton, Patricia M., Ching-Yi Tsai, Jefferey W. Berman, and Laura N. Lowes. 2015. "Comparisons of Web Plate Numerical Models for Self-Centering Steel Plate Shear Walls." *Earthquake Engineering & Structural Dynamics* 44 (12): 2093-2110.

Deierlein, G. G., A. B. Liel, C. B. Haselton, and C. A. Kircher (2007). "Assessing Building System Collapse Performance and Associated Requirements for Seismic Design." *SEAOC Convention* (Tahoe, CA).

Elkady, A., Lignos, D. G. (2015a). "Analytical investigation of the cyclic behavior and plastic hinge formation in deep wide-flange steel beam-columns." *Bulletin of Earthquake Engineering*, 13 (4), 1097-1118.

Esposto, M. 2008. "PTED Beam-to-Column Connections for Steel Moment Resisting Frames: Structural Identification Based on Numerical Analyses (Ph.D. Dissertation).", Università degli Studi di Napoli Federico II.

FEMA. 2009. *Quantification of Building Seismic Performance Factors, FEMA P695*. Washington D.C.: Federal Emergency Management Agency (FEMA).

Feng, D., Kolay C., Ricles, J.M., and Li, J. 2015. "Collapse Simulation of Reinforced Concrete Frame Structures." *Tall and Special Buildings* 25(12): 578-601.

Garlock, M. E. M. 2002. "Design, Analysis, and Experimental Behavior of Seismic Resistant Post-Tensioned Steel Moment Resisting Frames (Ph.D. Dissertation)." Lehigh University.

Guan, X., Moradi, S., and Burton H. 2018. "Seismic Performance of a Self-Centering Steel Moment Frame Building." *Eleventh U.S. National Conference on Earthquake Engineering,* Los Angeles, California.

Hulsey, Anne M. 2016. "Mitigating Local Buckling of Post-tensioned Connections in Steel Self-Centering Moment Resisting Frames (Master Thesis)." University of Texas at Austin.

Iyama, J., Seo, C.-Y., Ricles, J. M., and Sause, R. 2009. "Self-centering MRFs with Bottom Flange Friction Devices under Earthquake Loading." *Journal of Constructional Steel Research* 65(2): 314–325.

Ibarra, L. F., and Krawinkler, H. (2005). "Global Collapse of Frame Structures Under Seismic Excitations", *John A. Blume Earthquake Engineering Center Report, No. 152*, Stanford University.

Kamperidis, Vasileios C. 2016. "Novel Damage-Free Self-Centering Column Base Connection for Earthquake-Resilient Steel Buildings (Ph.D. Dissertation)." University of Warwick.

Kim, H.-J., and Christopoulos, C. 2008. "Friction Damped Posttensioned Self-Centering Steel Moment-Resisting Frames." *Journal of Structural Engineering* 134:11(1768): 1768–1779.

Kim, H.-J., and Christopoulos, C. (2009a). "Numerical Models and Ductile Ultimate Deformation Response of Post-tensioned Self-Centering Moment Connections." *Earthquake Engineering and Structural Dynamics* 38(1): 1–21.

Kolwankar, S., Amit Kanvinde, Maha Kenawy, Dimitros Lignos, and Sashi Kunnath. 2018. "Simulating Local Buckling-Induced Softening in Steel Members Using an Equivalent Nonlocal Material Model in Displacement-Based Fiber Elements." *Journal of Structural Engineering* 144(10): 04018192.

Kolwankar, S., Amit Kanvinde, Maha Kenawy, Dimitros Lignos, and Sashi Kunnath. 2018. "Simulating Cyclic Local Buckling-Induced Softening in Steel Beam-Columns Using a Nonlocal Material Model in Displacement-Based Fiber Elements." *Journal of Structural Engineering* 146(1): 04019174

Kostic, S.M., and Filippou, F.C., 2012. “Section Discretization of Fiber Beam-Column Elements for Cyclic Inelastic Response.” *Journal of Structural Engineering* 138 (5): 592–601.

Liel, Abbie B. 2008. “Assessing the Collapse Risk of California’s Existing Reinforced Concrete Frame Structures: Metrics for Seismic Safety Decisions (Ph.D. Dissertation).” Stanford University.

Lignos, D. G. (2008). “Sidesway Collapse of Deteriorating Structural Systems under Seismic Excitations (Ph.D. Dissertation).” Stanford University.

Lignos, D. G., Krawinkler, H. 2010. "A steel Database for Component Deterioration of Tubular Hollow Square Steel Columns under Varying Axial Load for Collapse Assessment of Steel Structures under Earthquakes." *Joint Conference Proceedings of 7th International Conference on Urban Earthquake Engineering (7CUEE) & 5th International Conference on Earthquake Engineering (5ICEE)*, Tokyo, Japan.

Lin, Y., Sause, R., and Ricles, J.M. 2013. “Seismic Performance of Steel Self-Centering Moment-Resisting Frame: Hybrid Simulations Under Design Basis Earthquake.” Journal of Structural Engineering 139 (11): 1823-1832.

McKenna F. T. 1997. “Object-oriented finite element analysis: Frameworks for analysis, algorithms and parallel computing (PhD dissertation).” University of California, Berkeley.

McKenna F. T. 1997. “Object-oriented finite element analysis: Frameworks for analysis, algorithms and parallel computing (PhD dissertation).” University of California, Berkeley.

Medina, R. A., Krawinkler, H. (2003). “Seismic Demands for Nondeteriorating Frame Structures and Their Dependence on Ground Motions.” *John A. Blume Earthquake Engineering Center Report*, No. 144, Stanford University.

Moehle, J., and Gregory G. Deierlein. 2004. “A Framework Methodology for Performance-Based Earthquake Engineering.” *Proc., 13th World Conference of Earthquake Engineering, Vancouver, B.C., Canada*.

Moradi, S., Alam, S.M., “Finite-Element Simulation of Posttensioned Steel Connections with Bolted Angles under Cyclic Loading.” 2016. *Journal of Structural Engineering* 142(1): ISSN 0733-9445/04015075(15).

Neuenhofer, A., Filippou, F. C. 1997. "Evaluation of Nonlinear Frame Finite-Element Models." *Journal of Structural Engineering*, 123 (7), 958-966.

Ricles, J., Sause, R., Garlock, M., and Zhou C. 2001. “Posttensioned Seismic Resistant Connections for Steel Frames.” *Journal of Structural Engineering*, 127(2): 113-121.

Ricles, J., Sause, R., Peng, S. W., and Lu, L. W. 2002. “Experimental Evaluation of Earthquake Resistant Post-Tensioned Steel Connections.” *Journal of Structural Engineering* 128(7):850-859.

Scott, M. H., Fenves, G. L. 2016. "Plastic Hinge Integration Methods for Force-Based Beam- Column Elements." *Journal of Structural Engineering*, 132 (2), 244-252.

Suzuki, Yusuke. 2018. “Earthquake-Induced Collapse of Steel Moment Resisting Frames with Conventional and High Performance of Steel Columns (Ph.D. Dissertation).” McGill University.

Vasdravellis, G., Karavasilis, T. L., and Uy, B. 2013b. “Large-Scale Experimental Validation of Steel Posttensioned Connections with Web Hour-Glass Pins.” *Journal of Structural Engineering*, 1033–1042.